UNIVERSITÉ DE LIMOGES
ÉCOLE DOCTORALE 522
FACULTÉ DES SCIENCES ET TECHNIQUES

Année : 2014 Thèse N X

Thèse

pour obtenir le grade de

DOCTEUR DE L'UNIVERSITÉ DE LIMOGES

Discipline : Matériaux Céramiques et Traitements de Surface

présentée par

Anastasia GULENKO

le 23 octobre 2014

Etude structurale du verre de TeO_2 et de la variété désordonnée TeO_2-δ par dynamique moléculaire

Thèse dirigée par Olivier MASSON et Philippe THOMAS

JURY :

Rapporteurs

Pierre BORDET	Directeur de Recherche CNRS, Université Joseph Fourier, Grenoble (France)
Konstantin SMIRNOV	Chargé de Recherche CNRS, Université de Lille 1, Lille (France)

Examinateurs

Alex HANNON	Ingénieur de Recherche, ISIS Facility, Didcot (England)
Olivier MASSON	Professeur, Université de Limoges, Limoges (France)
Philippe THOMAS	Directeur de Recherche CNRS, Université de Limoges, Limoges (France)

UNIVERSITÉ DE LIMOGES

ÉCOLE DOCTORALE 522

FACULTÉ DES SCIENCES ET TECHNIQUES

Year : 2014 Thesis N X

Thesis

submitted for the degree of

DOCTOR OF PHILOSOPHY OF THE UNIVERSITY OF LIMOGES

Discipline : Ceramic Materials and Surface Treatment

presented by

Anastasia GULENKO

23 october 2014

Structural study of amorphous TeO_2 and disordered $\delta-TeO_2$ phase by molecular dynamics simulations

Supervisors: Olivier MASSON and Philippe THOMAS

JURY :

<u>Reviewers</u>

Pierre BORDET	CNRS Research Director, University Joseph Fourier, Grenoble (France)
Konstantin SMIRNOV	CNRS Reseacher, University of Lille 1, Lille (France)

<u>Examiners</u>

Alex HANNON	Research Engineer, ISIS Facility, Didcot (England)
Olivier MASSON	Professor, University of Limoges, Limoges (France)
Philippe THOMAS	CNRS Research Director, University of Limoges, Limoges (France)

“Inspiration exists, but it has to find you working.”

Pablo Picasso

“ Все равно истины нет на свете или, быть может, она и была в каком-нибудь растении или в героической твари, но шел дорожный нищий и съел то растение или растоптал гнетущуюся низом тварь, а сам умер затем в осеннем овраге, и тело его выдул ветер в ничто. ”

Андрей Платонов, “Котлован”

To my grandpa.

Remerciements (Acknowledgements)

Je remercie vivement Monsieur Pierre BORDET, Directeur de Recherche CNRS à l'Université Joseph Fourier, et Monsieur Konstantin SMIRNOV, Chargé de Recherche CNRS à l'Université de Lille 1, d'avoir accepté le rôle important de rapporter ce manuscrit. Je remercie également Monsieur Alex HANNON, Ingénieur de Recherche à l'ISIS Facility, d'avoir accepté le rôle d'examinateur. Je remercie tous les membres du jury d'avoir assisté à la soutenance des travaux de ma thèse et d'avoir développé une discussion fructueuse et intéressante.

Le travail de thèse présenté dans ce manuscrit a été réalisé au laboratoire de Science des Procédés Céramiques et de Traitements de Surface (SPCTS), unité mixte de recherche du CNRS n° 7315, à Limoges. Je tiens à remercier Monsieur Thierry CHARTIER, directeur du SPCTS, de m'avoir accueillie au sein du laboratoire.

Je remercie également mes collègues russes Mikhail SMIRNOV et Andreï MIRGORODSKI de leur implication dans ma rencontre avec ce laboratoire.

Je remercie vivement mes collègues du SPCTS et de l'Axe 3 en particulier de m'avoir accueillie chaleureusement. C'est grâce à Philippe THOMAS qui a créé et qui entretient cette ambiance amicale dans notre groupe. Merci Philippe pour ton attention et ta sollicitude ! Tu étais mon 'papa' du laboratoire (et pas seulement. . .)!

Il faut noter le travail du secrétariat représenté par Virginie REYTIER, Nadine TCHEFRANOFF, Martine SEGEAR et Paméla BATHIAS et leur aide en ce qui concerne des questions administratives quotidiennes. Sans vous nous n'aurions pas pu avancer dans la recherche !

Ces trois années de contrat doctorat n'étaient que pour la thèse. C'était le temps d'apprendre une nouvelle culture, une nouvelle langue, de nouveaux paysages, une nouvelle cuisine, etc. . . Tout cela j'apprenais avec de l'aide et gràce aux gens qui m'entouraient. Avec le recul, je dirais maintenant que je vivais dans une pitite (!) ville tranquille et sympathique, au coeur de la campagne belle et apaisante, à côté des gens bien différents mais toujours intéressants. Je voudrais remercier mes collègues qui ont participé à mes découvertes de la vie française et qui ont fait partie de ces découvertes: Fabien REMONDIERE, Julie CORNETTE, Jean René DUCLERE, Jenny JOUIN, Marie LASGORCEIX, Laura MOLINA, Solène LE BRAS, Mickaël REICHMANN, Jayanth CHANNAGIRI, Florian JEAN, Abid BERGHOUT, Maggy COLAS, Antoine PLAT, Anthony BERTRAND, Richard MAYER, Chantal DAMIA, Aénor PONS. Je remercie également Claire BONHOMME, Alexandre BOULLE, Pierre CARLES, Julie CARREAUD, Cyril DANGLADE, Gaëlle DELAIZIR, Damien DI MARCO, Déborah DOMPOINT, Jesse GAMBE, Nabila GHRIBI, David HAMANI, Olivier NOGUERA, Laura PORTAL. Personne n'a traversé ma vie sans y avoir laissé une trace.

J'adresse des remerciements particuliers à Olivier MASSON qui m'a guidée pendant ces trois années. Il est très difficile de surestimer son apport au travail de ma thèse. Je suis pleinement consciente de la chance que j'ai eue d'avoir rencontré ce chercheur passionné, cet homme compréhensif, réjoui et très sympathique.

Un grand merci à vous tous, et que les oubliés me pardonnent !

Contents

List of Figures

List of Tables

List of Acronyms

ADP **A**tomic **D**isplacement **P**arameter

BO **B**ridging **O**xygen

FC **F**ast **C**ooling configuration

FCC **F**ace-**C**entered **C**ubic

IR **I**nfra-**R**ed

LF **L**eap**F**rog

LP **L**one **P**air

MAS–NMR **M**agic **A**ngle **S**pinning – **N**uclear **M**agnetic **R**esonance

MD **M**olecular **D**ynamics

NBO **N**on-**B**ridging **O**xygen

NMR **N**uclear **M**agnetic **R**esonance

NPT Ensemble with constant particles number (**N**), system pressure (**P**) and temperature (**T**)

NVE Microcanonical ensemble with constant particles number (**N**), system volume (**V**) and total energy (**E**)

NVT Ensemble with constant particles number (**N**), system volume (**V**) and temperature (**T**)

PBC **P**eriodic **B**oundary **C**onditions

PDF **P**air **D**istribution **F**unction

RMC **R**everse **M**onte **C**arlo

RT **R**oom **T**emperature

SC **S**low **C**ooling configuration

tbp **t**rigonal **bip**yramid

tp **t**rigonal **p**yramid

WKM	**W**arren, **K**rutter and **M**orningstar
XRD	**X**-**R**ay **D**iffraction

General introduction

The development of non-linear optical devices, such as up-conversion frequency systems and high speed optical-switches, has induced a great interest for materials exhibiting high linear and non-linear optical properties. Among these materials, the inorganic glasses based on the heavy metals are very interesting for application as systems with fast linear and non-linear optical response on the one hand and weak absorption on the other hand. Even if they do not have an optimal non-linear performance compared to some crystals or organic polymers, they present a commutation times significantly smaller (of picosecond or femtosecond order) than their concurrents (of nanosecond order).

Tellurium oxide-based glasses are among the most promising candidates, since their non-linear properties are the highest among the known oxide glasses. In particular their susceptibilities $\chi^{(3)}$ are 50–100 times higher than glassy SiO_2.

The origin of these properties, which is of great interest for material science, has been early attributed to the electronic ($5s^2$) lone pair (LP) of tellurium (IV) atoms when bonded to oxygen atoms. Recent works however suggest that the structure of the glass itself and in particular the nature of the Te–O–Te bridges is responsible to a large extend for these particular features.

Tellurium dioxide is known as a conditional glass former and requires fast-quenching techniques to form a glass. The resulting amorphous material is not stable to devitrification, but could be stabilised by adding modifier oxides. This is contrary to classical glass formers such as SiO_2, P_2O_5 and B_2O_3, where the modifiers usually break the glass network. But at the same time, the addition of modifiers oxides into TeO_2 system degrades the desired optical properties. A better understanding of these phenomena thus requires a good knowledge of the glass structure. The work on the pure amorphous TeO_2 system has been represented very poorly in the literature to date. The main aim of this work is to improve the knowledge of the structure of pure tellurium dioxide glass.

This study has been extended to the case of the disordered $\delta-TeO_2$ phase, which is formed during the crystallisation process of the TeO_2 glass. This phase is very interesting more from the fundamental point of view. It was discovered at the SPCTS laboratory about 15 years ago and seems to be similar to anti-glass phases described by Trömel *et al.* [1]. The description of $\delta-TeO_2$ phase made only with experimental techniques (X-ray diffraction and Raman spectroscopy) is incomplete.

The structural study of TeO_2 glass and $\delta-TeO_2$ phase requires the use of appropriate experimental techniques such as X-ray total scattering coupled with atomistic simulation methods such as molecular dynamics. The *ab initio* molecular dynamics methods are limited by the size of the simulated system and the simulation time. The classical molecular dynamics requires the knowledge of the interatomic potentials for a given system, and there are no established potentials for TeO_2 system in the literature.

The development of the empirical interatomic potentials for TeO_2 system is a very complicated problem. The local tellurium atom environment strongly varies in different structures. Tellurium atom can be three-, four-, five- and even six-coordinated in mixed TeO_2-based compounds, and the Te–O bond lengths and O–Te–O bond angles can vary in very large ranges (1.8 – 2.2 Å and 80 – 170° respectively for structures considered in this work). So it is a great challenge to derive the potentials for such a system as they should be highly transferable in order to represent all possible TeO_x units. A model should take into account such physical-chemical peculiarities as stereo-chemical active electronic lone pair of Te^{IV} atom when bonding to oxygen atoms, polarisability of oxygen atoms, covalency of Te–O bond, etc.

This work is organised as follows.

The first chapter is consecrated to the description of the investigated materials and structural characterisation methods. In the first part we consider the structure and the local Te^{IV} atom environment in pure and several mixed TeO_2 polymorphs. We demonstrate that the Te^{IV} atom coordination varies for different pure TeO_2 polymorphs and with the addition of modifiers oxides. We then overview the literature on the TeO_2-based glasses and $\delta-TeO_2$ phase. In the second part we give a necessary theoretical background for the experimental and simulation methods used in this work.

In the second chapter we report the results on the synthesis of $\gamma-$ and $\delta-TeO_2$ polymorphs. They are metastable phases difficult to obtain without secondary $\alpha-TeO_2$ phase. We performed X-ray diffraction and Raman spectroscopy measurements with temperature for four glassy systems: $92.5\%TeO_2 + 7.5\%WO_3$, $90\%TeO_2 + 10\%WO_3$, $95\%TeO_2 + 5\%NbO_{2.5}$, and $95\%TeO_2 + 5\%PbO$. We then report a method for obtaining the pure samples of $\gamma-$ and $\delta-TeO_2$. We propose a hypothesis explaining the mechanism of pure samples formation and perform X-ray diffraction, Raman spectroscopy and differential scanning calorimetry characterisation in order to test it.

The third chapter is consecrated to the development of interatomic potentials for the TeO_2 system. In this chapter we discuss the role of tellurium and oxygen atoms polarisation, Te–O and O–O pair interactions in the formation of various Te^{IV} coordinations. We then apply the derived potentials to several mixed TeO_2-based systems and investigate the potentials transferability. In such a way we convince ourselves that various tellurium atom environments could be well modelled and that the potentials are appropriate for application to molecular dynamics simulations of TeO_2-based disordered systems.

Finally, in the fourth chapter we use the results obtained in all previous chapters in order to investigate the structures of the pure TeO_2 glass and the $\delta-TeO_2$ polymorph. For the glass we perform the molecular dynamics simulations and compare the results with the neutron scattering data obtained in our group earlier. For $\delta-TeO_2$ phase we perform both the X-ray total scattering experiment and molecular dynamics simulations. The analysis of the obtained simulations data was performed with the help of self-made programs.

Chapter 1

Presentation of the investigated materials and structural characterisation methods

1.1 Crystalline polymorphs and TeO_2-based glasses

1.1.1 Te(IV) atom environments in pure TeO_2 polymorphs

Tellurium dioxide is present in various polymorphic forms. The various polymorphs identified and characterised at this time are following. The $\alpha-TeO_2$ (paratellurite) is a stable at ambient pressure and temperature phase [2, 3, 4, 5]. The natural form of the tellurium dioxide is β variety [6]. It is metastable and transforms irreversibly to α variety at 600 °C. Worlton *et al.* [7] reported a high pressure (19.8 kbar) TeO_2 polymorph, which corresponds to an orthorhombic deformation of $\alpha-TeO_2$ polymorph. The $\gamma-$ and $\delta-TeO_2$ are the metastable phases obtained during crystallisation of TeO_2-rich glasses [8, 9, 10, 11, 12]. They also transform irreversibly to $\alpha-TeO_2$ at temperature about 450 °C.

In this section we will regard the environments of tellurium (IV) atoms in crystalline $\alpha-$, $\beta-$, $\gamma-$ and $\delta-TeO_2$ polymorphs. We are particularly interested in the γ polymorph, as in our group it is considered as the crystalline structure closest to glass, and in δ polymorph, as it seems to represent a class of "anti-glasses" reported by Trömel *et al.* [1] and has never been thoroughly investigated.

1.1.1.1 $\alpha-TeO_2$ polymorph

The most studied TeO_2 polymorph is α-TeO_2. Its structure was thoroughly investigated by X-ray diffraction methods and described in 1986 by I.P.Kondratyuk [4] and in 1988 by P.A. Thomas [5]. The work of Kondratyuk reports the P 4_32_12 space group and cell parameters: $a = b = 4.810$ Å and $c = 7.613$Å.

It is often described with TeO_4 disphenoids connected in chains (Fig. 1.1a). In the disphenoid shown in Fig. 1.1b two equatorial bonds are shorter (1.879 Å) and two axial bonds are longer (2.121 Å). Each oxygen atom is connected with two tellurium atoms by one axial bond and one equatorial bond. The interconnection of the disphenoids by the vertexes allows to describe a three-dimensional network of the paratellurite phase. Hence, the tellurium atoms are connected *via* the asymmetrical Te–O–Te bridges.

When considering the more distant oxygen atoms (2.867 Å), we get a strongly distorted octahedral environment of Te atoms, so that α-TeO_2 can be thought of as a derived from rutile-type structure.

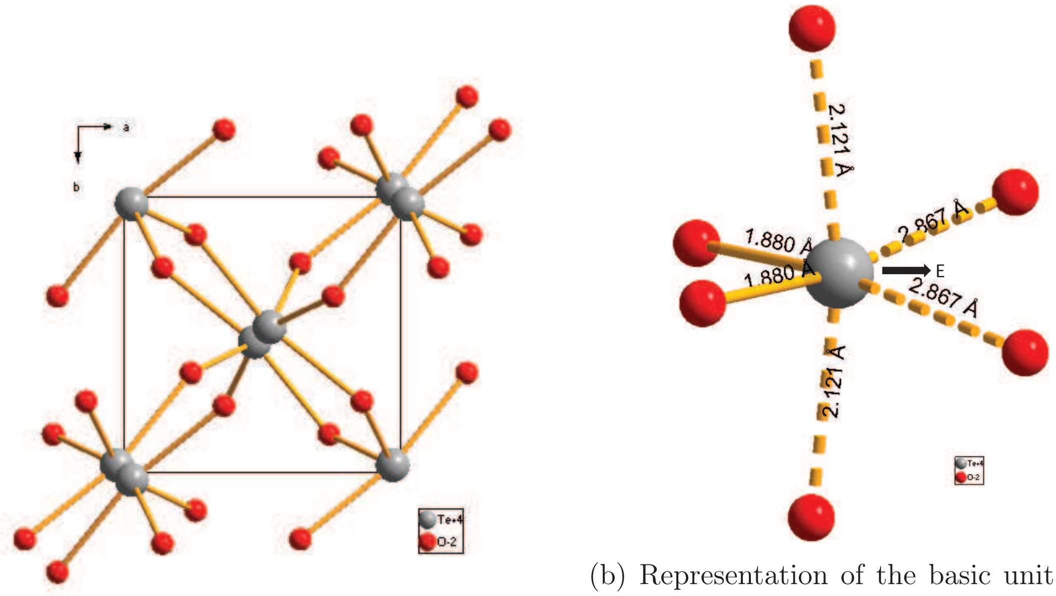

(a) Projection along the c-axis.

(b) Representation of the basic unit. The arrow points the LP (E) direction, solid lines represent the short and intermediate bonds (< 2.02 Å) and dashed lines represent the long bonds (> 2.02 Å).

Figure 1.1: The structure of $\alpha-TeO_2$.

1.1.1.2 $\beta-TeO_2$ polymorph

This is the natural form of tellurium dioxide, which transforms irreversibly to α variety at 600 °C. The β-TeO_2 polymorph crystallises in a orthorhombic system with the space group P*bca* and the cell parameters: $a = 12.035$ Å, $b = 5.464$ Å and $c = 5.607$ Å [6].

This phase can also be described with TeO_4 disphenoid. However, in this phase two shorter equatorial bonds and two longer axial bonds do not have the same lengths. The Te–O distances are 1.877 Å and 1.927 Å for the equatorial bonds and 2.070 Å and 2.196

Å for the axial bonds. The interconnection of TeO_4 units in this phase is different from the α-TeO_2 phase. The units are alternatively connected *via* a common vertex and an (axial-equatorial) edge forming the folded layers parallel to the (1 0 0) plane. Hence, in the $\beta-TeO_2$ polymorph the tellurium atoms are connected *via* the double Te–O–Te bridges.

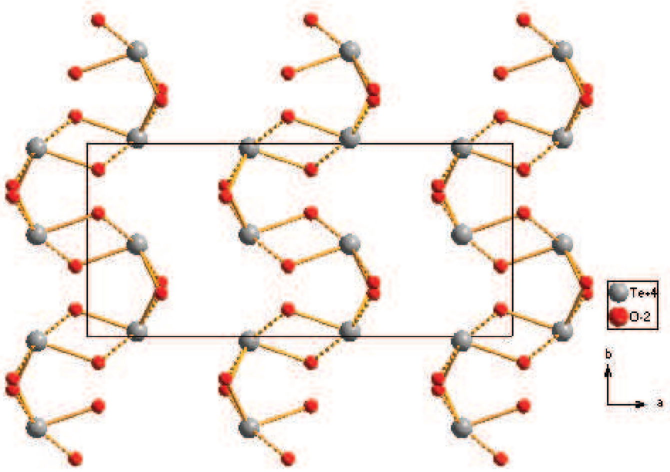

(a) Projection in $c-$axis direction.

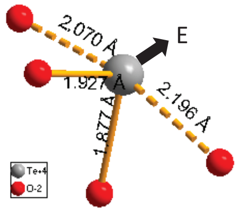

(b) Representation of the basic unit. The arrow points the LP (E) direction, the solid lines represent the short and intermediate bonds ($<$ 2.02 Å) and dashed lines represent the long bonds ($>$ 2.02 Å).

Figure 1.2: The structure of $\beta-TeO_2$.

1.1.1.3 $\gamma-TeO_2$ polymorph

The metastable γ-TeO_2 polymorph was discovered at the SPCTS laboratory in 1999 [8]. It was obtained as the result of the crystallisation of TeO_2-rich glasses within TeO_2–WO_3 and TeO_2–Nb_2O_5 systems. The γ-TeO_2 polymorph is characterised by orthorhombic system (space group P 21 21 21) with Z = 4 TeO_2 units per unit cell and cell parameters: a = 4.898 Å, b = 8.576 Å and c = 4.351 Å (Fig. 1.3a).

The three-dimensional structure of γ-TeO_2 polymorph can be described with TeO_4 disphenoid reported in Fig. 1.3b. This disphenoid, however, is strongly deformed with respect to the one in $\alpha-$ polymorph. The Te–O distances are 1.859 Å and 1.948 Å for the equatorial bonds and 2.019 Å and 2.197 Å for the axial bonds. The one of the two axial bonds (Te–O$_1^1$=2.197 Å) is much longer than the other one (Te–O$_2^1$=2.019 Å). This type of structural unit is usually assigned a notation TeO_{3+1} as an intermediate between TeO_4 trigonal bipyramid (tbp) and TeO_3 trigonal pyramid (tp). Such intermediate units occur quite often in mixed tellurium oxides (a detailed study of TeO_x units distribution could be found in the PhD thesis of D. Hamani [13]).

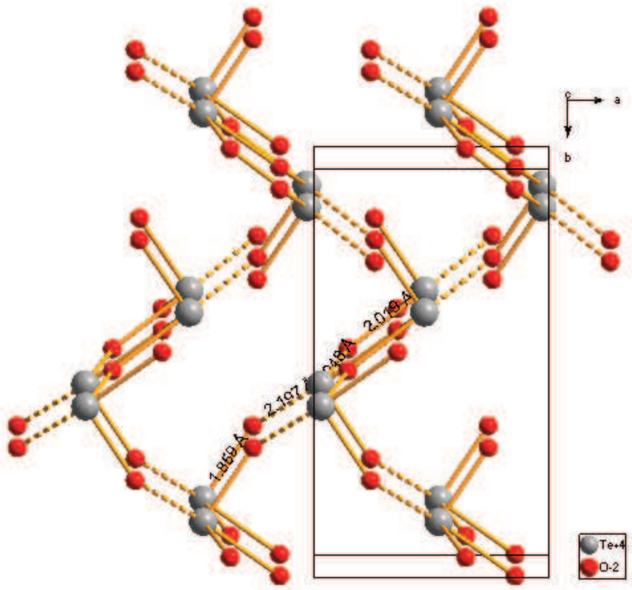

(a) Three-dimensional view.

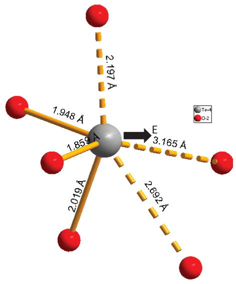

(b) Representation of the basic unit. The arrow points the LP (E) direction, the solid lines represent the short and intermediate bonds (< 2.02 Å) and dashed lines represent the long bonds (> 2.02 Å).

Figure 1.3: The structure of $\gamma-TeO_2$.

The TeO_4 structural units in γ-TeO_2 are connected by the vertexes creating the zigzag chains and large tunnels. The tellurium atoms LPs (E) are directed towards the centres of these tunnels. The tellurium atoms are connected *via* Te–$_{eq}O_{ax}$–Te bridges like in

α−TeO_2. However, in contrast to α−TeO_2, in γ-TeO_2 there are two types of bridges: essentially asymmetrical (1.859 Å – 2.197Å) and almost symmetrical (1.948 Å – 2.019 Å).

1.1.1.4 δ−TeO_2 polymorph

The δ−TeO_2 polymorph is the less studied polymorph among all the pure TeO_2 structures. It was discovered at the SPCTS laboratory about 15 years ago [9, 14, 10, 11, 12]. The δ−TeO_2 has never been obtained from pure TeO_2 glass, but was successfully synthesised from glassy samples containing 5–10 mol % of WO_3 or 2.5–10 mol % of Nb_2O_5. Its X-ray diffraction (XRD) pattern (Fig. 1.4) could be unambiguously indexed with a cubic cell (F $m\bar{3}m$, a = 5.690(1) Å) and its unit cell contains four TeO_2 units. However, the description of this structure with fluorite model is inconsistent. Indeed, an ideal fluorite structure with a cell parameter a = 5.690(1) Å requires Te–O bond lengths of about 2.464 Å, which is much larger then the usual Te–O bond lengths (~1.8–2.2 Å). In addition, each cation is coordinated by eight anions, whereas in all known tellurites, Te(IV) atom is commonly coordinated by three or four oxide ions. The unit cell and basic structural unit of idealised δ−TeO_2 polymorph are presented in Fig. 1.5a and 1.5b.

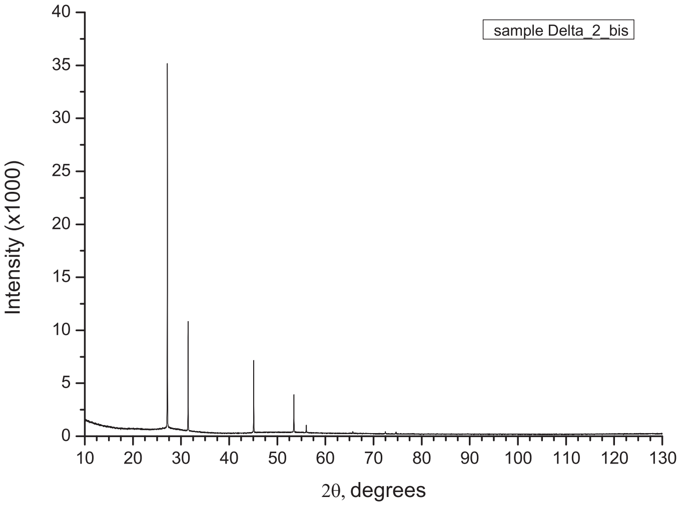

Figure 1.4: XDR powder diagram of the δ−TeO_2 obtained.

The aspects discussed above bring us to comparison of δ−TeO_2 polymorph with the cubic phase (a = 5.54 Å) formed within the $15K_2O$-$15Nb_2O_5$-$70TeO_2$ system [15], the anti-glass phases and other lanthanoid tellurites IV (a = 5.49 – 5.7 Å reported by Trömel *et al.*) [1], and a metastable β polymorph of $Bi_2Te_4O_{11}$ (a = 5.64 Å) [16]. The last one was studied by Masson *et al.* in [17] by both neutron powder diffraction and reverse Monte Carlo modelling (RMC). The authors showed that the cations form a fairly well-defined

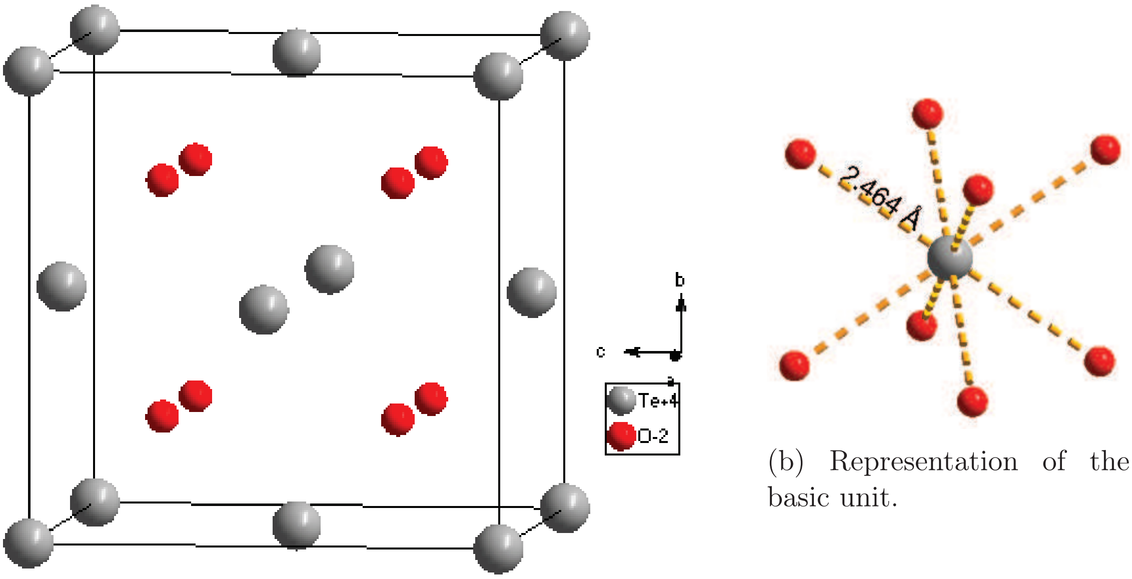

(a) Three-dimensional view.

(b) Representation of the basic unit.

Figure 1.5: The structure of the ideal fluorite $\delta-TeO_2$ model.

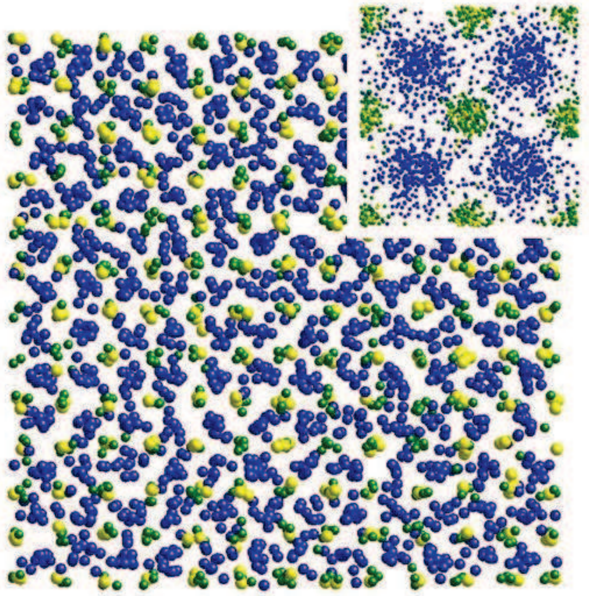

Figure 1.6: The RMC model of $\beta-Bi_2Te_4O_{11}$ and its average structure (upper right corner) with Te/Bi atoms in green and O atoms in blue.

FCC lattice, whereas the oxygen sub-lattice is very disordered (positional disorder). It was also shown that $\beta-Bi_2Te_4O_{11}$ consists of mainly TeO_3 and TeO_4 polyhedra connected in a conner-sharing way, contains long cooked and branched chains, rings and few double oxygen bridges. The RMC model model of $\beta-Bi_2Te_4O_{11}$ is reported on Fig. 1.6. A similar model could have described the average structure of $\delta-TeO_2$.

1.1.2 TeO_2-based glasses

The structure of modified TeO_2-glasses has been relatively well investigated by different techniques: Infrared (IR) and Raman spectroscopy [18, 19], Magic Angle Spinning (MAS)–Nuclear Magnetic Resonance (NMR)[20, 21], NMR, Neutron and X-ray diffraction combined with Reverse Monte Carlo (RMC) simulations [22, 23, 24, 25]. These studies describe the tellurite glasses as complex systems composed of various TeO_x structural units with either bridging oxygens (BO) or non bridging oxygen (NBO) atoms. These units are described in terms of Q_m^n units, where m is the total number of BO and NBO atoms (within a chosen R_{cutoff}) and n is the number of BO atoms. More precisely, the authors in [22, 23] established that the presence of five tellurite polyhedra (Q_3^0, Q_3^1, Q_3^2, Q_4^3, Q_4^4, see Fig. 1.7) in the glass model is necessary to achieve a good agreement between experimental data and RMC model of modified TeO_2 glasses. All these Q_m^n polyhedra are found in modified tellurite crystals, whereas the pure TeO_2 polymorphs (α- and γ-TeO_2) consist of only Q_4^4 and Q_{3+1}^4 units, as we saw in previous sections.

The work on the pure amorphous TeO_2 system has been represented with only few studies in the literature to date [26, 27, 28, 29, 30, 31]. Let us now consider only two of them. The first one is in an *ab initio* molecular dynamics (MD) studies by Pietrucci *et al.* [26]. These authors report a glass model that consists of various Q_m^n units like those determined by RMC modelling, but also of other Q_3^3 and Q_5^5 units, and Q_3^3 units make up an important contribution (20.4 %) in Q_m^n population. Also the authors report the presence of 14% of terminal oxygen atoms, which does not fit well with the continuous glass network model of Zachariasen [32]. The second work on pure amorphous TeO_2 system by Barney *et al.* [27] is based on recent neutron diffraction experiment. The authors made the precise measurements of tellurium coordination number n_{TeO} and obtained a value 3.68(4), that implies that the glass structure is formed from about 2/3 four-coordinated units and 1/3 three-coordinated units, that gives, in turn, about 16% of terminal oxygen atoms. Further they propose a simple connectivity model for the glass, where TeO_3 and TeO_4 units in ratio 1 : 2 form the rings like in crystalline $K_2Te_4O_9$ structure.

These results are highly unusual and require deeper understanding. However, *ab initio* MD methods are limited in size of simulated system and simulation time. The glass model in [26] consisted of only 32 TeO_2 units and was obtained as a result of 16 ps cooling the liquid at a rate of ≈ 10^{14} K/s. The authors themselves consider that such a high concentration of NBO atoms might be due to a too high cooling rate used in *ab initio* MD simulation. In other words, the system might have not reached a fully equilibrated glass structure and resembles more a frozen liquid.

In contrast, classical MD allows bigger size-scale and longer time-scale simulations in comparison with *ab initio* MD and is chosen in this work as an atomistic simulations method for TeO_2-based glasses structure.

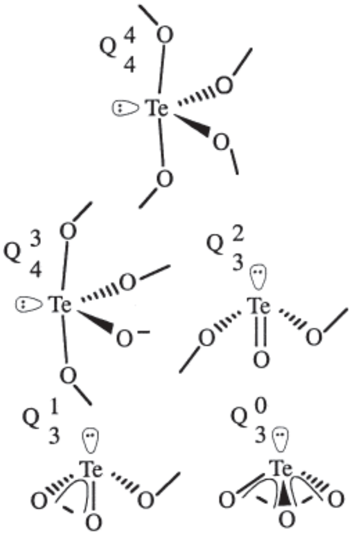

Figure 1.7: Structural units Q_m^n found in tellurite crystals, where m is the number of bonded oxygen atoms and n is the number of bridging oxygen atoms. Taken from [22]

1.1.3 Environments of the Te(IV) atom found in tellurite materials

In Sec. 1.1 of this chapter we reviewed the local environment in some TeO_2-based materials ($\alpha-$, $\beta-$, $\gamma-$ and $\delta-TeO_2$ pure polymorphs and TeO_2-based glasses). Contrary to silicates, for example, the local arrangement is influenced by a high stereo-chemical activity of the Te(IV) electronic LP and differs from one pure polymorph to another. Moreover, in $\delta-TeO_2$ polymorph and glasses the local Te(IV) atom environment remains not really clear.

Although, we did not consider the mixed TeO_2-based compounds, it is worth noting, that the local environment strongly varies when adding modifiers. The detailed study of Te(IV) atom environment variation with modifiers edition is reported in the PhD thesis of D. Hamani [13], which comprises an overview of more than 100 TeO_2-based compounds and develops a new nomenclature for TeO_x units and some regularities in Te(IV) atom coordination.

Many authors propose that the TeO_2-based structures consist of the TeO_4, TeO_{3+1} and TeO_3 units and their proportion depends on the quantity of the added modifier oxide [33, 18, 34, 35, 36]. The TeO_4 unit (disphenoids) transforms to the TeO_3 units *via* the intermediate TeO_{3+1} units, which causes the decrease of BO atoms quantity and leads to the change of Te coordination number from 4 to 3.

However, the TeO_4 to TeO_3 transformation is not general case. We will give here the examples of two peculiar cases of Te(IV) atom coordination. These are the $BaTe_2O_6$ and $Cs_2Te_4O_{12}$ structures with atypical symmetrical environment of Te(IV) atom. Fig. 1.8 and Fig. 1.9 show the unit cell and Te(IV) atom coordination for $BaTe_2O_6$ and $Cs_2Te_4O_{12}$ structures respectively. In the $BaTe_2O_6$ structure Te(IV) atom is coordinated to five oxygen atoms, where four of them form a square pyramid with edge of 2.126 Å and the fifth bond is much shorter (1.830 Å). The LP points in the opposite direction of the shortest bond. In the $Cs_2Te_4O_{12}$ structure Te(IV) atom is located in the centre of a perfect octahedron TeO_6 formed with six oxygen atoms (distance Te–O = 2.112 Å) and Te LP does not present any stereochemical activity (i.e. the LP is not polarised).

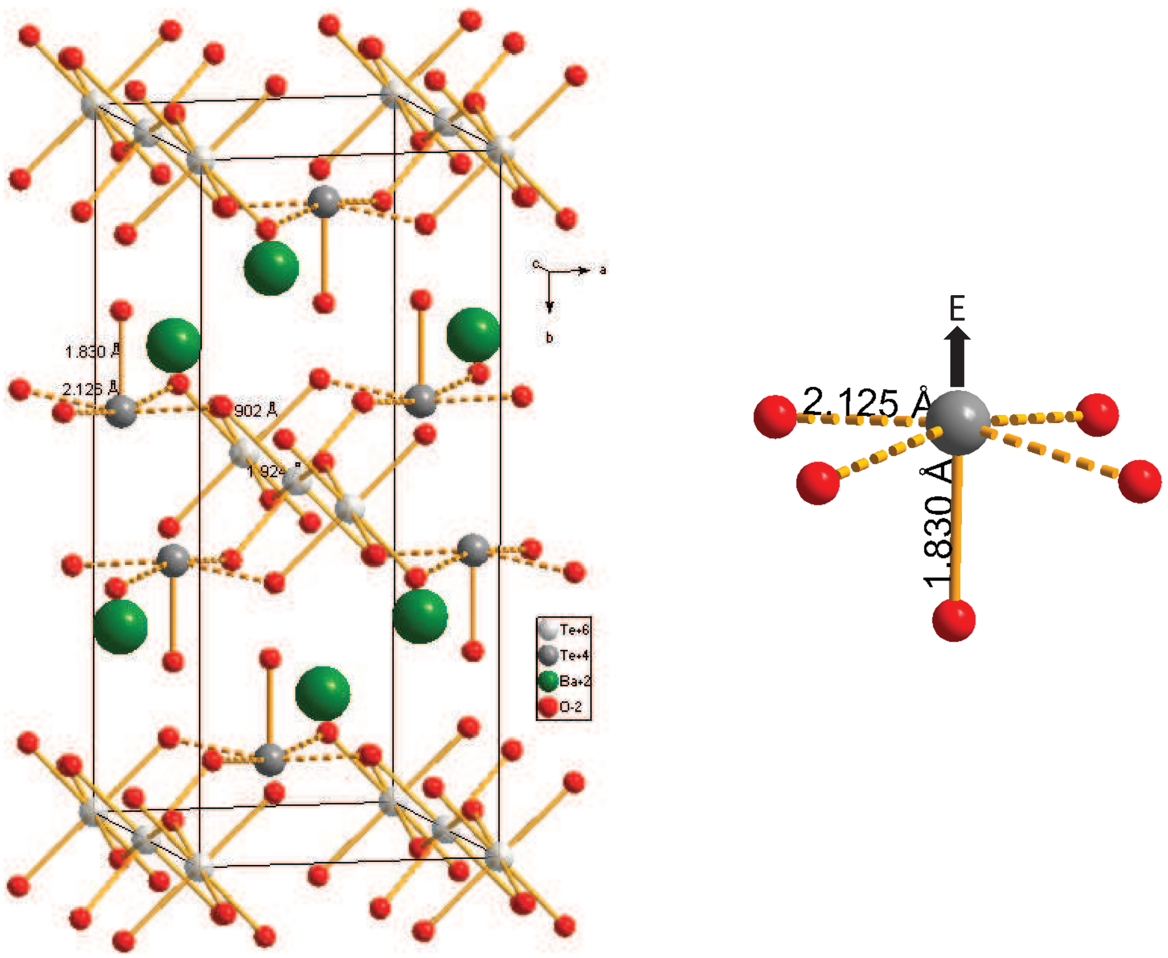

Figure 1.8: Spacial view of the $BaTe_2O_6$ structure unit cell and its Te(IV) atom environment. Te(IV) atoms are represented in deep grey, Te(VI) atoms in light grey, O atoms in red and Ba atoms in green. The arrow points the LP (E) direction, solid lines represent the short and intermediate bonds (< 2.02 Å) and dashed lines represent the long bonds (> 2.02 Å).

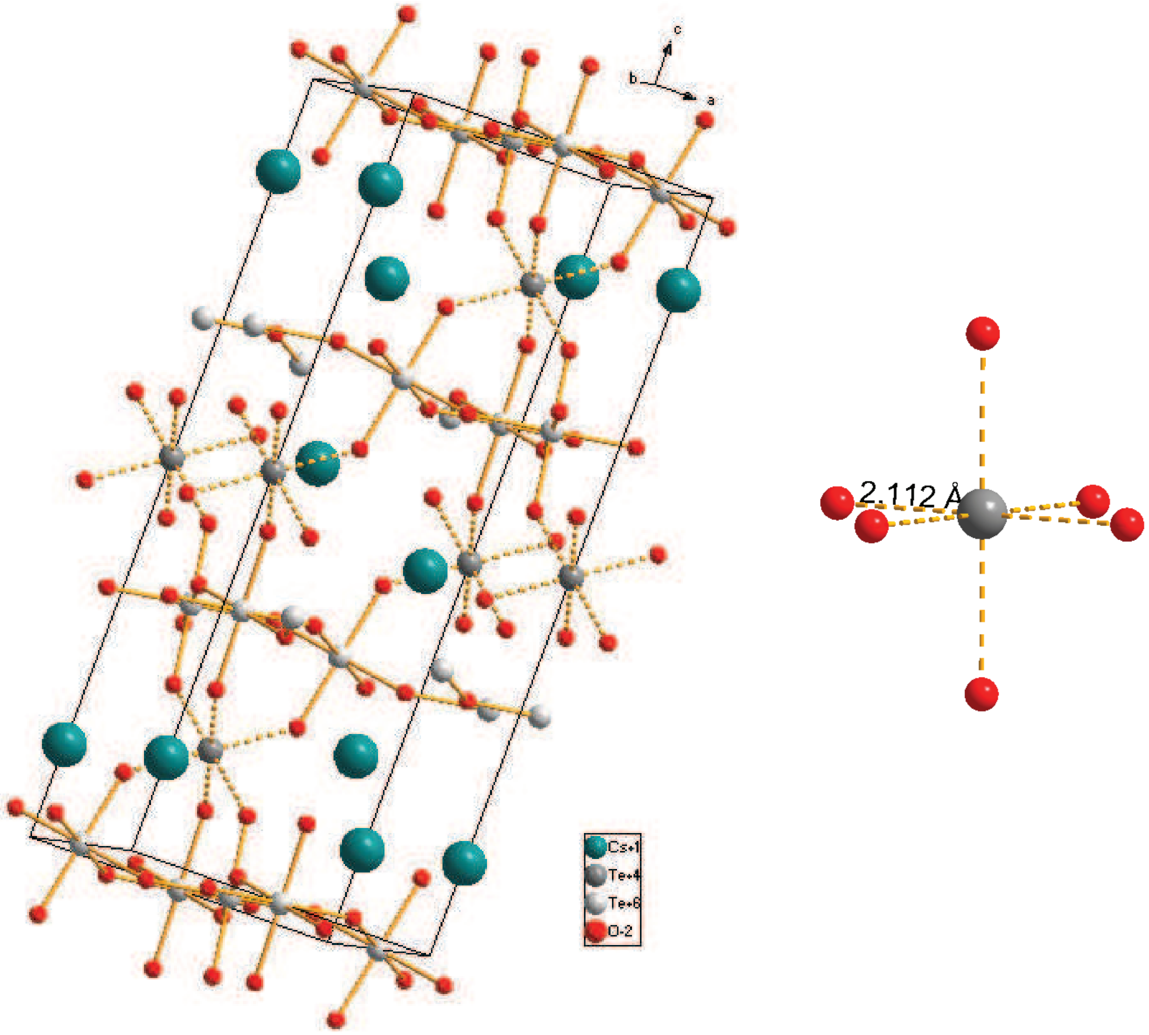

Figure 1.9: Spacial view of the $Cs_2Te_4O_{12}$ structure unit cell and its Te(IV) atom environment. Te(IV) atoms are represented in deep grey, Te(VI) atoms in light grey, O atoms in red and Cs atoms in teal. Solid lines represent the short and intermediate bonds (< 2.02 Å) and dashed lines represent the long bonds (> 2.02 Å).

1.2 Structure characterisation using the simulation methods

The problem of performing MD simulations falls into two parts: firstly, it is necessary to establish the way the atoms interact with each other, *i.e.* the interatomic potential (IAP) and then we can proceed to MD simulation itself. There are already established IAPs for a number of element pairs, which could be found in literature as for example in the IAP data base composed by the Department of Chemistry of University College London staff [37]. However, for the element pairs of our interest (Te, O) the IAP does not exist. For this reason, we consecrate the first part of this section to background of IAP derivation methods. In the second part of this section we will recall general MD method background and consider particular algorithms, models and features used in this work.

1.2.1 Interatomic potential derivation: presentation of the methodology

When deriving an IAP, it is necessary to take into account all physical peculiarities of studied material. For TeO_2 system we have to consider the Te–O bond covalency, stereoactivity of tellurium IV electronic LP, strong polarisability of both Te and O atoms. Also an accurate IAP should be transferable, *i.e.* able to describe such a large bond lengths distribution presented in TeO_2-based materials and flexible enough to reproduce correspondingly large bond-angles distribution and different coordination numbers. Hence, it is important to chose an appropriate form of the IAP and atomic model.

To our knowledge the IAPs for pure TeO_2 system have never been presented in the literature. The only work reported the classical MD simulations for TeO_2 system is MD simulations of ZnO–TeO_2 glasses [38]. The authors used the three-body IAP for Te–O interaction, which could have prevented them to reproduce all the variety of TeO_x structural units by fixing the minimum of potential energy at a certain angle value. In addition, the envelope of the resulting pair distribution function (PDF) does not fit very well experimental data in medium-range order (3–6 Å). The PDFs obtained in [38] are reported in Fig. 1.10.

1.2.1.1 Potential form

The IAPs were derived in the framework of the Born model of solids, in which the lattice is constructed as an infinite array of charged spherical ions. The total potential energy U_{tot} for the interaction between two ions i and j is given as

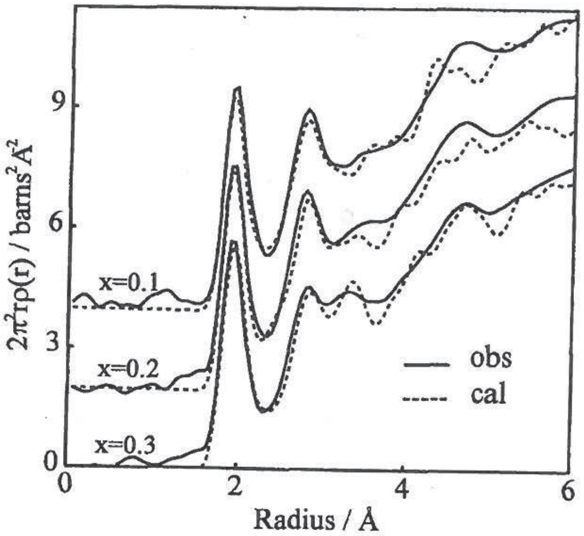

Figure 1.10: Comparison of the PDFs derived from glass structure models of MD construction (dotted lines) and those obtained by neutron diffraction (solid lines) for xZnO–(1–x)TeO$_2$ glasses (x = 0.1, 0.2, 0.3). Taken from [38].

$$U_{tot} = U_{coul} + U_{sr}. \tag{1.1}$$

The first term represents the long range Coulombic interaction

$$U_{coul}(r_{ij}) = \frac{q_i q_j}{4\pi\epsilon_0}\frac{1}{r_{ij}} \tag{1.2}$$

with q_i for the ion charge on species i and r_{ij} for the interatomic distance between ion i and ion j. The second term U_{sr} is the short-range interaction energy, which has both repulsive and attractive components (see Fig. 1.11).The Buckingham potential model has previously proved to be successful in modelling of various materials [39, 40] and was chosen in this work:

$$U_{sr}(r_{ij}) = Ae^{-r_{ij}/\rho} - Cr_{ij}^{-6} \tag{1.3}$$

where the A parameter can be approximated as a measure of a number of electrons within the ion; ρ can be approximated as a measure of the electron density and C is an approximate description of the polarisability of the ion [41]. However, sometimes a simple two-body potential form is not enough to correctly model the studied system. Thus, for example, when modelling the tetrahedral SiO$_4$ coordination, the angular forces are important and a simple harmonic function of bond angle [42] is often included in the model:

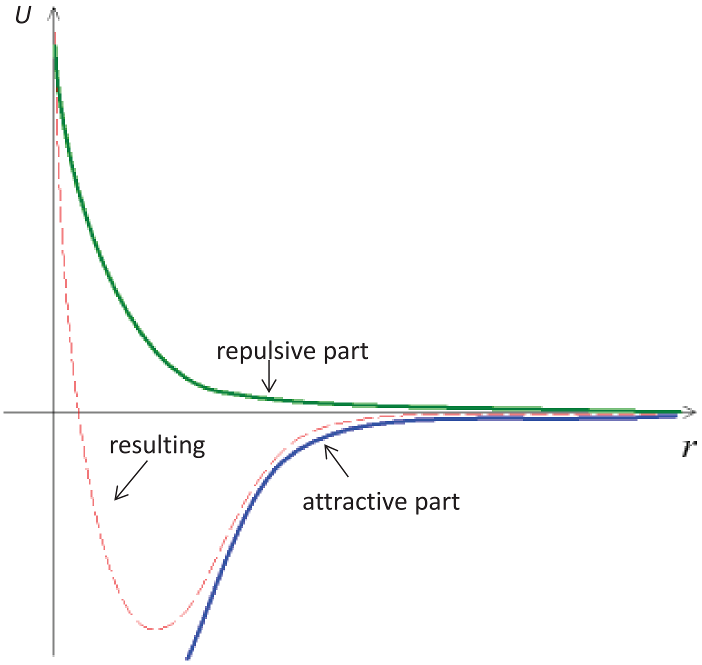

Figure 1.11: Interatomic potential energy of the pair of atoms resulting of repulsive and attractive components.

$$U(\theta) = \frac{1}{2}(\theta - \theta_0)^2, \tag{1.4}$$

where θ_0 is the nominal equilibrium angle (109.47° for a tetrahedral coordination).

1.2.1.2 Polarizability

All the functions for potential energy described above assume that ions are rigid. This means that the model does not allow for ionic polarisation in response to local electrical fields. In our case, as we will see later, neglecting the strong polarisation effect of Te (IV) electronic LP in tellurites would lead to failure in modelling of correct structure.

The simplest way to introduce the ion polarisation is the core-shell model, which was presented for the first time by Dick and Overhause [43]. Its schematic representation is reported in Fig. 1.12. In this model the atom is divided into a core and a shell, where all the atom mass is assigned to the core and the massless shell models the atom polarizability. The core and shell are Coulombicaly screened from each other, but coupled by a harmonic spring of force constant k_2^{cs}, which has a potential form [44]:

$$U_{cs} = \frac{1}{2}k_2^{cs}x^2 \tag{1.5}$$

where x is the core-shell distance. If the shell charge is q_s, then the polarisability of

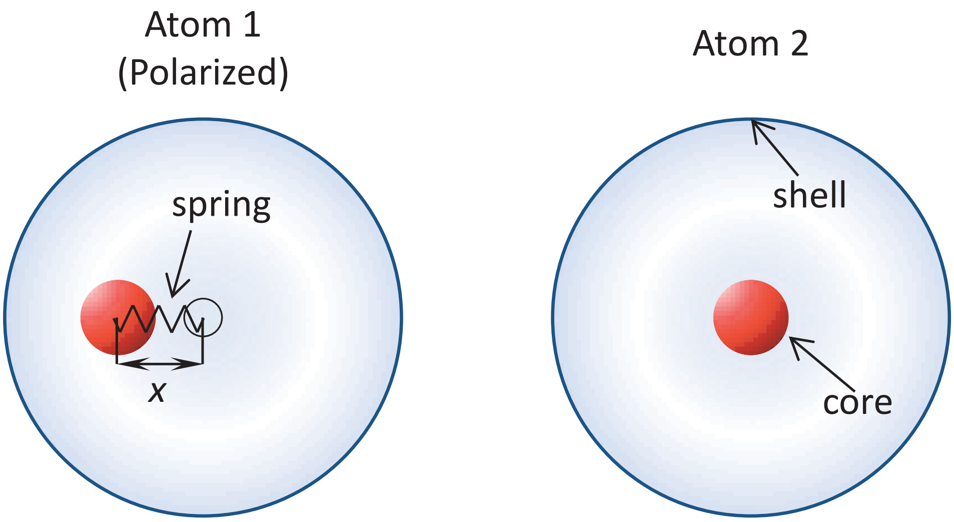

Figure 1.12: Schematic representation of core-shell model. The atom on the left is polarised, *i.e.* its shell is shifted with respect to the core at distance x.

the ion in vacuum in harmonic approach is given by

$$\alpha = \frac{q_s^2}{k_2^{cs}} \tag{1.6}$$

As J.D. Gale noted, it is impossible to distinguish from a phenomenological point of view between on site ion polarisation and charge transfer between ions. This may explain why the combination of formal charges with the shell model has been so successful for modelling materials that are quite covalent, such as silica polymorphs.

By convention, the short-range forces are specified to act on the shell, while the Coulomb potential acts on both the core and the shell, which is not the case in the present work, as we will see later.

In some cases an anharmonic spring can be used, which is quartic in form:

$$U_{cs} = \frac{1}{2}k_2^{cs}x^2 + \frac{1}{24}k_4^{cs}x^4 \tag{1.7}$$

One of the rare examples of using a higher-order constraining force on the core-shell interaction is discussed in details in [45]. Wojcik *et al.* claim that many of the published sets of shell model potentials for oxides exhibit an unphysical collapse when the anion-cation pair is allowed to attain its minimum energy configuration. They discuss the effect of adding a quartic term to the core-shell potential in the failed models and show that it could be a remedy to the problem of the pathological shell model ions. But there is no universal method because of the variety of effects on relative permittivities and elastic constants.

1.2.1.3 Transferability

In order to use all abilities of atomistic modelling with empirical IAP, the functions set for interaction between atoms of certain type should be transferable. This means that once the IAP is set for one system, we do not need to retune the model for each new application.

For example, supposing that we want to perform a calculation of some crystalline phase under pressure. If the model correctly reproduces the elastic constants, there is a chance that the low-pressure results will be reasonable. But once the bond lengths have changed appreciably, there is no guarantee at all that the model will match experiment because the model has not been tuned to reproduce the energy function for these new interatomic distances.

We can fall into the same trap in the case of tellurites but even at zero-pressure. As was discussed above, the range of the interatomic distances in tellurites is very large for different structures. The IAP model tuned for $\alpha-$TeO$_2$ (with Te–O bond lengths of 1.8795 Å and 2.121 Å) will not necessarily work for $\gamma-$TeO$_2$ (with Te–O bond lengths of 1.859 Å – 2.197 Å) or for a mixed compound like Cs_2TeO_3 (with Te–O bond lengths of 1.846 Å[46]). This problem becomes even more evident in glasses, where Te atom can have really diverse coordination.

In order to tackle this problem, we used two independent structural data values for $\alpha-$ and $\gamma-$TeO$_2$ polymorphs, which contain the bond lengths in the range 1.86–2.2 Å, and performed simultaneous tuning of the model. In such a way, these two phases comprise a large bond lengths range, which also includes the bond lengths in a majority of mixed TeO$_2$-based compounds.

1.2.1.4 Fitting of potential parameters

Empirical potential derivation consists in a least squares procedure, whereby the difference between experimentally observed and calculated properties is minimised. The sum of squares, F, is defined as follows:

$$F = \sum_{all\ observables} w(f_{calc} - f_{obs})^2 \tag{1.8}$$

where f_{calc} and f_{obs} are the calculated and observed quantities and w is a weighting factor. In this work we used a Newton-Raphson functional minimisation approach option in GULP software [47] to solve the least squares problem. We carried out empirical fitting to the experimental structural data.

Almost all properties of the material can be used in the derivation process, including elastic and dielectric constants, lattice energy and phonon data. However, it is often the case with empirical fitting that only the experimental crystal structural data is known. To improve the reliability and transferability of IAPs we used the elastic constants data as energy second derivative information. For α-TeO$_2$ we used the experimental elastic constants data [48] and for γ-TeO$_2$ the calculated ones by *ab initio* [49] and lattice dynamics [8] methods. For the other investigated TeO$_2$-based compounds only experimental structural data was considered.

1.2.1.5 Fit quality and stability of the system. Elastic constants criterion.

A fit is considered as "good" if it is able to reproduce the lattice parameters and interatomic distances within a small error with respect to experimental values. In this work we accepted an error of 5% and preferred, hence, the capability of IAPs to reproduce the diverse tellurium(IV) environments rather than very precise cell parameters.

When fitting the potential parameters, one has to ensure the stability of the optimised structure. We referred to two criteria of stability. Firstly, the calculated phonon modes should be positive. The frequencies are obtained through calculating the second derivatives of energy, which constitute the hessian matrix. The eigenvalues of this matrix correspond to squared harmonic frequencies of normal vibrations. Hence, a negative eigenvalue corresponds to an imaginary frequency. This means that corresponding normal coordinate has a negative curvature and the system has not reached a minimum of the potential energy.

The second criterion of stability is the elastic constants matrix. For a stable structure, elastic constants should satisfy the well-known Born-Huang stability criteria [50], namely, the energy density must be a positive definite quadratic form, so that the energy is raised by any small strains. This leads to the requirement that all the eigenvalues of elastic constant matrix should be positive. We report here the restrictions on the elastic constants for crystal systems in special cases, which were used in this work (from [50] and [51]).

Hexagonal crystals (C_{11}, C_{33}, C_{44}, C_{12} and C_{13} independent constants)

$$\begin{gathered} C_{44} > 0, C_{11} > |C_{12}|, \\ (C_{11} + 2C_{12})C_{33} > 2C_{13}^2 \end{gathered} \tag{1.9}$$

Tetragonal crystals (C_{11}, C_{33}, C_{44}, C_{66}, C_{12} and C_{13} independent constants)

$$\begin{aligned} C_{11} > 0, C_{33} > 0, C_{44} > 0, C_{66} > 0, \\ C_{11} - C_{12} > 0, C_{11} + C_{33} - 2C_{13} > 0, \\ 2(C_{11} + C_{12}) + C_{33} + 4C_{13} > 0 \end{aligned} \tag{1.10}$$

Orthorhombic crystals (C_{11}, C_{22}, C_{33}, C_{44}, C_{55}, C_{66}, C_{12}, C_{13} and C_{23} independent constants)

$$\begin{aligned} C_{11} > 0, C_{22} > 0, C_{33} > 0, C_{44} > 0, C_{55} > 0, C_{66} > 0, \\ C_{11} + C_{22} + C_{33} + 2(C_{12} + C_{13} + C_{23}) > 0, \\ C_{11} + C_{22} - 2C_{12} > 0, \\ C_{11} + C_{33} - 2C_{13} > 0, \\ C_{22} + C_{33} - 2C_{23} > 0 \end{aligned} \tag{1.11}$$

Monoclinic crystals (C_{11}, C_{22}, C_{33}, C_{44}, C_{55}, C_{66}, C_{12}, C_{13}, C_{23}, C_{15}, C_{25}, C_{35} and C_{46} independent constants)

$$\begin{aligned} C_{11} > 0, C_{22} > 0, C_{33} > 0, C_{44} > 0, C_{55} > 0, C_{66} > 0, \\ C_{11} + C_{22} + C_{33} + 2(C_{12} + C_{13} + C_{23}) > 0, \\ C_{33}C_{55} - C_{35}^2 > 0, \\ C_{44}C_{66} - C_{46}^2 > 0, \\ C_{22} + C_{33} - 2C_{23} > 0 \end{aligned} \tag{1.12}$$

1.2.2 Theoretical Background of Classical Molecular Dynamics Method

Molecular dynamics simulation consists in the numerical, step-by-step, solution of the classical Newtonian equations of motion. A general 'recipe' of its performance is quite simple: it suffices to define a starting configuration (*i.e.* atoms positions and velocities), the interatomic interaction within the system, the working conditions (temperature, pressure) and numerically solve the equations of motion. In this section we will briefly review how to embody this simple idea in terms of computational methods and algorithms. The more detailed discussion on MD theory can be found in the classic books of M.P. Allen and D.J. Tildesley *"Computer simulation of liquids"* [52] and in *"Molecular dynamics* *simulation"* by J.M. Haile [53].

1.2.2.1 Equations of motion

The first MD simulation was accomplished for a system of hard spheres, by Alder and Wainwright [54, 55]. In this case, the particles move at a constant velocity between perfectly elastic collisions, and it is possible to solve the dynamic problem without making any approximation. Several years later, a successful attempt was made to solve the equations of motion for a realistic system, a set of Lennard-Jones particles [56]. Here, an approximate, step-by-step procedure is needed, since the forces change continuously as the particles move.

The classical Newtonian equations of motion can be written as

$$m_i \ddot{\mathbf{r}}_i = \mathbf{f}_i \qquad \mathbf{f}_i = -\frac{\partial}{\partial \mathbf{r}_i} U, \tag{1.13}$$

where the particles are consdered as point masses m_i that interact via the interatomic potential U. Thus we can calculate the forces $\mathbf{f}_i$ and the accelerations for all the particles in the system for each moment.

A standard method for solution of ordinary differential equations such as 1.13 is the finite difference approach. The general idea is the following: given the molecular positions, velocities, and other dynamics information at time t, we attempt to obtain the positions, velocities etc. at a later time $t + \delta t$, to a sufficient degree of accuracy. The equations are solved on a step-by-step basis. The time interval δt should be significantly smaller than the typical time taken for a molecule to travel its own length [52]. Typical values of MD timestep are of the order of $10^{-12} - 10^{-15}$ seconds.

1.2.2.2 Verlet algorithm

In this work we used DL_POLY software [57] to carry out MD simulations. It uses the algorithms based on the Verlet scheme [58] to numerically integrate the equations of motion. This algorithm generates trajectories in the micro canonical (NVE) ensemble in which the total energy (kinetic plus potential energy) is conserved. We used the leapfrog (LF) algorithm version.

The LF algorithm requires the knowledge of position (r) and force (f) at a time t while the velocities (v) are half a timestep behind. The first step is to calculate the velocities at $t + (1/2)\delta t$ by integrating of the force:

$$v(t + \frac{1}{2}\delta t) \longleftarrow v(t - \frac{1}{2}\delta t) + \delta t \frac{f(t)}{m} \tag{1.14}$$

where m is the mass of a site.

The positions are then calculated using the new velocities:

$$r(t+\delta t) \longleftarrow r(t) + \delta t v(t+\frac{1}{2}\delta t) \tag{1.15}$$

1.2.2.3 Core-shell model treatment

The IAPs derived in this work include the core-shell model [43] for both Te and O atoms. This model requires a special treatment in MD simulations, as the shells are supposed to be massless point charges that makes solving of the equations of motion impossible. Two methods of incorporating atom polarisability into MD simulation are included in DL_POLY Classic software [57]. The first one is the devised by Fincham *et al.* [59] and known as the adiabatic shell model. In this method a fraction of the atomic mass is assigned to the shell in order to permit a dynamical description. The fraction of the mass is chosen in a manner to ensure that the natural frequency of vibration ν of the harmonic spring (i.e.

$$\nu = \frac{1}{2\pi}\Big[\frac{k_2^{cs}}{x(1-x)m}\Big]^{1/2}, \tag{1.16}$$

where m and k_2^{cs} are the atomic mass and the harmonic spring constant (see 1.2.1.2)), is well above the frequency of vibration of the whole atom in the system. From the dynamical point of view, the core-shell unit resembles a diatomic molecule with harmonic bond. However, the high vibration frequency of the bond prevents effective exchange of the kinetic energy between the core-shell unit and the remaining system [57]. Such implementation of a core-shell model doubles the number of the particles in the system and correspondingly increases the computation time.

The second method is the relaxed shell model described by Lindan and Gillan in [60]. It is based on the same electrostatic principles as described in 1.2.1.2 and the shell is assigned a zero mass. This means that the shell cannot be driven dynamically and instead, firstly, we relax it to a condition of zero (or at least negligible) force at the start of the integration of the atomic motion and then we integrate the motion of the finite mass core by conventional molecular dynamics. Since each timestep of the algorithm entails a minimisation operation, the cost per timestep becomes considerably more than for rigid-ion MD simulation.

1.2.2.4 Thermostats

The discussion above concerned the 'typical' MD simulations with constant particles number, system volume and total energy, *i.e.* the NVE or 'microcanonical' ensemble. In many practical cases we might wish to keep other quantities constant, for example, temperature or/and pressure. In those cases the MD system must be coupled to a thermostat or/and barostat to ensure that the average system temperature or/and pressure is/are maintained close to the requested ones.

There are several ways to perform the MD simulations in other than microcanonical ensemble (Langevin [61], Andersen [62], Evans (Gaussian constraints)[63], Berendsen [64], Nosé-Hoover [65] thermostats). The most used are the Berendsen and Nosé-Hoover algorithms. We will briefly discuss here Berendsen thermostat and barostat used in this work. More detailed information on realisation of different algorithms can be found in the literature (for example, in [52, 57, 66]).

In Berendsen thermostat the system is coupled to an external heat bath with fixed temperature T_0. The velocities are scaled at each step, such that the rate of temperature change is proportional to the difference in temperature:

$$\frac{dT(t)}{dt} = \frac{1}{\tau}(T_0 - T(t)) \tag{1.17}$$

where τ is the coupling parameter, which determines how tightly the bath and the system are coupled together. The change in temperature between successive time steps is:

$$\Delta T = \frac{\delta t}{\tau}(T_0 - T(t)). \tag{1.18}$$

Thus, the scaling factor for the velocities is

$$\lambda = \sqrt{T_0/T(t)} = 1 + \frac{\delta t}{\tau}\left\{\frac{T_0}{T(t - \frac{\delta t}{2})} - 1\right\}. \tag{1.19}$$

Similar to the temperature coupling, in Berendsen barostat an extra term is added to the equations of motion that effects the pressure change

$$\left(\frac{dp}{dt}\right) = \frac{p - p_0}{\tau_p} \tag{1.20}$$

where τ_p is the time constant of coupling. A simple proportional coordinate scaling accompanies volume scaling and minimises local disturbances. An extra term is added to the equations of motion:

$$\dot{\mathbf{r}} = \mathbf{v} + \alpha\mathbf{r}, \tag{1.21}$$

while the volume changes accordingly:

$$\dot{V} = 3\alpha V. \tag{1.22}$$

The pressure change is related to isothermal compressibility β

$$\frac{dp}{dt} = -\frac{1}{\beta V}\frac{dV}{dt} = -\frac{3\alpha}{\beta}. \tag{1.23}$$

With Eq. 1.20 α evaluates to

$$\alpha = -\frac{\beta(p_0 - p)}{3\tau_p}. \tag{1.24}$$

Thus the modified equation of motion is

$$\dot{\mathbf{r}} = \mathbf{v} - \frac{\beta(p_0 - p)}{3\tau_p}\mathbf{r} \tag{1.25}$$

and represents a proportional scaling of coordinates.

1.2.2.5 Periodic boundary conditions (PBC)

Computer simulations are usually performed on a small number of molecules, $10 \leq N \leq 10\ 000$. Although, nowadays the computational facilities increase from year to year owing to new powerful supercomputers and new fast algorithms and the size of simulated systems can achieve 10 million-atom size [67], the majority of the studied systems remains relatively small. Small system size leads to significant influence of the surface effects. For 1000 atoms arranged in a 10×10×10 cube, no less than 488 atoms appear on the cube faces, so that atoms on the surface will experience quite different forces from atoms in the bulk. The problem of surface effects can be overcome by implementing periodic boundary conditions [68]. The cubic (or rectangular) box is replicated through space to form an infinite lattice. In the course of the simulation, as an atom moves in the original box, its periodic image in each of the neighbouring boxes moves in exactly the same way. Thus, as an atom leaves the central box, one of its images will enter through the opposite face [52].

In this work the size of the box was chosen in order to model the glass up to "medium" limit distances where the atoms positions are no more correlated. In our case, this value was set to 12 Å. This means that simulation box should have the $L/2 > 12$ Å (where L – the side of the simulation box), which results in system with > 850 particles (1700 working with core-shell model) considering the atomic density of about 0.06 atoms/Å^3.

1.3 Experimental Approach

1.3.1 Conventional X-ray powder diffraction characterisation

The phase identification for the synthesised TeO_2 polymorphs was made with the help of X-ray powder diffraction (XRD). This is a well-known technique and the general presentation of the method and its theoretical background could be found elsewhere (for example, in the book of B.E. Warren, *X-ray diffraction* [69]). We just recall here that the principle of powder diffraction consists in irradiating a polycrystalline sample with a (quasi)monochromatic X-ray beam and measuring the scattered intensities on a large (2θ) angular domain. The diffraction peaks and the background constitute the diffraction diagram, the former serve as the characteristics of the compound structure (metrics and symmetry of crystalline lattice, nature and positions of atoms in the cell).

In this work we used a Brucker D8 Advance diffractometer with Bragg-Brentano $\theta-2\theta$ geometry equipped with X-ray tube with copper anode and a Guinier/Johansson type germanium monochromator cut along the planes (111). This monochromator allows one to work with the monochromatic K_{α_1} (1.5406 Å) copper radiation. The set-up is also equipped with a furnace that allows performing measurements at various temperatures.

The resolution and refinement of a structure were performed using the Rietveld [70] method. The position, height and width of the reflections in the diffraction pattern are used to determine the crystalline lattice metric and atomic positions. This method is well-known and its detailed description could be found in *The Rietveld Method* by R. A. Young [71]. The refinement reported in this work was made with Jana2006 [72] and Fullprof [73] softwares. The adjusted parameters were: the cell parameters, atomic positions, atomic displacement parameters, background and peak profile parameters.

1.3.2 X-ray total scattering

The X-ray total scattering technique is routinely used for 7 years at the SPCTS laboratory. The theoretical background and set-up have already been discussed in previous SPCTS PhD thesis [74, 75, 76]. We recall below the main points.

Conventional X-ray diffraction methods (or neutron diffraction) focus mainly on precise measurement of the positions and the intensities of Bragg peaks and, hence, on the average structure only. (The peak position depends on the crystalline lattice metric, whereas the intensities provide the information about the averaged atoms positions in the cell.) No attention is paid on the background. Nevertheless, the background contains the diffuse scattering signal coming from the sample. This signal contains information about the deviation of the real structure with respect to the average structure and provides some interesting structural information, namely about the nature of the structural disorder

[77, 69, 78]. The total X-ray scattering principle consists in measuring whole scattered signal, *i.e.* the Bragg peaks and the diffuse scattering. These measurements allow us to obtain the PDF of the studied material.

For the long time this technique was the way to obtain structural information in glasses and liquids. In the 1980s, it was applied to the crystalline solids [77]. This evolution was favoured by availability of the sources of the intense synchrotron radiation with the short wavelength which allowed us to obtain the good quality PDFs, and by improving of the structure simulation methods, which permit to analyse these functions. The complete review of the total scattering is given in the book of Egami and Billinge, *Underneath the Bragg peaks: structural analysis of complex materials* [77]. We will precise here the theoretical background of X-ray total scattering emphasising the quantities that we can obtain with this technique. Then we will present the manner, in which we obtained the PDFs at SPCTS for the samples synthesised in Chapter 2.

1.3.2.1 Theoretical background

1.3.2.1.1 Bragg scattering and diffuse scattering In the total scattering experiment we measure the elastic scattering differential cross-section $\frac{d\sigma}{d\Omega}$ of the sample in the directions of the scattering vector $\vec{Q}$. This cross-section represents the number of elastically scattered photons per time per solid angle $d\Omega$. The vector $\vec{Q}$ is defined as $\vec{Q} = \vec{k}_{final} - \vec{k}_{initial}$, where $\vec{k}_{initial}$ and $\vec{k}_{final}$ represent the wave vectors of incident and scattered waves (Fig. 1.13).

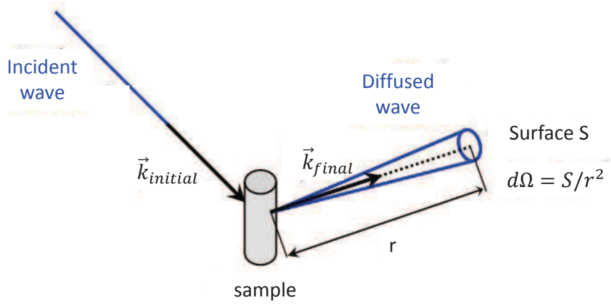

Figure 1.13: Quantities used in description of X-ray diffusion phenomenon.

The norm of this vector is equal to $\frac{4\pi sin\theta}{\lambda}$, where λ is the wavelength of the incident radiation and θ is the half of the scattering angle 2θ. The expression 1.26 gives the amplitude of the wave scattered in the direction $\vec{Q}$, where N represents the number of atoms in the sample, f_j is the scattering factor of an atom j and $\vec{r_j}$ is the position vector of this atom.

$$A(\vec{Q}) = \sum_{j=1}^{N} f_j e^{i\vec{Q}\vec{r}_j} \tag{1.26}$$

The elastic scattering differential cross-section measured in the direction $\vec{Q}$ is given by the square of the scattered amplitude [79, 80]:

$$\frac{d\sigma}{d\Omega} = I(\vec{Q}) = \langle A(\vec{Q})A^*(\vec{Q})\rangle = \sum_{j=1}^{N}\sum_{k=1}^{N} f_j f_k^* \langle e^{i\vec{Q}(\vec{r}_j-\vec{r}_k)}\rangle \tag{1.27}$$

As it can be seen, the intensity provides information on the interatomic vectors $\vec{r}_j - \vec{r}_k$.

As the averaged crystalline structure could be defined and as we consider only displacement disorder, we can decompose the vector position of an atom j as follows:

$$\vec{r_j} = \vec{R}_j + \vec{\delta}_j, \tag{1.28}$$

where $\vec{R}$ represents the average position of atom j in the structure (the ideal position) and $\vec{\delta}_j$ is the displacement with respect to this average position. Substituting this to expression 1.27 gives:

$$I(\vec{Q}) = \sum_j\sum_k f_j f_k^* e^{i\vec{Q}(\vec{R}_j-\vec{R}_k)}\langle e^{i\vec{Q}(\vec{\delta}_j-\vec{\delta}_k)}\rangle \tag{1.29}$$

Given u_j the projection of the vector $\vec{\delta}_j$ on the scattering vector, this expression becomes:

$$I(\vec{Q}) = \sum_j\sum_k f_j f_k^* e^{i\vec{Q}(\vec{R}_j-\vec{R}_k)}\langle e^{iQ(u_j-u_k)}\rangle. \tag{1.30}$$

It could be written in the form:

$$I(\vec{Q}) = I_B(\vec{Q}) + I_D(\vec{Q}), \tag{1.31}$$

where $I_B(\vec{Q})$ and $I_D(\vec{Q})$ represent Bragg scattering and diffuse scattering respectively and given as:

$$I_B(\vec{Q}) = \sum_j\sum_k f_j f_k^* e^{i\vec{Q}(\vec{R}_j-\vec{R}_k)}\langle e^{iQu_j}\rangle\langle e^{-iQu_k}\rangle \tag{1.32}$$

$$I_D(\vec{Q}) = \sum_j\sum_k f_j f_k^* e^{i\vec{Q}(\vec{R}_j-\vec{R}_k)}\Big(\langle e^{iQ(u_j-u_k)}\rangle - \langle e^{iQu_j}\rangle\langle e^{-iQu_k}\rangle\Big). \tag{1.33}$$

The second term in the equation 1.31 gives the continuous distribution of the intensity scattered by the reciprocal lattice; it corresponds to diffuse scattering. It can be divided into two terms ($j = k$ and $j \neq k$):

$$\begin{aligned} I_D(\vec{Q}) &= \sum_j |f_j|^2 (1 - \langle e^{iQu_j}\rangle \langle e^{-iQu_k}\rangle) \\ &+ \sum_j \sum_{k \neq j} f_j f_k^* e^{i\vec{Q}(\vec{R}_j - \vec{R}_k)} \big(\langle e^{iQ(u_j - u_k)}\rangle - \langle e^{iQu_j}\rangle \langle e^{-iQu_k}\rangle \big) \end{aligned} \tag{1.34}$$

The first term of this new equation yields to the increase of diffuse scattering with Q. It depends on the atomic displacement factor that means that the intensity lost in the Bragg peaks is found in this term. It converges to $\sum_j |f_j|^2$ at large Q values (while the Bragg peaks disappear). The second term, that contains information about the correlations of displacements (through the term $e^{iQ(u_j - u_k)}$), yields to the modulations of the diffuse scattering. It turns into zero when the displacements are not correlated (since $\langle e^{iQ(u_j - u_k)}\rangle = \langle e^{iQu_j}\rangle \langle e^{-iQu_k}\rangle$).

It is easily clear now, why it is important to measure the ensemble of scattered signal and not only Bragg scattering, loosing a part of the information about structural disorder present in the sample.

1.3.2.1.2 Pair distribution functions In the case of homogeneous samples, as it is the case on this work, the scattering signal depends only on the modulus of $\vec{Q}$ but not on its direction.

Thus, the relation 1.29 for the intensity could be given in the form (Debye formulae):

$$I(Q) = \sum_j \sum_k f_j f_k^* \frac{sin(Qr_{jk})}{Qr_{jk}} \tag{1.35}$$

which, in turn, can be expressed with respect to the pair distribution function $G(r)$ of the material with the use of sine Fourier transform:

$$Q(S(Q) - 1) = \int_0^\infty 4\pi r \rho_0 (G(r) - 1) sin(Qr) dr \tag{1.36}$$

where ρ_0 represents the atomic density (in atom/Å^3) and $S(Q)$ the structure factor or structure function defined as:

$$S(Q) - 1 = \frac{I(Q) - \sum_j |f_j|^2}{|\sum_j f_j^2|} = \frac{I(Q)/N - \langle |f|^2 \rangle}{|\langle f \rangle|^2} \tag{1.37}$$

We shall note that $S(Q)$ should not be confused with the crystallographic structure factor $F_{hkl}(Q)$, which represents the amplitude scattered by the crystalline unit cell.

The pair distribution function is obtained experimentally by truncated sine Fourier transform of the structure factor (measured by total scattering):

$$4\pi r \rho_0 (G(r) - 1) = \frac{2}{\pi} \int_0^{Q_{max}} Q(S(Q) - 1) sin(Qr) dQ, \tag{1.38}$$

where Q_{max} is maximum experimentally reachable magnitude value of the scattering value.

The pair distribution function $G(r)$ represents the probability to find in the structure a pair of atoms separated by a distance r. It is one-dimensional function, which presents the peaks at the values of r corresponding to interatomic distances. Fig. 1.14 illustrates the construction of such a function, each atom is taken as an origin and the average is over the ensemble of the atoms in the sample.

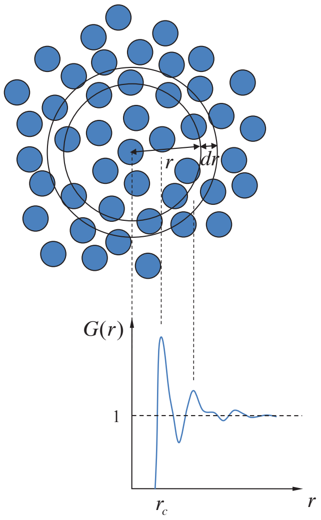

Figure 1.14: Scheme representing the construction of the pair distribution function G(r).

Let us note, that for the distances smaller than r_c the function is equal to zero. This distance characterises the shortest interatomic distances present in the structure. We can also point out that $G(r)$ converges to 1 (oscillating around this value) for great r values. Thus, each peak of the PDF is directly associated with pairs of atoms present in the material, and peak area is proportional to the probability of the presence of the pair. The PDF is very intuitive and permits simple description of the short- and medium-range order in studied material.

In this work we will also use the reduced form of the PDF denoted $g(r)$ and defined as:

$$g(r) = 4\pi r\rho_0(G(r) - 1). \tag{1.39}$$

This function is zero at $r = 0$, then it follows negative slope until $r = r_c$, and oscillates around 0 when $r \to \infty$. The main advantage of this function is a nice development of the correlation peaks at intermediate distances.

1.3.2.1.3 Multi-component systems In the case when the system under study (like in this work) is composed of more than one kind of atom, the structure factor and the pair distribution function appear as the function of partial quantities $S_{\alpha\beta}(Q)$ and $G_{\alpha\beta}(r)$, which represent the partial structure factor and partial PDF for the pairs of atoms of type α and β respectively. The relation between the structure factor and the partial functions is as follows:

$$S(Q) = \sum_{\alpha=1}^{n}\sum_{\beta=1}^{n}\gamma_{\alpha\beta}S_{\alpha\beta}(Q) \tag{1.40}$$

with $\gamma_{\alpha\beta}$ Faber-Ziman coefficients, defined as:

$$\gamma_{\alpha\beta}(Q) = \frac{c_\alpha c_\beta f_\alpha f_\beta^*}{|\langle f\rangle|^2} \tag{1.41}$$

where c_α and c_β represent the atomic concentrations of species α and β and f_α and f_β^* their corresponding atomic scattering factors.

In the same manner, we can express the total pair distribution function as a function of the partial pair distribution functions:

$$g(r) \approx \sum_{\alpha=1}^{n}\sum_{\beta=1}^{n}\gamma_{\alpha\beta}\big[g_{\alpha\beta}(r) - 1\big]. \tag{1.42}$$

Meanwhile, the last equation is only an approximation (Warren, Krutter and Morningstar (WKM) approximation), which considers the Faber-Ziman factors as constant. The exact expression was recently obtained in [81]. The functions $g(r)$ and $g_{\alpha\beta}(r)$ are constructed in the similar way, in particular they tend to 0 at large distances. We can also note that the partial functions depend only on the atomic structure of the material, whereas the function $g(r)$ besides this depends on experimental technique because of the presence of $\gamma_{\alpha\beta}$.

1.3.2.2 Presentation of the experimental set-up, acquisition and data treatment

The diffractometer used in this work was developed 7 years ago in the SPCTS laboratory in collaboration with Pierre Lecante from CEMES in Toulouse. The detailed description is given in the thesis of Richard Mayet [75]. It consists of the following elements (Fig. 1.15): a molybdenum sealed X-ray tube (1); a graphite monochromator (2) cut along the planes (002) that permits the selection of the molybdenum doublet ($K_{\alpha_1}, K_{\alpha_2}$) wavelength ($\lambda_{K_{\alpha_1}} = 0.7093$); a goniometric head (3), which supports the capillary containing the powder and which should be adjusted in such a way that the axis of the capillary coincide with the rotational axis of the goniometer; two collimators comprised of the splits of 1 and 2 mm (the front collimator (4) permits to define a quasi-parallel incident beam, while the back collimator (5) defines the direction of 2θ); a scintillation detector (6) permits to count the photons scattered by the sample.

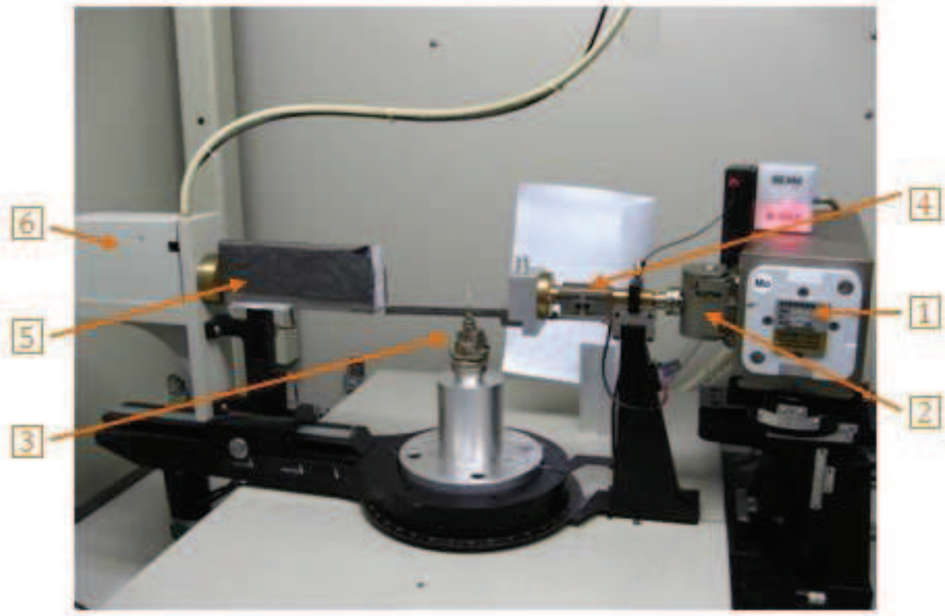

Figure 1.15: Diffractometer set up used in X-ray total scattering.

To limit the absorption of the incident X-ray beam by the sample and, hence, to minimise the absorption corrections, it is necessary to determine the linear attenuation coefficients μ for each component and to foresee an adequate capillary diameter. To this end, we calculate the mass attenuation coefficient μ/ρ for each studied compound following the equation 1.43. X_i represents the mass fraction and $(\mu/\rho)_i$ the mass attenuation coefficient of each element i. The latter could be easily found in the international tables for crystallography. The density ρ is calculated considering that the compactness of the powder inside the capillary is about 40 %.

$$\left(\frac{\mu}{\rho}\right)_{total} = \sum_i X_i \left(\frac{\mu}{\rho}\right)_i \tag{1.43}$$

Thus, one needs to define the radius of the capillary, r, so that $\mu r \approx 1$. However, generally it is difficult to get the capillary of exactly obtained value, so we chose a greater diameter than calculated one in oder to avoid the difficulties when filling the capillary, which can lead to decrease of the local compactness. In this work we used the capillaries with the diameter 0.3 mm for $\delta-$ and $\gamma-\mathrm{TeO}_2$ samples.

Filled capillary is put on the goniometric head and adjusted in such a way to remain fixed in the centre of the incident beam during its rotation. For this purpose we adjust the angles and the translations of the goniometric head with the help of a microscope. The acquisition of the diagrams is carried out then directly to a computer connected with the diffractometer using the XTSScan software developed in the laboratory [82]. The scattered by the sample intensity is collected by the detector mounted on the 2θ holder. The acquisition parameters are as follows:

- Q_{min} = 0 Å^{-1} (or $2\theta = 0°$)
- Q_{max} = 17 Å^{-1} (or $2\theta \approx 147.29°$)
- step ΔQ = 0.02 AA^{-1}
- pause time t = 240 s

For each sample we carried out several measurements to improve the count statistics, in particular for the large angles. To obtain the structure factor, it is necessary to perform a certain number of corrections for the raw data, in particular to eliminate the signals, which were not scattered by the sample and to keep only the elastic scattering, $I(Q)$. The different corrections are estimated either with calculations or with additional measurements. We will briefly recall the correction type to be carried out here. The scattered intensity measured experimentally from the sample, I_{sample}, is related to $I(Q)$ by:

$$I(Q) = \frac{1}{P(Q)}\frac{1}{A(Q)}\left[I_{sample}(Q) - \alpha A'(Q) I_{Fluo} - Y(Q) A''(Q) I_{Comp}(Q) - I_{Mul}(Q)\right], \quad (1.44)$$

where

- $P(Q)$ is the polarisation factor,
- $A(Q)$, the absorption factor of the sample for the incident radiation of the wavelength λ,
- I_{Fluo}, the fluorescent radiation intensity,
- $A'(Q)$, the absorption factor of the sample for the incident radiation of the wavelength $\lambda'(\lambda' > \lambda)$,
- α, the fraction of the fluorescent radiation intensity effectively measured by the detector,
- $I_{Comp}(Q)$, the Compton scattering intensity,
- $A'(Q)$, the absorption factor of the sample for the Compton scattering of the wavelength $\lambda''(\lambda'' > \lambda)$,

- $Y(Q)$, the fraction of the Compton scattering intensity effectively measured by the detector,
- $I_{Mul}(Q)$, the intensity resulting from the multiple scattering in the sample.

The total intensity scattered by the sample $I_{sample}(Q)$ is obtained from the experimentally measured intensity I_{exp} with the following expression:

$$I_{sample}(Q) = I_{exp} - \beta(Q)I_{EV}(Q) - A_{C,CE}(Q)I_C(Q), \tag{1.45}$$

where

- $I_{EV}(Q$ is the scattering from empty environment (no sample),
- $\beta(Q)$, scattering measured in the presence of the sample,
- $I_C(Q)$, the scattering from the capillary only,
- $A_{C,CE}(Q)$, the absorption of scattering by the capillary with the sample.

The procedures for corrections, normalisation and obtaining the pair distribution function concerning the X-ray total scattering are performed using a home-made program [83] and are not given here.

1.3.3 Raman scattering

Raman spectroscopy is a spectroscopic technique used to observe vibrational, rotational, and other low-frequency modes in a system. The principle of the Raman spectroscopy is based on the Raman scattering phenomenon discovered by C. V. Raman and K. S. Krishnan in liquids [84] and by G. Landsberg and L. I. Mandelstam in crystals [85] in 1928. The effect had been predicted theoretically by Adolf Smekal in 1923 [86]. When the laser beam interacts with a material, it will scatter the part of the incident light. Most photons are elastically scattered (Rayleigh scattering), such that the scattered photons have the same energy (frequency and wavelength) as the incident photons. However, a small fraction of the scattered photons are scattered by an excitation, with the scattered photons having a frequency different from, and usually lower than, that of the incident photons. This excitations (also called phonons) are the vibrational modes of the system. Hence, with Raman scattering we can determine the vibrational modes of a material by measuring the difference in energy between the excitation and scattered photons. But not all the vibration modes are Raman-active. They will be Raman-active only if they obey the selection rules [87].

In our study we used the Jobin-Yvon 6400 spectrometer facility supplied with a CCD camera and an ionised argon excitation source of 514.532 nm wavelength. As our samples are metastable, in order to avoid their decomposition under laser exposure, we set the following parameters: a weak laser power of 300 mW, a yellow filter D1 and a short acquisition time of 10 s. The Raman spectra were registered between 10 and 1000 cm^{-1} through a microscope (x50). The diameter of a laser spot is about 1 μm. The evolution with temperature of the samples was studied with the a furnace LINKAM THS600.

1.3.4 Differential scanning calorimetry

The differential calorimetry analysis measures the difference in the heat flux between the sample and the reference (that could be air, for example) during the temperature cycle. It permits to determine the glass transition temperature (T_g), melting temperature (T_m), crystallisation temperature (T_c) and the reaction enthalpies.

The powdered samples ($\approx$ 15–20 mg) were introduced into covered aluminium crucibles and the DSC curves were recorded between 40 and 600 °C using a heating rate of 10 °C/min. In order to avoid the reaction of the studied material with the furnace atmosphere, the analysis were held under inert gas (nitrogen with the flux of 50 ml/min). We considered the glass transition temperature as the inflection point of the steep change of the calorimetric signal associated with this transition. The crystallisation temperature was taken as the intersection of the slope of the exothermic peak with the baseline.

Chapter 2

Synthesis of $\delta-$ and $\gamma-TeO_2$ polymorphs

The metastable $\delta-$ and $\gamma-TeO_2$ polymorphs are very interesting from a structural point of view. However, they are both very difficult to synthesise as pure as possible, *i.e.* without any secondary phases, as was discussed in Chapter 1. In this chapter, we aim to present our work about the optimisation of the synthesis parameters for such samples by crystallising the modified TeO_2 glassy systems. For each chosen system we studied the phase evolution using temperature *in situ* X-ray diffraction and Raman spectroscopy and then we discuss the conditions of preparation of pure $\delta-TeO_2$ and $\gamma-TeO_2$ crystalline polymorphs and their Raman spectroscopic and thermal analysis. The $\delta-TeO_2$ structure will be further studied in Chapter 4.

2.1 Previous studies on $\delta-$ and $\gamma-TeO_2$ synthesis

The choice of the compositions was based on previous studies of our group in the SPCTS laboratory. It was shown [9, 14, 10, 11, 12, 88] that $\delta-$ and $\gamma-TeO_2$ polymorphs can be obtained from the modified TeO_2 glassy systems like TeO_2–WO_3, TeO_2–Nb_2O_5 and TeO_2–PbO. Namely, in TeO_2–WO_3 system $\gamma-TeO_2$ crystallises from the glasses with 5–20 molar % of WO_3 in 325–475 ℃ range, according to the diagram of evolution with composition of T_g and T_c from [9] (Fig. 2.1). $\delta-TeO_2$ crystallises in more narrow range: 5–15 molar % of WO_3 and 325–425 ℃ range. In all cases $\gamma-TeO_2$ and $\delta-TeO_2$ polymorphs appear with a small quantity of $\alpha-TeO_2$ polymorph, which increases when T_c augments.

These polymorphs also appear within the TeO_2–Nb_2O_5 system [14]. Blanchandin *et al.* studied the equilibrium and non-equilibrium phase diagrams and showed that $\gamma-TeO_2$ forms within the 2.5–25 molar % range and in 390–540 ℃ temperature range (Fig. 2.2). Similarly to the WO_3-modified system, the $\delta-TeO_2$ forms in a more narrow region: 2.5–12.5 molar % and 390–430 ℃.

For the TeO_2–PbO system, $\gamma-TeO_2$ and $\delta-TeO_2$ crystallise in the ranges close to those

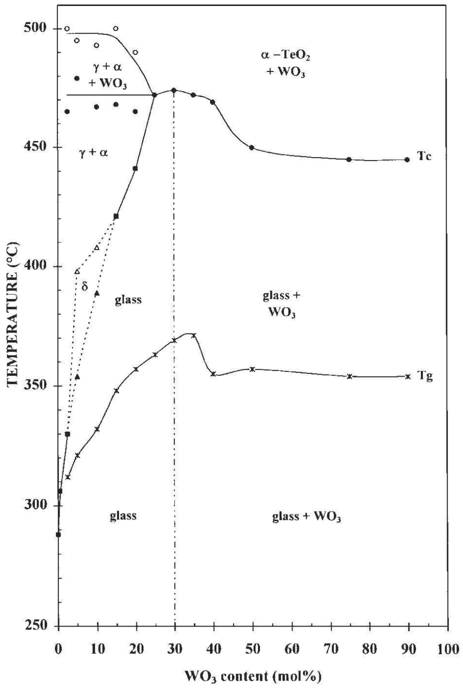

Figure 2.1: Evolution with composition of the glass transition temperature T_g ($*$), of the various crystallisation temperatures T_c (□: $\gamma-$ and $\alpha-\mathrm{TeO}_2$; ▴: $\delta-\mathrm{TeO}_2$, •: WO_3) and of mono tropic transition temperatures (△: $\delta \rightarrow \alpha$, ∘: $\gamma \rightarrow \alpha$) of the TeO_2–WO_3 glasses.

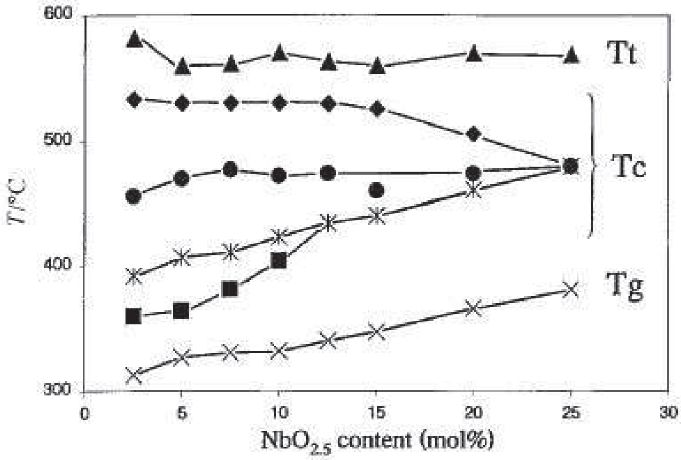

Figure 2.2: Evolution with composition of the glass transition temperature T_g (×), of the various crystallisation temperatures T_c (■: $\delta-\mathrm{TeO}_2$; $*$: $\gamma-\mathrm{TeO}_2$; •: $\alpha-\mathrm{TeO}_2$, ◆: $\mathrm{Nb}_2\mathrm{Te}_4\mathrm{O}_{13}$) and of polymorphic transformation T_t (▲: $\gamma \rightarrow \alpha$) temperatures of the TeO_2–$\mathrm{NbO}_{2.5}$ glasses.

of the TeO_2–Nb_2O_5 system. Fig. 2.3 reports the evolution of T_g and T_c of the TeO_2–PbO glasses with composition [88].

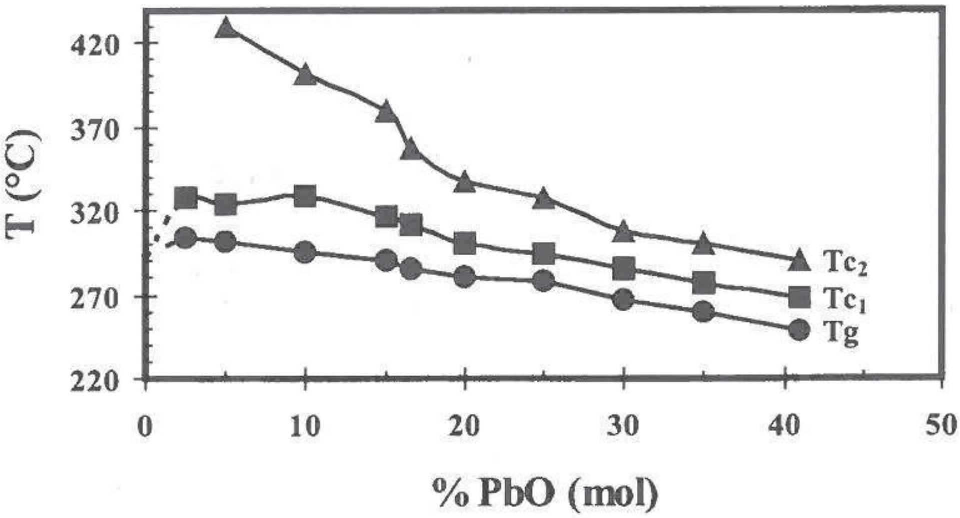

Figure 2.3: Evolution with composition of the glass transition temperature T_g (●), of the various crystallisation temperatures T_c (■: $\delta-TeO_2$ and $\gamma-TeO_2$; ▲: $\alpha-TeO_2$ or mixture of $PbTe_5O_{11}$ and $Pb_2Te_3O_8$ according to the initial composition of the sample) of the TeO_2–PbO glasses.

We aimed to define the optimal conditions for crystallisation of $\gamma-TeO_2$ and $\delta-TeO_2$ polymorphs with the minimum content of $\alpha-TeO_2$ polymorph. To this end we intended to minimise the modifiers percentage (but at the same time to add enough modifier to improve the glass stability) for the four following systems: 92.5%TeO_2 + 7.5%WO_3 ($\delta-TeO_2$ exists in a too narrow temperature range for the system with 5%WO_3), 90%TeO_2 + 10%WO_3, 95%TeO_2 + 5%$NbO_{2.5}$, and 95%TeO_2 + 5%PbO.

2.2 Preliminary temperature *in situ* X-Ray diffraction and Raman spectroscopy studies of the crystallisation of $\delta-$ and $\gamma-$TeO$_2$ from glasses.

We used the commercial materials for all modifiers : WO_3 (Alfa Aesar 99.8%), Nb_2O_5 (Sigma-Aldrich 99.9%) and PbO (Aldrich 99.9%). TeO_2 was prepared from thermal decomposition of orthotelluric acid H_6TeO_6 (Aldrich 99.9%) at 550 ℃ for 12h following the chemical reaction:

$$H_6TeO_6 \longrightarrow TeO_2 + 3H_2O + 1/2O_2.$$

The as-obtained tellurium dioxide corresponds to $\alpha-$TeO$_2$ polymorph.

The powders were milled during 20–30 minutes in an agate mortar in proportions that correspond to the chosen compositions. Then, the samples were melted in platinum crucibles during half an hour at 800 ℃ and quenched using the method proposed by Kim *et al.* [89]. In this method, the bottom of platinum crucible was quickly dipped in a freezing mixture (at temperature of about −10°C) which consists of ice, ethanol and NaCl. Each obtained glassy sample was checked by XRD and Raman spectroscopy for the absence of the crystallised phases.

Further we performed *in situ* X-Ray diffraction and Raman spectroscopy measurements in order to precisely define the crystallisation temperatures for TeO_2 polymorphs. In both experiments the furnace was heated at 10 ℃/min to the required temperature. We waited 5 minutes before each acquisition in order to stabilise the temperature within the whole sample. The acquisition time of one Raman spectrum was set to 60 seconds in order to avoid a long term laser exposure on the sample. The X-ray diffraction acquisition required about 55 minutes for the chosen 2θ range.

For Raman spectroscopy measurements the acquisitions were made in three different sample points in order to ensure of the sample homogeneity. After the measurements the data were normalised, averaged for each temperature and corrected for Bose-Einstein factor.

2.2.1 The 92.5%TeO_2 + 7.5%WO_3 system

The *in situ* X-Ray diffraction with temperature shows, that three TeO_2 polymorphs crystallise from the TeO_2-glass with 7.5 mol % of WO_3. Firstly, we observe (Fig. 2.4) that $\alpha-TeO_2$ begin to crystallise already at 320 ℃ when the most part of the sample is still in a glassy state. Then $\delta-TeO_2$ polymorph appears in a very narrow temperature region of 340-350 ℃. It is well crystallised and has narrow and intense diffraction peaks. The enlarged part of the XRD pattern in the insert demonstrates the weak peaks of secondary $\alpha-TeO_2$ phase. The intensity of these peaks remains constant until approximately 410 ℃.

As the sample is heated up to 360 ℃, we observe how $\delta-TeO_2$ polymorph transforms to $\gamma-TeO_2$ polymorph. These phases co-exist at 360-370 ℃ and starting from 380 ℃ we only have a well crystallised $\gamma-TeO_2$ polymorph (accompanied by small quantity of α phase). The quantity of $\alpha-TeO_2$ polymorph in the sample starts to increase from 420 ℃ and at 450 ℃ $\gamma-TeO_2$ polymorph has completely disappeared.

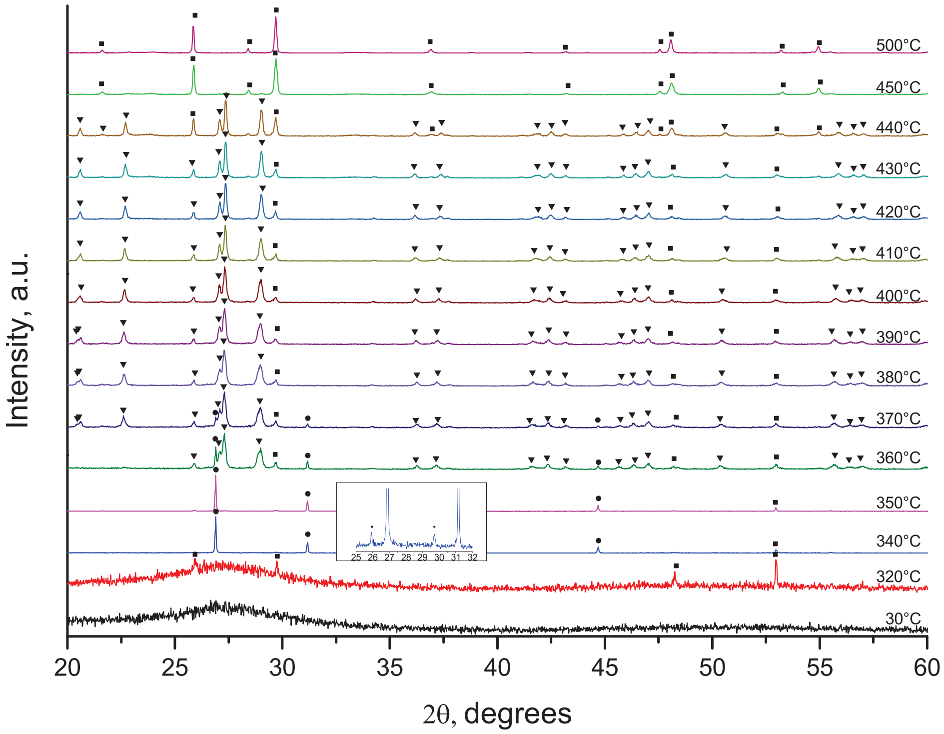

Figure 2.4: XRD powder patterns at various temperatures for a TeO_2 glassy sample containing $7.5WO_3$ mol % (●: $\delta-TeO_2$, ▼: $\gamma-TeO_2$, ■: $\alpha-TeO_2$).

The crystallisation of 92.5%TeO_2 + 7.5%WO_3 glassy sample evolves in the same manner according to the *in situ* Raman spectroscopy with temperature (see Fig. 2.5), but with a certain shift in crystallisation temperature values. This difference appears for all studied samples and is due to different acquisition conditions (60 seconds acquisition for Raman spectroscopy and 55 minutes for XRD) and, hence, to kinetic effect of crystallisation.

According to the Raman spectroscopy analysis, the 92.5%$\mathrm{TeO_2}$ + 7.5%$\mathrm{WO_3}$ sample stays in glassy state under 370℃ and crystallises directly to $\gamma-\mathrm{TeO_2}$ polymorph (with secondary $\alpha-\mathrm{TeO_2}$ phase) at 380℃. We cannot observe $\delta-\mathrm{TeO_2}$ crystallisation, as its Raman spectrum is hardly distinguishable from the one of a glassy sample (see the Raman spectrum of $\delta-\mathrm{TeO_2}$ in Fig. 2.16). The sample fully transforms to $\alpha-\mathrm{TeO_2}$ at 500℃.

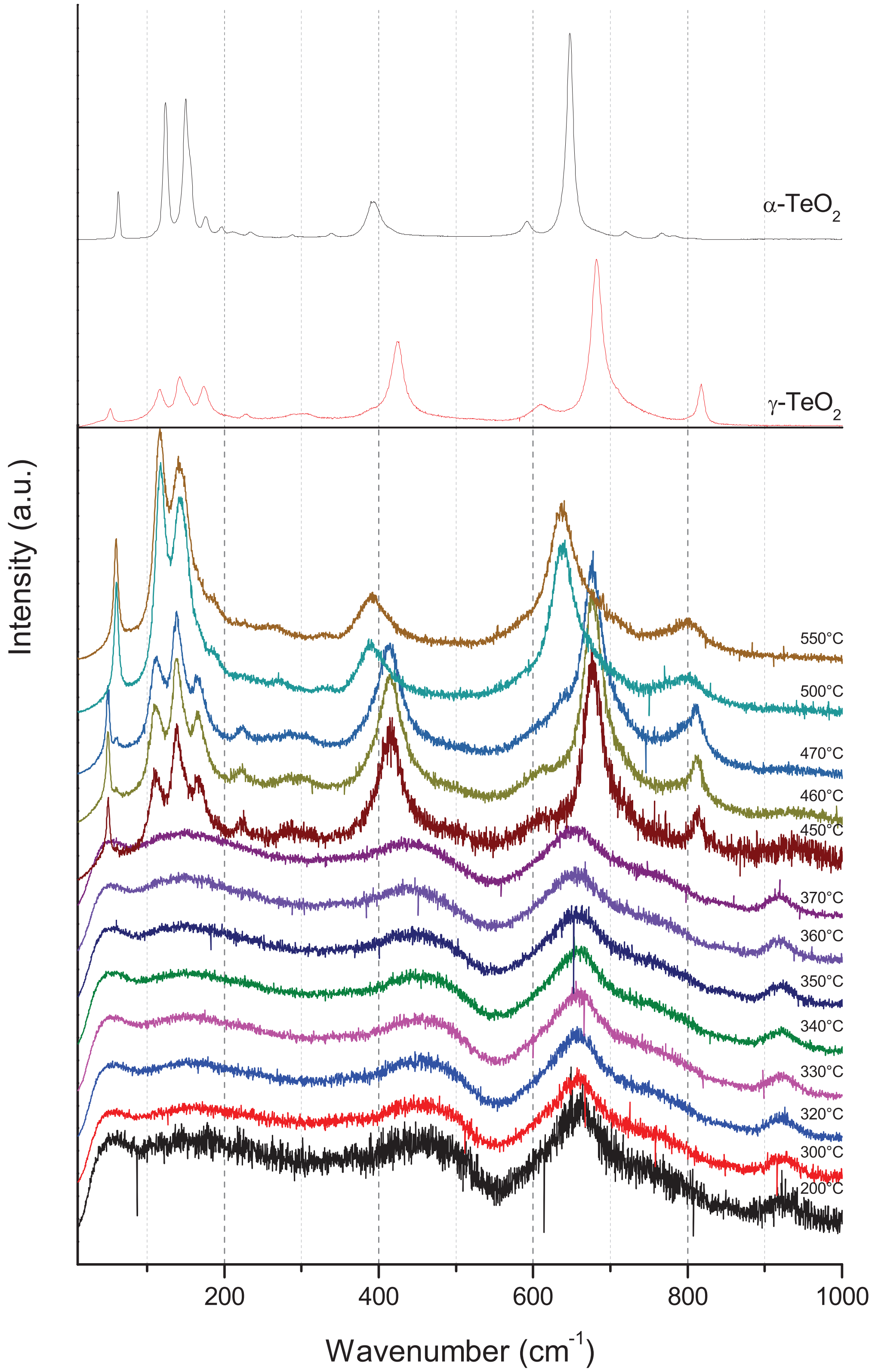

Figure 2.5: Raman spectra of the 92.5%TeO_2 + 7.5%WO_3 system at various temperatures and reference spectra of $\alpha-\mathrm{TeO}_2$ and $\gamma-\mathrm{TeO}_2$.

2.2.2 The 90%TeO$_2$ + 10%WO$_3$ system

Temperature *in situ* X-Ray diffraction results for the 90%TeO$_2$ + 10%WO$_3$ system are reported in Fig. 2.6. Here $\gamma-$TeO$_2$ starts to crystallise at 320 ℃ and at 340 ℃ appears well crystallised accompanying by secondary $\alpha-$TeO$_2$ phase (as shown in the enlarged insert). Contrary to 92.5%TeO$_2$ + 7.5%WO$_3$ system, the transition *glass* $\longrightarrow \gamma-TeO_2$ happens directly, without $\delta-$TeO$_2$ crystallisation. The quantity of $\alpha-$TeO$_2$ starts to increase earlier (at 380 ℃) in the system with larger amount of WO$_3$ modifier. However, the temperature of complete transformation to $\alpha-$TeO$_2$ stays the same as in previous system, *i.e.* 450 ℃.

As in previous system, *in situ* Raman spectroscopy with temperature shows the same sequence of polymorphs crystallisation, but the crystallisation temperatures are ≈40℃ higher than those defined by X-ray diffraction (see Fig. 2.7). That way, $\gamma-$polymorph appears at 380℃ together with secondary $\alpha-$polymorph and fully transforms into it at 500℃.

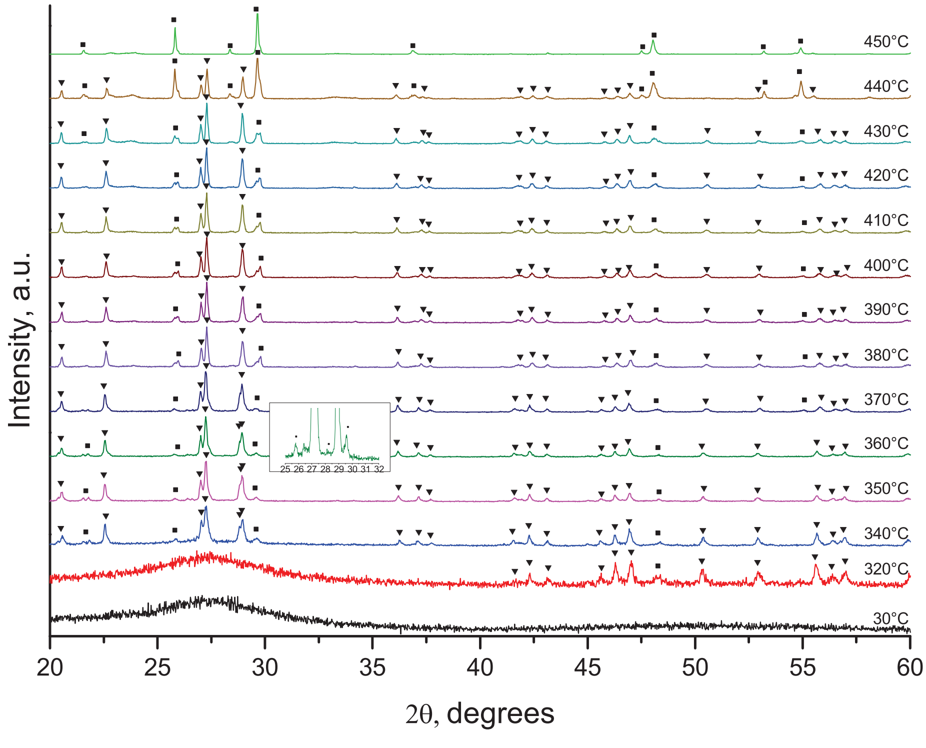

Figure 2.6: XRD powder patterns at various temperatures for a TeO$_2$ glassy sample containing 10WO$_3$ mol % (▼: $\gamma-$TeO$_2$, ■: $\alpha-$TeO$_2$).

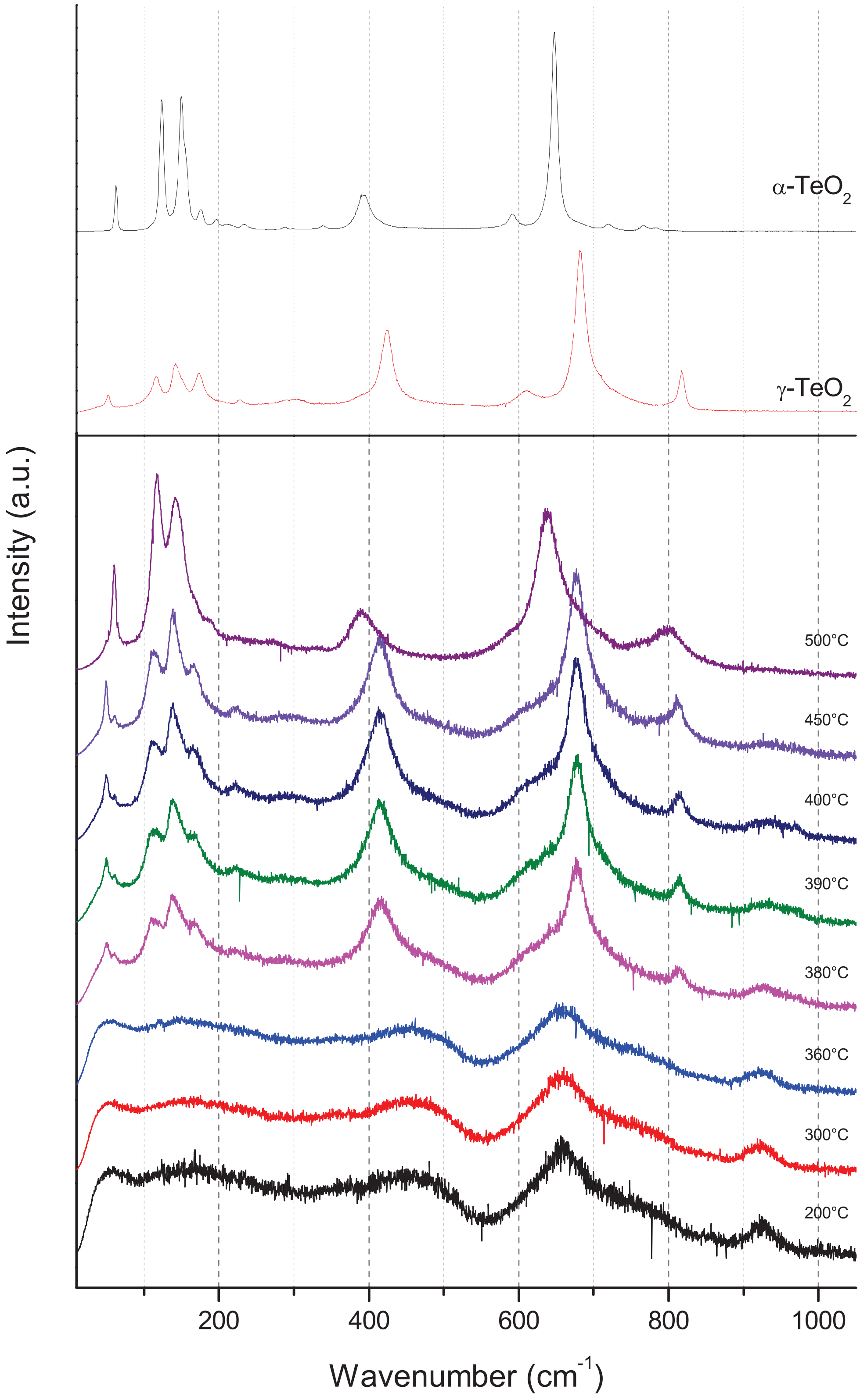

Figure 2.7: Raman spectra of the $90\%TeO_2 + 10\%WO_3$ system at various temperatures and reference spectra of $\alpha-TeO_2$ and $\gamma-TeO_2$.

2.2.3 The 95%TeO_2 + 5%$NbO_{2.5}$ system

For the TeO_2-glassed modified with 5 molar % of Nb_2O_5 the behaviour with temperature surprisingly differs from the results reported in [14]. X-ray diffraction shows (Fig. 2.8) that $\delta-TeO_2$ crystallises in very narrow temperature range 320–340 ℃ and then it fully transforms into $\alpha-TeO_2$ already at 350 ℃. As in both previous systems, $\delta-TeO_2$ crystallises simultaneously with $\alpha-TeO_2$ as secondary phase from the very beginning (as shown in the enlarged insert).

Similarly to the other systems, for the 95%TeO_2 + 5%$NbO_{2.5}$ system we cannot observe the crystallisation of $\delta-TeO_2$ by Raman spectroscopy, as its spectrum resembles the spectrum of the glass (Fig. 2.16), so that we observe only $\alpha-TeO_2$ crystallisation at 370℃ (Fig. 2.9).

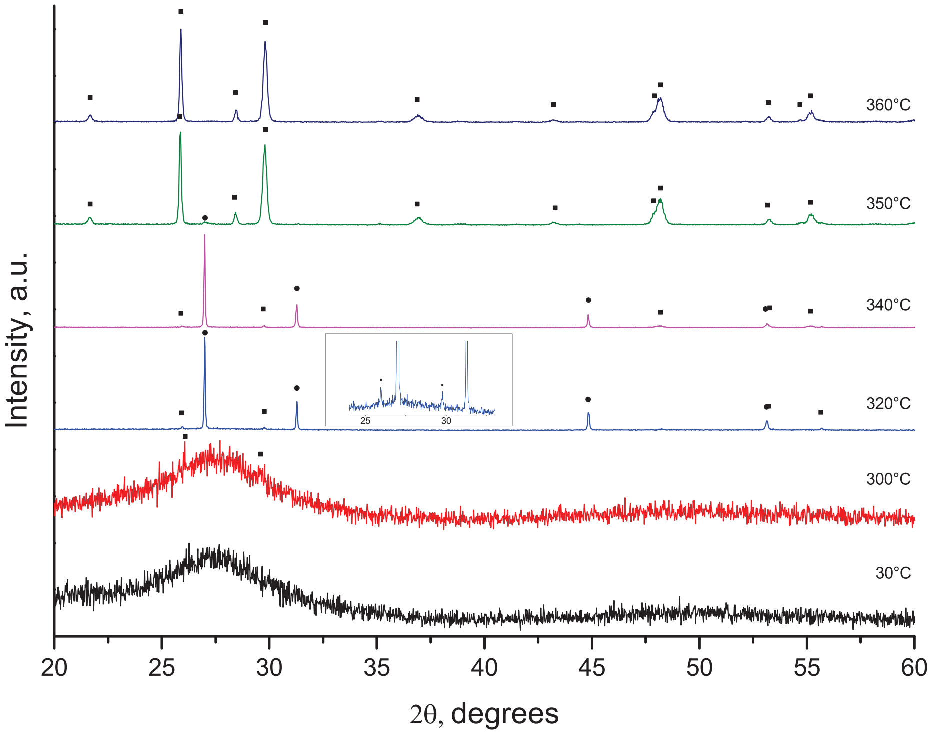

Figure 2.8: XRD powder patterns at various temperatures for a TeO_2 glassy sample containing 5$NbO_{2.5}$ mol % (●: $\delta-TeO_2$, ■: $\alpha-TeO_2$).

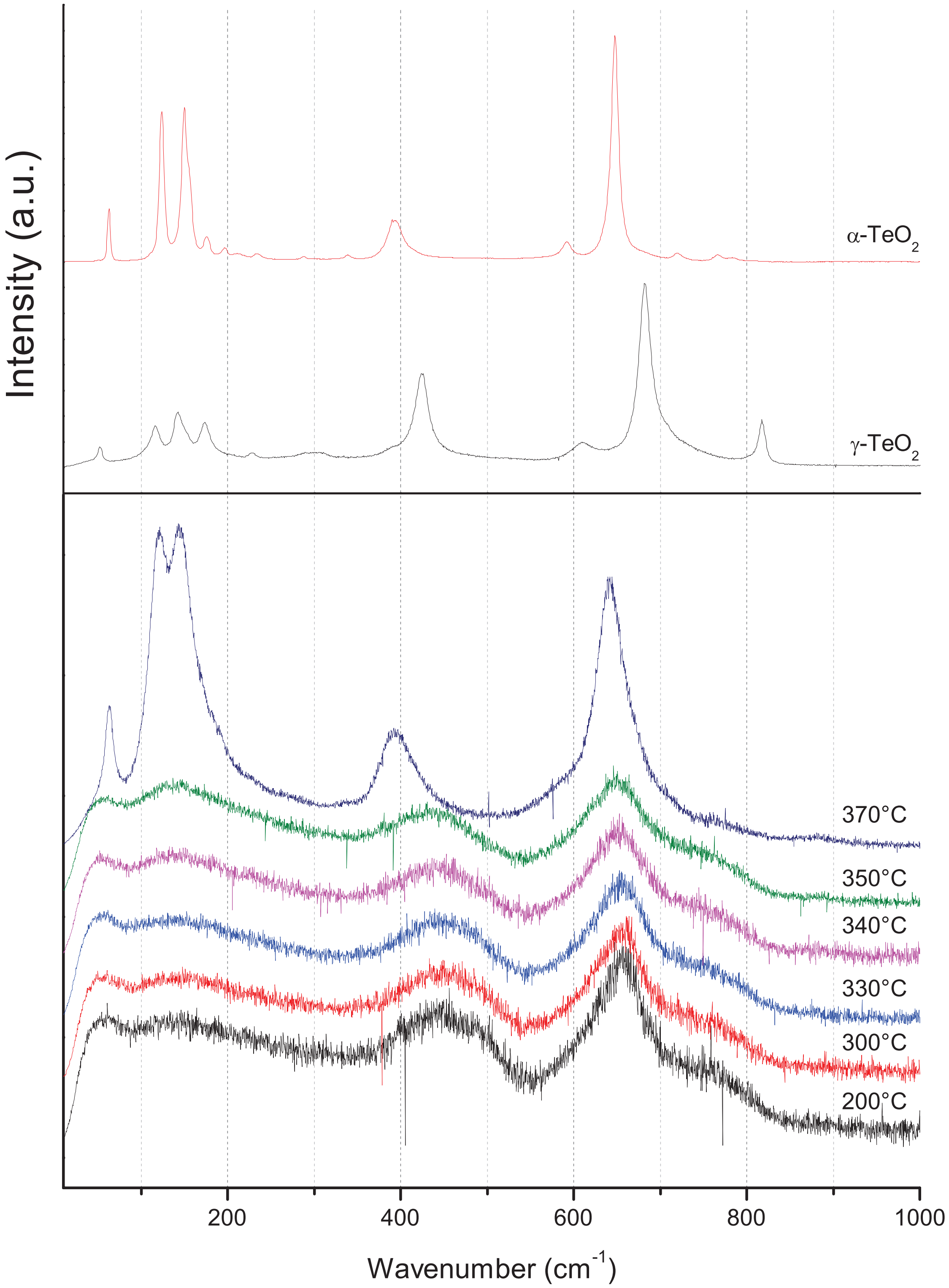

Figure 2.9: Raman spectra of the 95%TeO_2 + 5%$NbO_{2.5}$ system at various temperatures and reference spectra of $\alpha-TeO_2$ and $\gamma-TeO_2$.

2.2.4 The 95%TeO$_2$ + 5%PbO system

The studies for TeO_2-glass modified with 5 molar % of lead oxide show that $\gamma-$polymorph crystallises in a wide temperature range 280–400 ℃ (Fig. 2.10) and is always accompanied with small quantity of secondary $\alpha-$polymorph (see the enlarged insert). The peaks of the latter phase are well remarkable only at 270 ℃. The quantity of $\alpha-TeO_2$ start to increase at 410 ℃ so that at 450 ℃ the $\alpha-TeO_2$ phase predominates in the crystallised sample (410–440 ℃ range is not shown in Fig. 2.10).

Raman spectroscopy confirms once again these results and shows that $\gamma-TeO_2$ crystallises starting from 300℃ and completely transforms into $\alpha-TeO_2$ at 460℃ (Fig. 2.11).

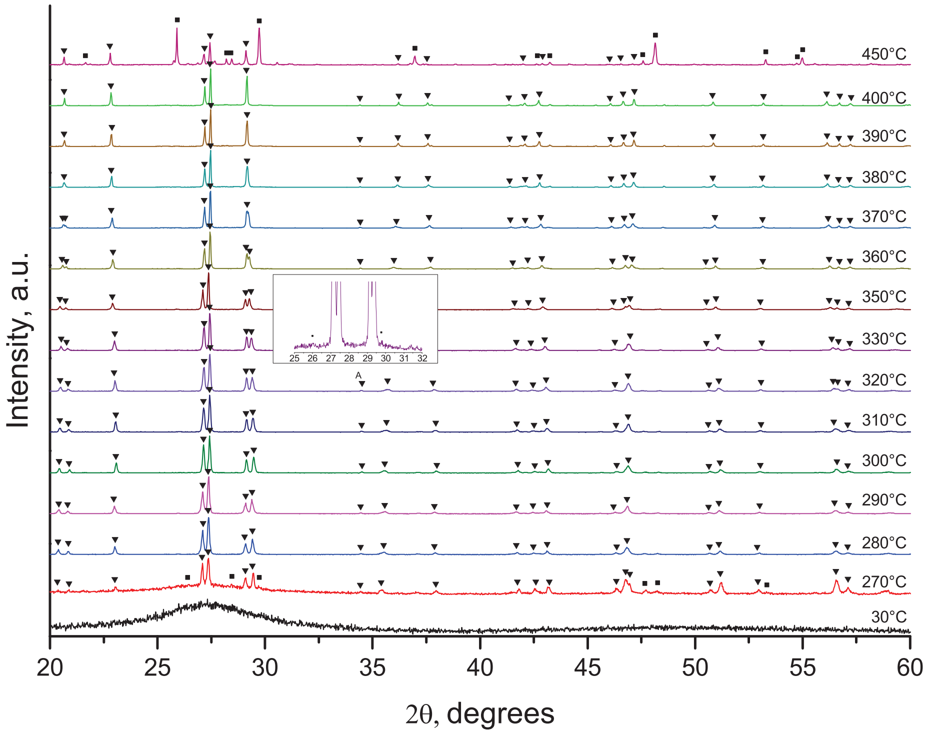

Figure 2.10: XRD powder patterns at various temperatures for a TeO_2 glassy sample containing 5PbO mol % (▼: $\gamma-TeO_2$, ■: $\alpha-TeO_2$).

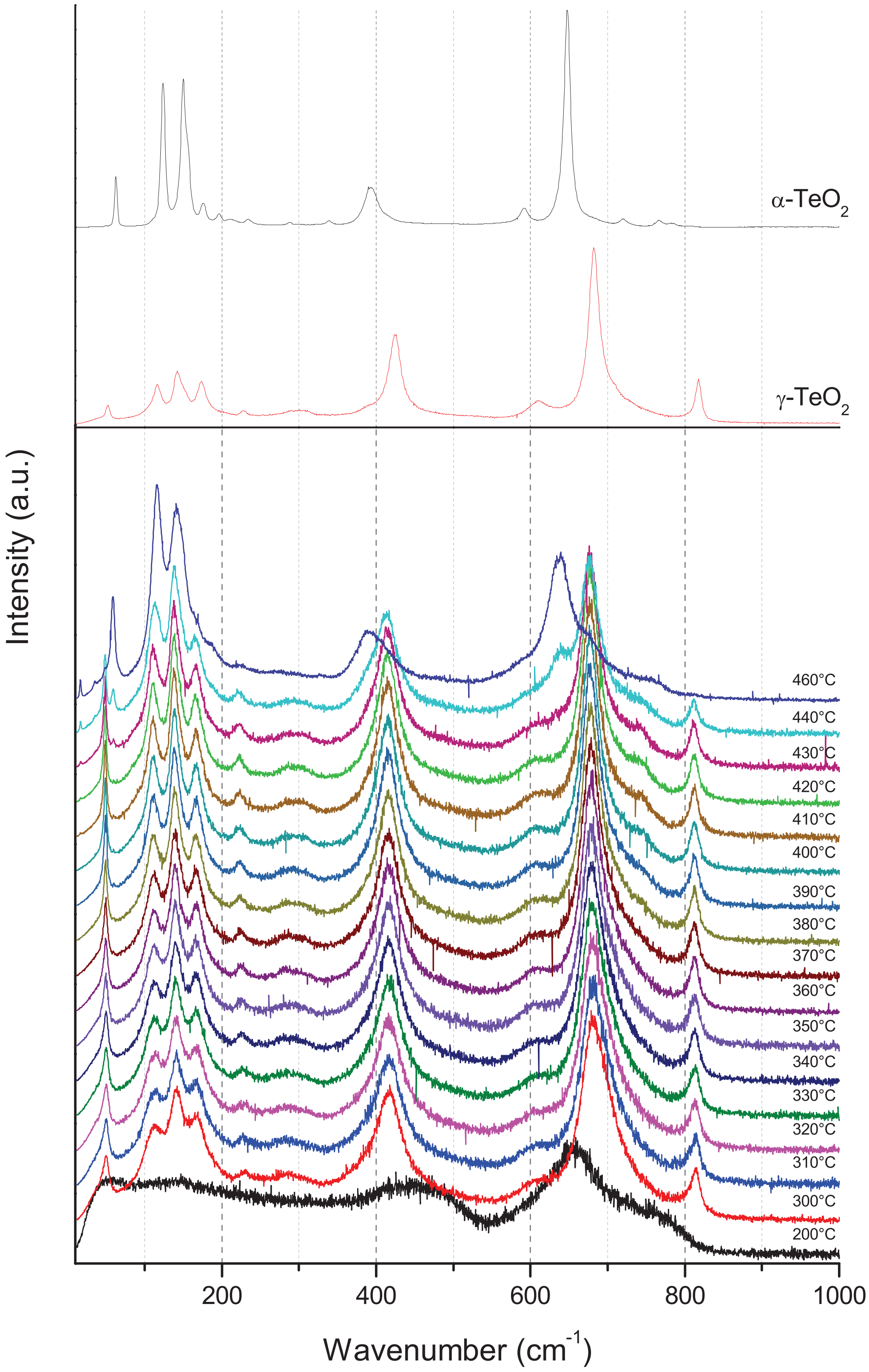

Figure 2.11: Raman spectra of the $95\%TeO_2 + 5\%PbO$ system at various temperatures and reference spectra of $\alpha-TeO_2$ and $\gamma-TeO_2$.

2.2.5 Discussion

We performed X-ray diffraction and Raman spectroscopy analysis of the glassy samples in order to define the optimal composition and conditions for crystallisation of $\gamma-$ and $\delta-\mathrm{TeO}_2$ polymorphs. In all the studied cases, the secondary $\alpha-\mathrm{TeO}_2$ polymorph always appears simultaneously with desired $\gamma-$ or $\delta-$polymorph.

We would like to recall from [9] that crystallisation from pure TeO_2-glass is extremely difficult for $\gamma-\mathrm{TeO}_2$ polymorph and unsuccessful for $\delta-\mathrm{TeO}_2$ polymorph. This implies that generally pure TeO_2 glass tends to crystallise directly into $\alpha-\mathrm{TeO}_2$. Whereas small quantities of modifiers oxides stabilise the pure TeO_2-glass and somehow help to form $\gamma-$ and $\delta-\mathrm{TeO}_2$ polymorphs.

These peculiarities of TeO_2-glasses behaviour allow us to suppose, that our unsuccessful attempts to obtain completely pure $\gamma-$ or $\delta-\mathrm{TeO}_2$ polymorphs rise from inhomogeneities of the glassy samples. In other words, some parts of our sample, which are well mixed with a modifier, crystallise to $\gamma-$ or $\delta-\mathrm{TeO}_2$, while other parts (pure TeO_2-glass) directly give $\alpha-\mathrm{TeO}_2$ polymorph at the same time. We will develop this hypothesis in the next section consecrated to the $\delta-\mathrm{TeO}_2$ polymorph synthesis.

2.3 $\delta-$TeO$_2$ synthesis

As we have shown in the previous section, the 95%TeO$_2$ + 5%NbO$_{2.5}$ composition provide the widest temperature range of crystallisation for $\delta-$TeO$_2$ polymorph and the lowest percentage of a modifier contest. Thus, we chose this composition for $\delta-$TeO$_2$ synthesis. Firstly, the glassy sample called here and after Glass_1D (about 0.5 g) was put in platinum crucible into tubular furnace for 1 hour at 340 ℃. The heating rate of the furnace was set to 2 ℃/min. The X-ray diffraction pattern for the obtained sample is reported in Fig. 2.12. We can see, that the sample is still in a glassy state but has a small quantity of the simultaneously crystallised $\alpha-$ and $\delta-$TeO$_2$ polymorphs. Hence, 1 hour is a too short time for the conventional furnace conditions. (Note, that during XRD measurements the sample was annealed primarily for 1 hour at 300 ℃ and 1 hour at 320 ℃.) Then the same sample was put in the same furnace at the same conditions for 5 hours more. In the XRD pattern of final sample (Fig. 2.13) we observe a well crystallised $\delta-$TeO$_2$ polymorph with a small quantity of $\alpha-$TeO$_2$ polymorph. The intensity of the first peak attributed to $\alpha-$TeO$_2$ makes about 5% of the intensity of the first $\delta-$TeO$_2$ peak.

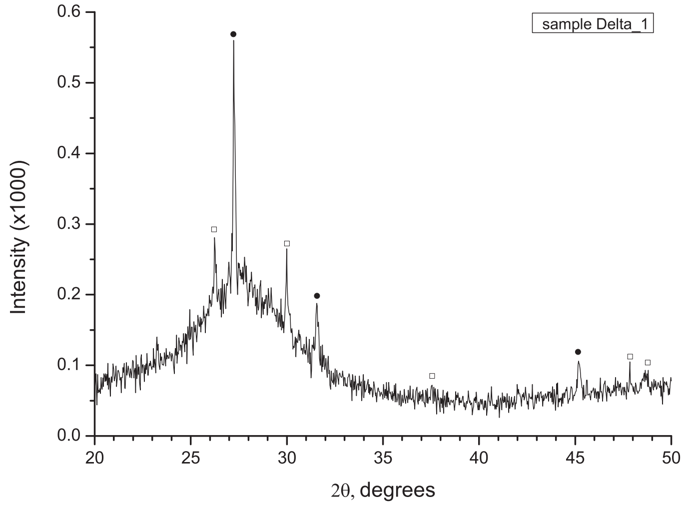

Figure 2.12: XRD powder pattern of the 95%TeO$_2$ + 5%NbO$_{2.5}$ glassy sample annealed in the furnace for 1 hour at 340 ℃ (□ – $\alpha-$TeO$_2$, • – $\delta-$TeO$_2$).

The $\alpha-$TeO$_2$ phase can crystallise together with $\delta-$TeO$_2$ polymorph because of a too high annealing temperature. To ensure the right choice of the temperature, we attempted to make $\delta-$TeO$_2$ polymorph from the other sample (called here and after Glass_2D) by annealing it at a lower (320 ℃) temperature for 20 hours. From the XRD pattern in Fig. 2.14 we conclude that this temperature was not enough for crystallisation of $\delta-$TeO$_2$ in conventional furnace, but in the same time was well enough for crystallisation

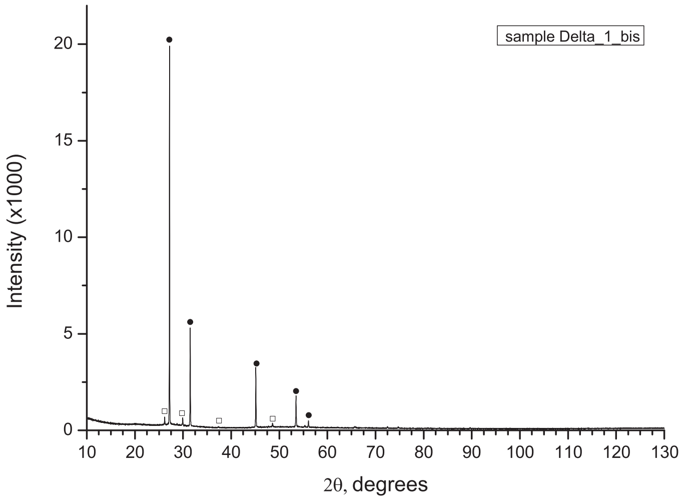

Figure 2.13: XRD powder pattern of the $\delta-\mathrm{TeO_2}$ obtained by annealing of the 95%$\mathrm{TeO_2}$ + 5%$\mathrm{NbO_{2.5}}$ glassy sample in the furnace for 6 hour at 340 ℃ (□ – $\alpha-\mathrm{TeO_2}$, • – $\delta-\mathrm{TeO_2}$).

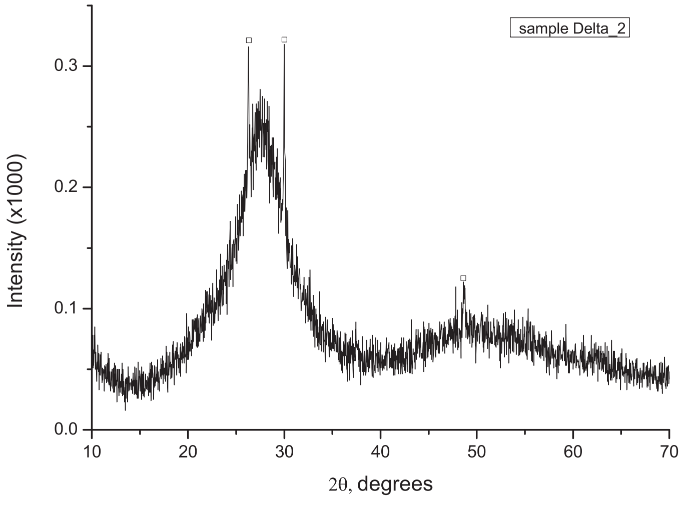

Figure 2.14: XRD powder pattern of the 95%$\mathrm{TeO_2}$ + 5%$\mathrm{NbO_{2.5}}$ glassy sample annealed in the furnace for 20 hour at 320 ℃ (□ – $\alpha-\mathrm{TeO_2}$).

of undesirable $\alpha-$TeO$_2$.

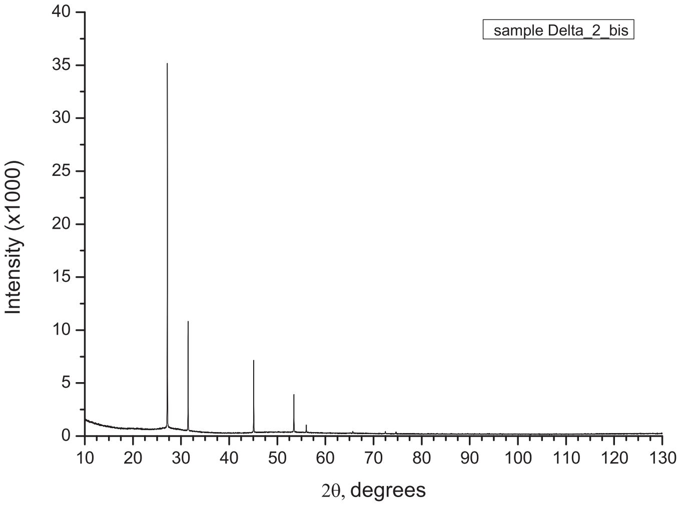

Figure 2.15: XRD powder pattern of the $\delta-$TeO$_2$ obtained by annealing of the 95%TeO$_2$ + 5%NbO$_{2.5}$ glassy sample (milled and melted four times) in the furnace for 6 hour at 340 °C.

The last factor that could be a reason of such a behaviour is a possible compositional inhomogeneity within the glassy sample. In order to check this hypothesis, we tried to homogenise the glassy sample as well as possible. To this end, we repeated the preparation procedure (milling the powder for about 30 minutes, melting at 800 °C, cooling and crushing the obtained glass) for the sample Glass_2D four times more. After this procedure, this sample was annealed at 340 °C for 6 hours and its resulting XRD pattern is reported in the Fig. 2.15. We can state, that this pattern has peaks corresponding only to $\delta-$TeO$_2$ polymorph. In such a manner, we obtained for the first time a perfectly pure (without secondary phase) $\delta-$TeO$_2$ polymorph.

In Fig. 2.16 we present the Raman spectra for different glassy samples and $\delta-$TeO$_2$ crystallised polymorphs. The black line represents the spectrum of the glassy sample milled and melted only one time and used to prepare $\delta-$TeO$_2$ sample called here and after Delta_1_bis, which contains secondary phase. The red line represents the spectrum of the glassy sample milled and melted four times and used to prepare $\delta-$TeO$_2$ sample without traces of $\alpha-$TeO$_2$ polymorph (called here and after Delta_2_bis). The spectra of the original glassy samples look like the spectra of homogeneous glasses and do not differ at all. Whereas the spectra of the $\delta-$TeO$_2$ samples crystallised from these original glasses have remarkable differences. The Raman spectrum of the $\delta-$TeO$_2$ sample Delta_1_bis is presented in blue and has obvious discrete lines superposed on the continuous background. These lines in the 150-200 cm^{-1} interval and near 680 cm^{-1} could be attributed to the

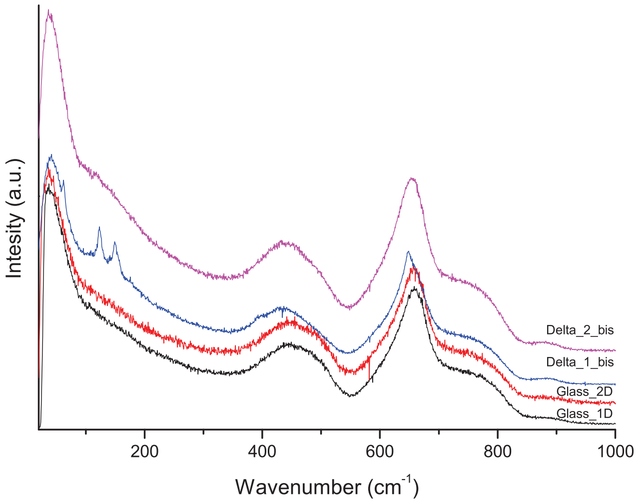

Figure 2.16: Raman spectra of the 95%TeO$_2$ + 5%NbO$_{2.5}$ glassy sample Glass_1D milled and melted only once (black), glassy sample Glass_2D milled and melted four times (red), $\delta-$TeO$_2$ obtained from the glass Glass_1D (blue), $\delta-$TeO$_2$ obtained from the glass Glass_2D (magenta).

presence of $\alpha-$TeO$_2$ polymorph in the sample according to the Raman spectrum of $\alpha-$TeO$_2$ (see Fig. 2.17) and to the XRD pattern of the sample (Fig. 2.13). Whereas, the spectrum of the pure sample Delta_2_bis (in magenta) really resembles the TeO$_2$-glass spectrum and does not have any discrete lines indicating the presence of any crystalline phases (contrary to XRD powder pattern (Fig. 2.15) with thin and intense peaks). All samples were prepared with 5 mol % of NbO$_{2.5}$ modifier and present a band near 880 cm^{-1}, which corresponds to the vibration of the NbO$_6$ polyhedra [90].

2.3.1 DSC analysis

Fig. 2.18 reports the DSC curves of the 95%TeO$_2$ + 5%NbO$_{2.5}$ glassy samples milled and melted ones (black line) and four times (red line). The DSC peaks were identified by variable temperature XRD studies. We are mostly interested in two peaks in the 350–380 ℃ range. For the glassy sample milled and melted only once they are not well separated and correspond to consequential crystallisation of $\delta-$TeO$_2$ and $\alpha-$TeO$_2$ polymorphs, whereas for the homogenised glassy sample these peaks are clearly more separated. The mechanism explaining the effect of homogenisation on phase crystallisation temperature could be the following: the non-homogenised glass contains zones more or less rich in modifier, that causes simultaneous $\delta-$TeO$_2$ (from rich in modifier grains) and $\alpha-$TeO$_2$ (from pure TeO$_2$-glass grains) crystallisation and, therefore, lower (367 ℃) $\delta \rightarrow \alpha$

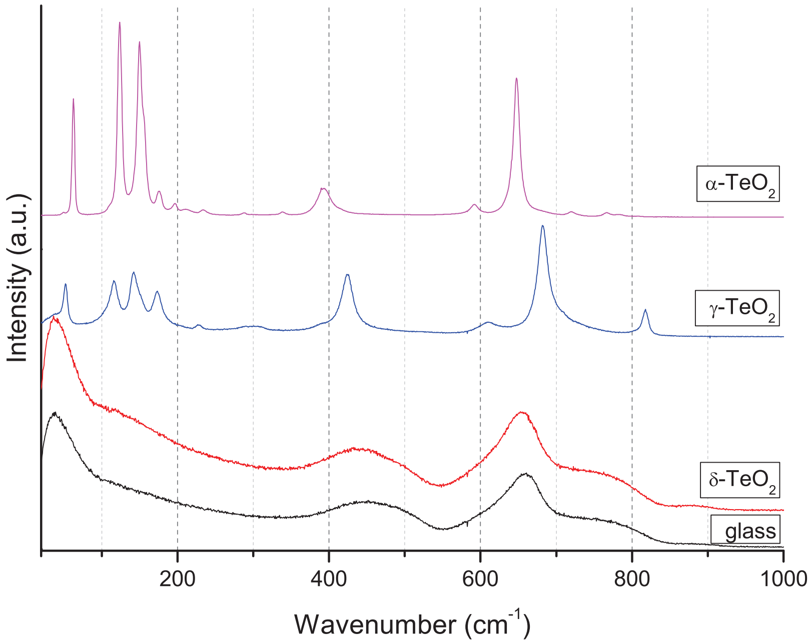

Figure 2.17: Raman spectra of the 95%TeO_2 + 5%$\text{NbO}_{2.5}$ glassy sample (black), $\delta-\text{TeO}_2$ (red), $\gamma-\text{TeO}_2$ (blue), $\alpha-\text{TeO}_2$ (magenta).

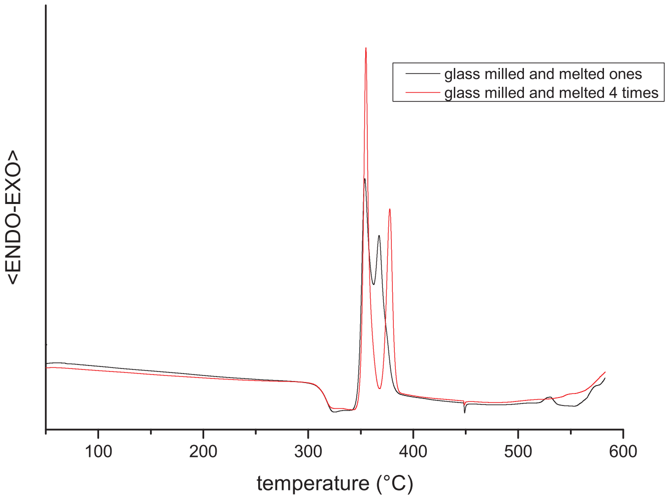

Figure 2.18: DSC curves for the glassy samples 95%TeO_2 + 5%$\text{NbO}_{2.5}$ milled and melted only once (black) and four times (red).

transition temperature. On the other hand, when the glass is homogenised, the modifier atoms are uniformly distributed in the sample that, in turn, prevents early $\alpha-$TeO$_2$ crystallisation, as there is no more grains with different modifier concentration. This shifts the peak on the DSC curve (Fig. 2.18) corresponding to $\alpha-$TeO$_2$ crystallisation to the higher temperature 377 ℃.

Note that the difference in the crystallisation temperatures defined by DSC method and by *in situ* XRD is due to the kinetic effect. As the time of one acquisition in XRD was about 55 minutes, atoms had enough time to arrange in crystalline structure at lower temperatures, while DSC measurements are continuous (with a constant heating rate of 10℃/min) and the crystallisation takes place at higher temperatures.

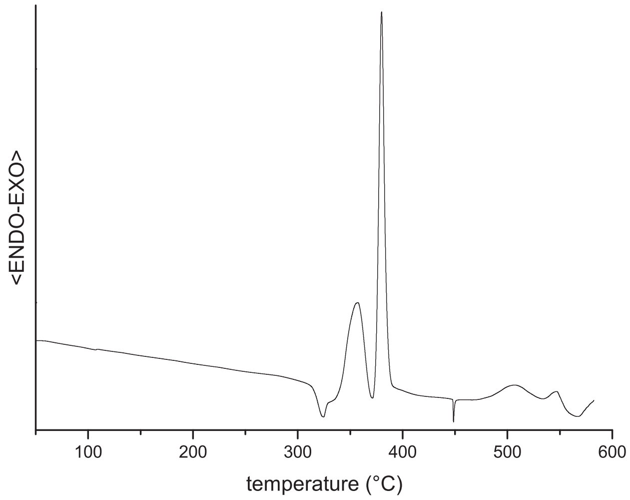

Figure 2.19: DSC curve for the $\delta-$TeO$_2$ sample Delta_2_bis crystallised from 95%TeO$_2$ + 5%NbO$_{2.5}$ glass at 340 ℃ for 6 hours.

Fig. 2.19 shows the DSC curve for crystallised $\delta-$TeO$_2$ sample. It resembles more the curve for the glassy sample than for the crystallised phase. Apparently, the sample is not completely crystallised and still has a glassy part, which is confirmed by the continuous background on the XRD pattern (Fig. 2.15). In such a way, the first observed phenomenon on the DSC curve is the glass transition (the steep change of the calorimetric signal) followed by crystallisation into $\delta-$TeO$_2$ polymorph (356 ℃) with following crystallisation of the whole sample into $\alpha-$TeO$_2$ (379 ℃).

However, as we already mentioned, $\delta-$TeO$_2$ is a metastable phase which is difficult to obtain and can have different behaviour from sample to sample. To back up this observation, let us now present some results for another $\delta-$TeO$_2$ sample. Sample called here and after Delta_3 was obtained from the glass of the same composition (with

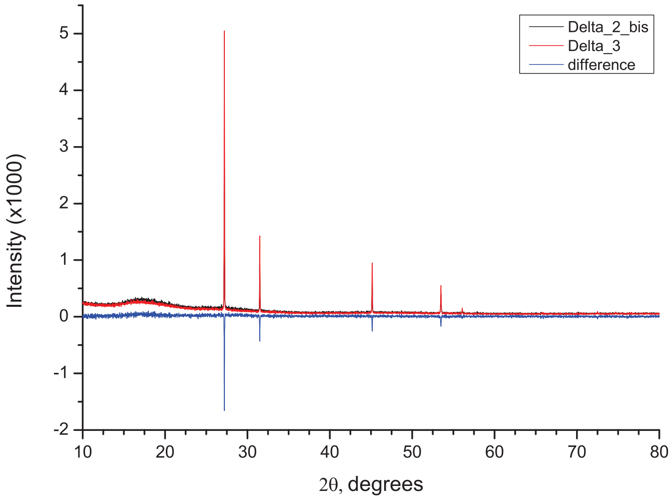

Figure 2.20: XRD powder patterns of the $\delta-\mathrm{TeO}_2$ Delta_2_bis (black) and $\delta-\mathrm{TeO}_2$ Delta_3 (red). The difference of the signals is shown in blue.

the same milling and melting procedure) and in the same conditions (annealing time and temperature) as sample Delta_2_bis. The only difference was in the quantity of crystallised powder: ≈ 0.4 g for sample Delta_2_bis and ≈ 0.2 g or sample Delta_3. We present the XRD patterns made in the same acquisition conditions for both samples in the Fig. 2.20. These are $\delta-\mathrm{TeO}_2$ samples without secondary $\alpha-\mathrm{TeO}_2$ polymorph, but with some quantity of the glassy powder. The curve hump at 15–20 degrees corresponds to the signal from the plastic sample holder. These patterns are almost the same, but the difference curve (blue) shows, that the peaks intensity of sample Delta_3 is higher, whereas the continuous background is slightly weaker. As the acquisition conditions were identical, we can qualitatively estimate, that sample Delta_3 is better crystallised than sample Delta_2_bis. This hypothesis can explain the DSC curve for sample Delta_3 (Fig. 2.21), which differs quite strongly from the one for sample Delta_2_bis (Fig. 2.19). It has a small steep change of the calorimetric signal (glass transition) and a thin peak at 382 ℃ corresponding to $\delta \rightarrow \alpha$ transition.

In summary, in this section we described the procedure for obtaining the pure $\delta-\mathrm{TeO}_2$ polymorph and emphasised the subtleties of its thermal behaviour. In spite of identical manipulations, it is extremely difficult to synthesise completely identical samples, as shown with XRD patterns (Fig. 2.20) and DSC curves (Fig. 2.19 and Fig. 2.21) for samples Delta_2_bis and Delta_3.

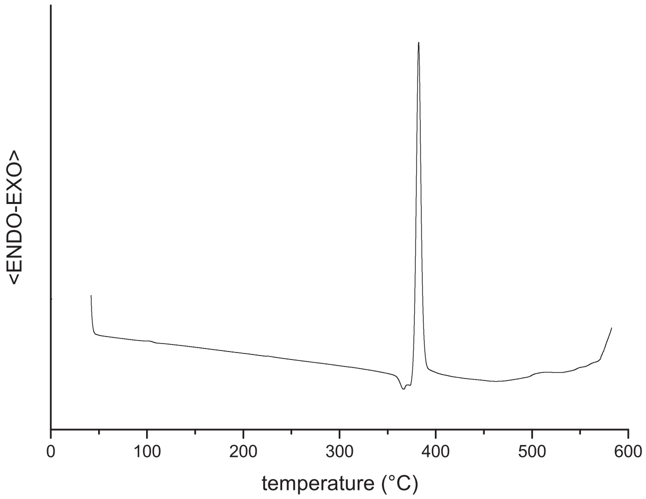

Figure 2.21: DSC curve for the $\delta-TeO_2$ sample Delta_3 crystallised from 95%TeO_2 + 5%$NbO_{2.5}$ glass at 340 ℃ for 6 hours.

2.4 $\gamma-TeO_2$ synthesis

For $\gamma-TeO_2$ synthesis we have chosen the 95%TeO_2 + 5%PbO system, as it has a really wide forming range in temperature and the lowest percentage of modifier oxide. In this section we present the XRD patterns of two samples called here and after Gamma_1 (Fig. 2.22) and Gamma_2 (Fig. 2.23). We obtained the first sample by annealing a glassy sample Glass_1G in the platinum crucible at 380 ℃ for 10 hours. We obtained a well crystallised $\gamma-TeO_2$ but with a small quantity of $\alpha-TeO_2$ like in the case of previous system. Then, in order to homogenise the sample, we repeated five times the preparation procedure (milling the powder for about 30 minutes, melting at 800 ℃ cooling and crushing) for the glassy sample Glass_2G. The Fig. 2.23 reports the XRD pattern of perfectly pure (without secondary phase) $\gamma-TeO_2$ polymorph prepared by the annealing of 95%TeO_2 + 5%PbO glassy sample at 320 ℃ for 14 hours.

Fig. 2.24 reports the Raman spectra of samples Gamma_1 ($\gamma-TeO_2$ with a small quantity of $\alpha-TeO_2$) and Gamma_2 ($\gamma-TeO_2$ without secondary phase). Let us recall now the analysis of the vibrational Raman spectrum of $\gamma-TeO_2$ polymorph made by A.P. Mirgorodsky *et al.* [10].

The conclusions are the following: the intense band (TeO_2-pulsation) near 680 cm^{-1} expresses highly asymmetric linkage Te–O$\cdots$Te. The other intense band near 430 cm^{-1} (symmetric stretching vibration TeOTe) corresponds to the other type of linkage in $\gamma-TeO_2$ – symmetric Te–O–Te bridges build up of two chemically equivalent Te–O bonds. The corresponding asymmetric stretching vibration TeOTe leads to a weaker band at

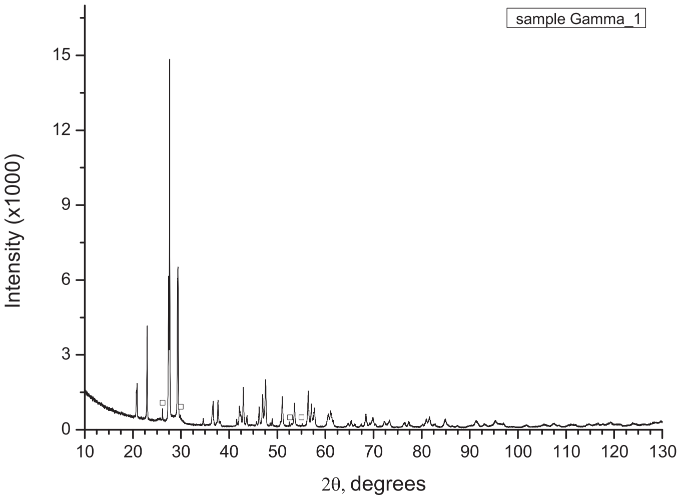

Figure 2.22: XRD powder pattern of the $\gamma-\mathrm{TeO_2}$ obtained by annealing of the 95%$\mathrm{TeO_2}$ + 5%PbO glassy sample in the furnace for 14 hour at 320 ℃ (□ – $\alpha-\mathrm{TeO_2}$).

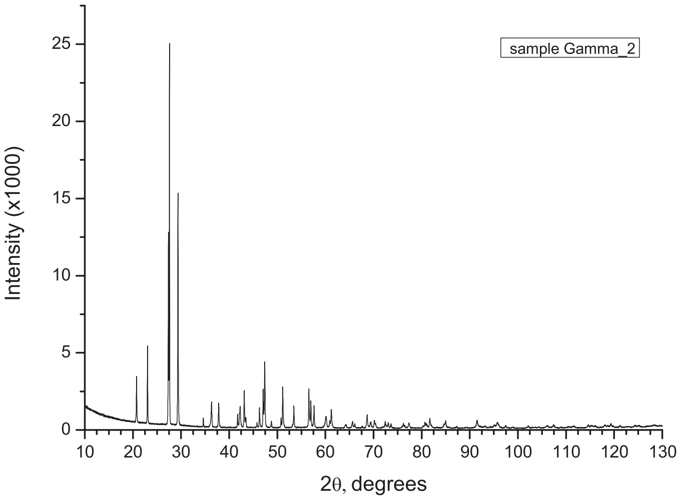

Figure 2.23: XRD powder pattern of the $\gamma-\mathrm{TeO_2}$ obtained by annealing of the 95%$\mathrm{TeO_2}$ + 5%PbO glassy sample (milled and melted four times) in the furnace for 14 hour at 320 ℃.

about 820 cm^{-1}.

The profiles of Raman spectra for samples Gamma_1 (with small quantity of $\alpha-\mathrm{TeO}_2$) and Gamma_2 (pure) are very alike apart from some subtle differences as, for example, at $\approx$ 750 cm^{-1}. It is difficult to emphasise the differences between these spectra like we have done for $\delta-\mathrm{TeO}_2$ in the previous section, as the Raman spectra of $\alpha-\mathrm{TeO}_2$ and $\gamma-\mathrm{TeO}_2$ polymorphs are rather close (see Fig. 2.17).

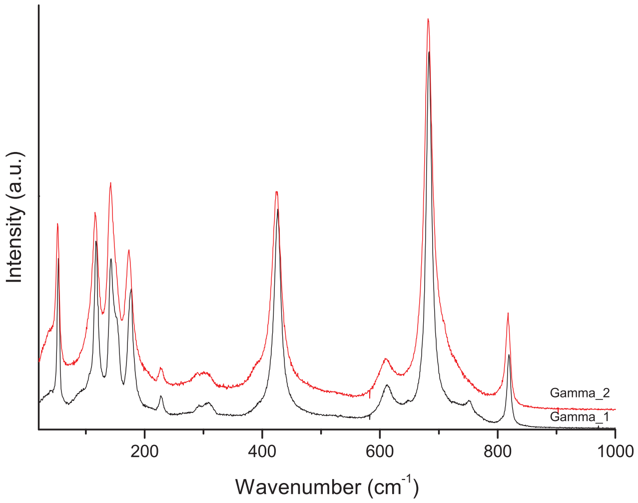

Figure 2.24: Raman spectra of the $\gamma-\mathrm{TeO}_2$ samples Gamma_1 obtained by annealing of the 95%TeO_2 + 5%PbO glassy sample milled and melted only once (black) and Gamma_2 obtained by annealing of the 95%TeO_2 + 5%PbO glassy sample milled and melted five times (red).

2.4.1 DSC analysis

DSC results for 95%TeO_2–5%PbO glassy sample are reported in Fig. 2.25. The black curve represents the result for normal glass (milled and melted only once) and the red one for homogenised glass (milled and melted five times). The first exothermic peak (313–320 ℃) corresponds to $\gamma-TeO_2$ crystallisation and follows by the second exothermic peak (438 ℃) that corresponds to $\gamma \rightarrow \alpha$ transition, according to XRD studies with temperature reported in Sec. 2.2.4. The endothermic peak at 510 ℃ corresponds to peritectic reaction of incongruent melting (according to phase equilibrium diagram from [88] reported in Fig. 2.27). For the normal glass $\gamma-TeO_2$ crystallisation peak is larger and less intense than one for homogenised glass and shifted to 7 ℃ on the left. This phenomenon could be explained by the effect of homogenisation in the same manner as described for 95%TeO_2–5%$NbO_{2.5}$ glasses in Sec. 2.3.1.

DSC curve for $\gamma-TeO_2$ sample Gamma_2 (pure) is reported in Fig. 2.26. The exothermic peak at 437 ℃ corresponds to $\gamma \rightarrow \alpha$ transition and follows by endothermic peak of incongruent melting at 508 ℃.

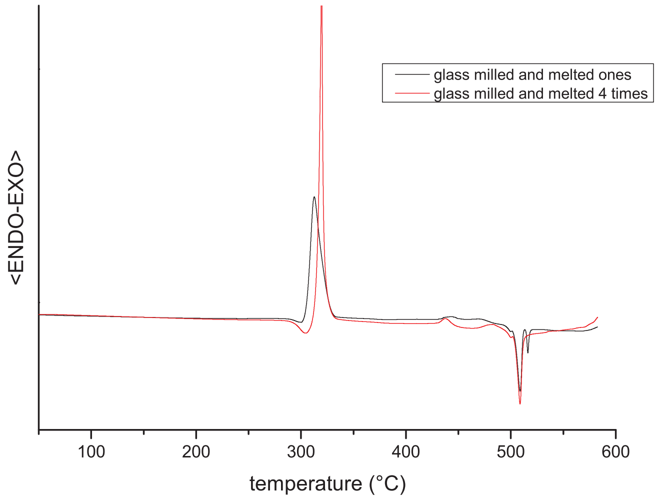

Figure 2.25: DSC curves for the glassy samples 95%TeO_2 + 5%PbO milled and melted only once (black) and four times (red).

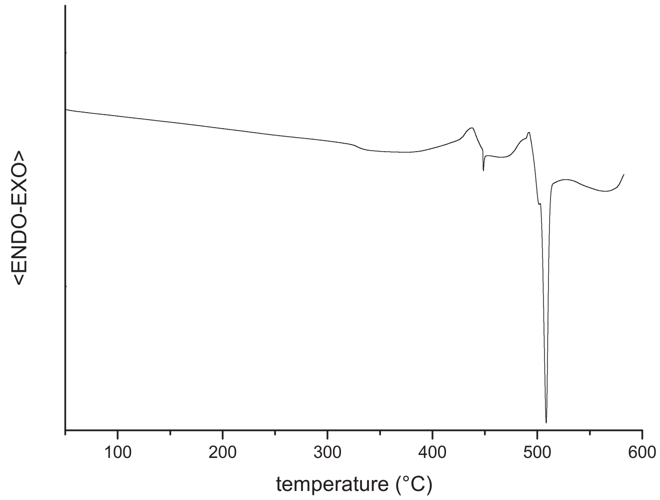

Figure 2.26: DSC curve for the $\gamma-\mathrm{TeO_2}$ sample crystallised from 95%$\mathrm{TeO_2}$ + 5%PbO glass at 320 ℃ for 14 hours.

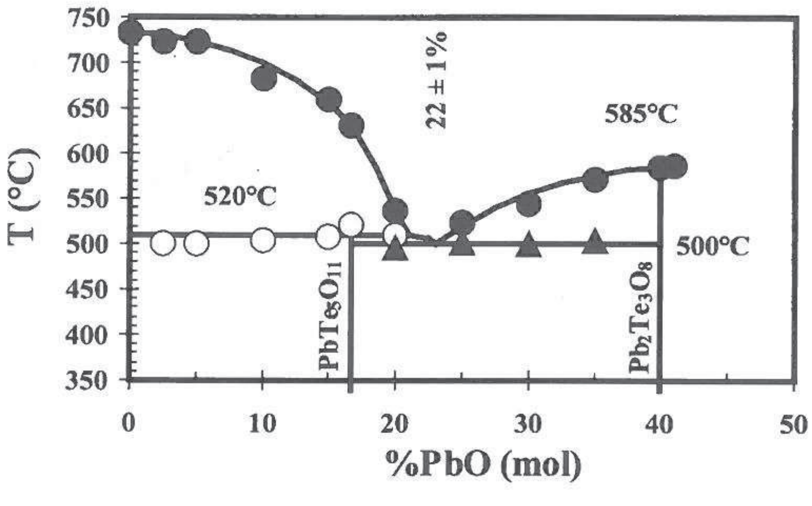

Figure 2.27: Phase equilibrium diagram of the $\mathrm{TeO_2}$–PbO system.

2.4.2 Evolution of the cell parameters during crystallisation of $\gamma-$TeO$_2$

We investigated the thermal expansion of the $\gamma-$TeO$_2$ polymorph in the 30–370 ℃ temperature range. The experimental results and the results of the linear fitting are reported in Fig. 2.28 and in Table 2.1 respectively. This is a normal thermal expansion with slopes in the range 10^{-5} – 10^{-4} Å/℃ depending on the crystalline direction.

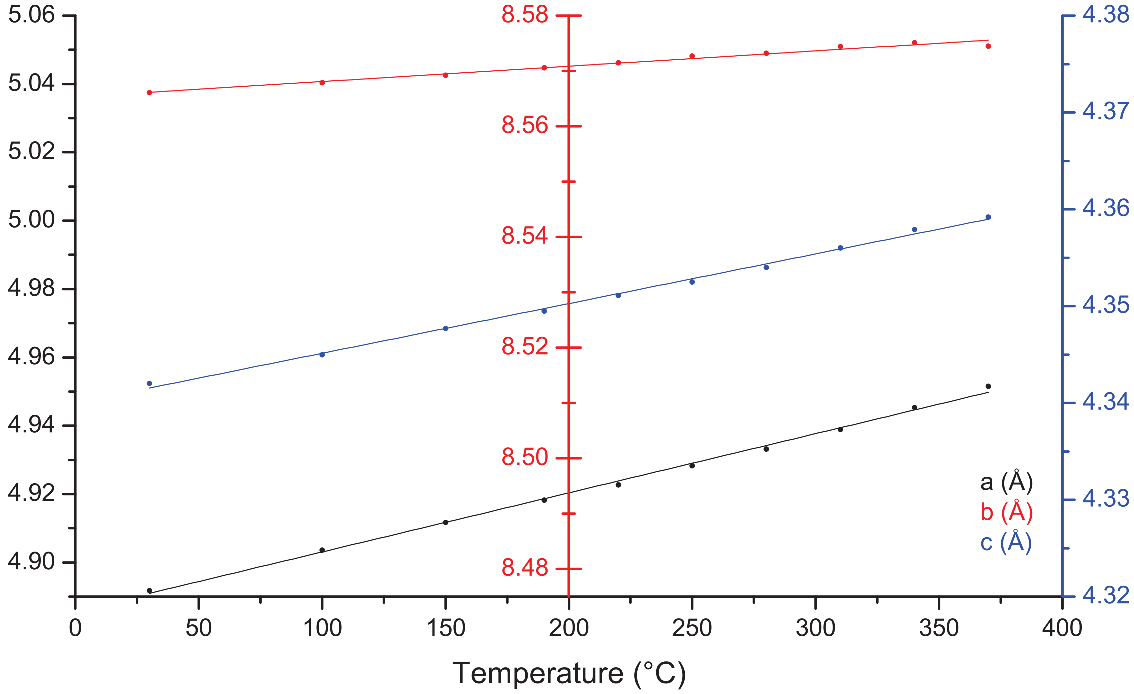

Figure 2.28: Evolution of the $\gamma-$TeO$_2$ cell parameters with temperature during thermal expansion. The cell parameters are presented in black (a), red (b) and blue (c). The lines represent the linear fitting.

In contrast to the normal thermal expansion of the *crystallised* $\gamma-$TeO$_2$ polymorph, the evolution with temperature of the $\gamma-$TeO$_2$ cell parameters *during* crystallisation from the glass surprisingly differs. We found out that the cell parameters ratio does not settle definitively at the first moment of crystallisation. Fig. 2.29 shows the evolution of the cell parameters with temperature during crystallisation of the $\gamma-$TeO$_2$ polymorph from the glassy sample. The b and c cell parameters increase linearly up to 380 ℃, where the line slope decreases and the cell parameters tend to reach their settled values. The a cell parameter exhibits a surprising behaviour decreasing with the increase of temperature. The results of the linear fitting (excluding the points at 390 ℃ and 400 ℃) are reported

Table 2.1: Parameters for the linear fitting of the data for $\gamma-$TeO$_2$ thermal expansion.

	$y = y_0 + kx$	
Cell parameter	y_0, Å	k, Å/ °C
a	4.886	$1.7 \cdot 10^{-4}$
b	8.565	$2.8 \cdot 10^{-5}$
c	4.340	$5.1 \cdot 10^{-5}$

in Table 2.2. In addition to the negative slope for a cell parameter, the absolute slope values for all cell parameters are significantly higher than for $\gamma-$TeO$_2$ thermal expansion.

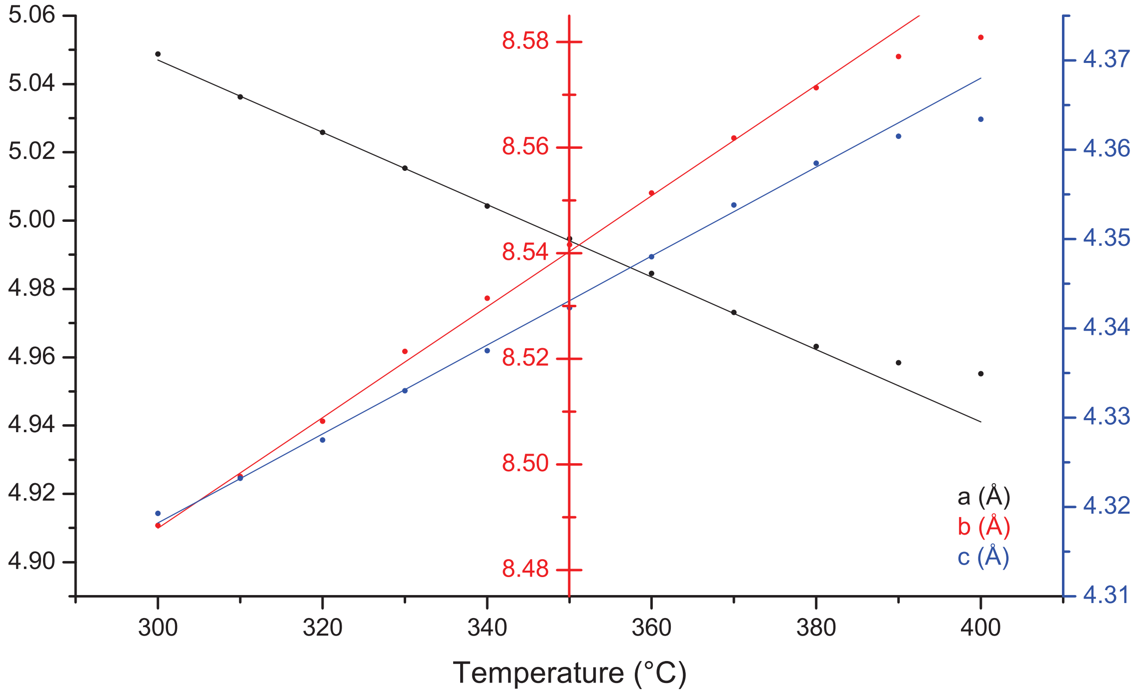

Figure 2.29: Evolution of the cell parameters with temperature during crystallisation from the glassy sample. The cell parameters are presented in black (a), red (b) and blue (c). The lines represent the linear fitting (excluding the points at 390°C and 400°C).

We recall here that in this XRD experiment each acquisition took 55 minutes. This means that the evolution shown in Fig. 2.29 corresponds to ≈ 11 hours. In such a way, this phenomenon has not necessarily only thermal character but also kinetic. In order to demonstrate the kinetic effect in $\gamma-$TeO$_2$ polymorph crystallisation, we performed an XRD experiment with long temperature plateau as shown in the upper part of Fig. 2.30. Fig. 2.30 reports the results of the cell parameters evolution with time at three different temperatures (300 °C, 350 °C, 370 °C). The data show that the dependency character is

Table 2.2: Parameters for the linear fitting of the data for $\gamma-\mathrm{TeO_2}$ crystallisation from the glass (excluding the points at 390℃ and 400℃).

	$y = y_0 + kx$	
Cell parameter	y_0, Å	k, Å/ ℃
a	5.365	$-1\cdot10^{-3}$
b	8.173	$1\cdot10^{-3}$
c	4.169	$4.9\cdot10^{-4}$

not linear at all: the cell parameters change significantly during the first 10 hours and then continue to change slowly during the next 14 hours.

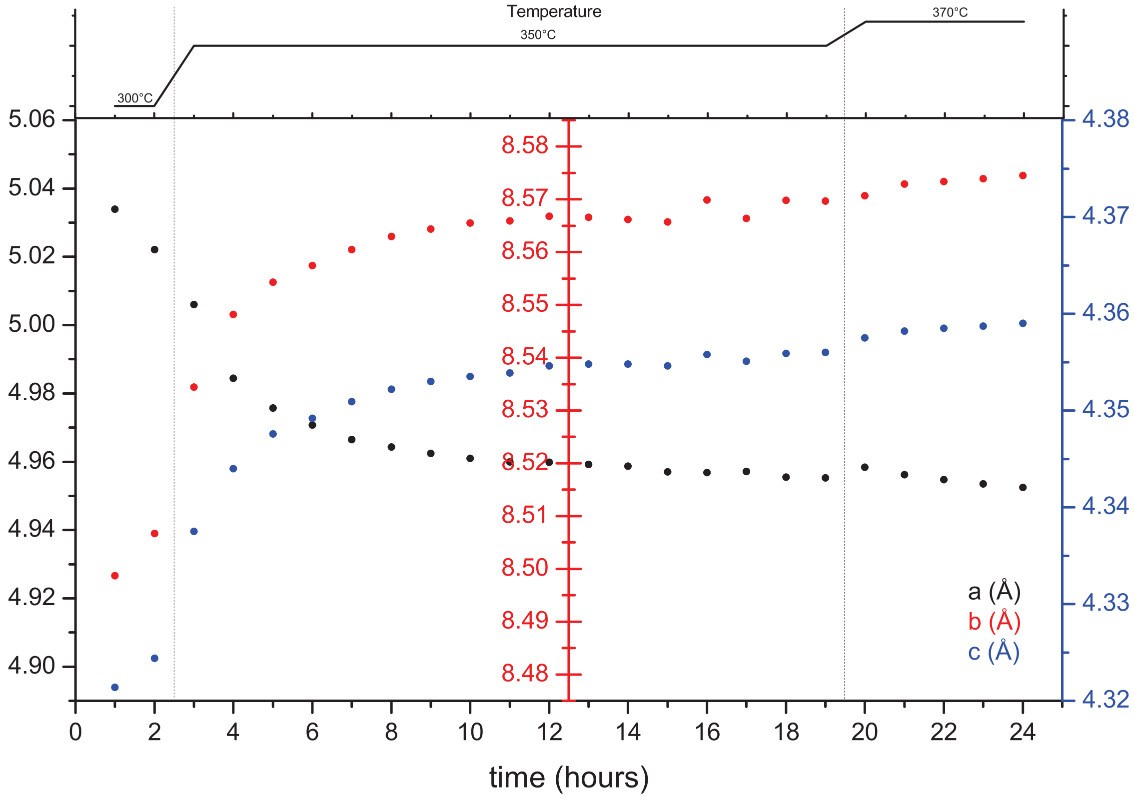

Figure 2.30: Evolution of the cell parameters with time and at different temperatures. The heating scheme is given on the top of the figure. The cell parameters are presented in black (a), red (b) and blue (c).

The combined results for thermal expansion and for crystallisation with temperature for each cell parameter separately are given in Fig. 2.31. We can clearly see, as was discussed above, that the first crystallised phase is rather different from the one at room temperature. Only after heating for several hours (at the same or different temperatures) the crystallising $\gamma-\mathrm{TeO_2}$ phase reaches the stable state (*i.e.* the state with the same ratio in cell parameters as for $\gamma-\mathrm{TeO_2}$ at the room temperature).

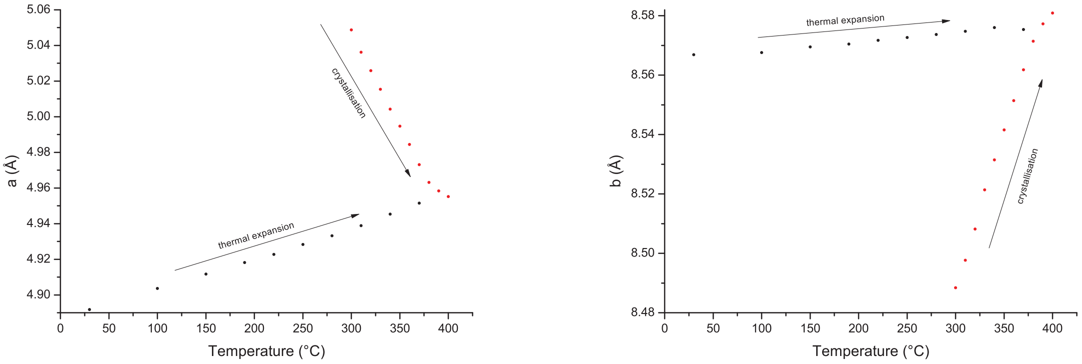

(a) a cell parameter.

(b) b cell parameter.

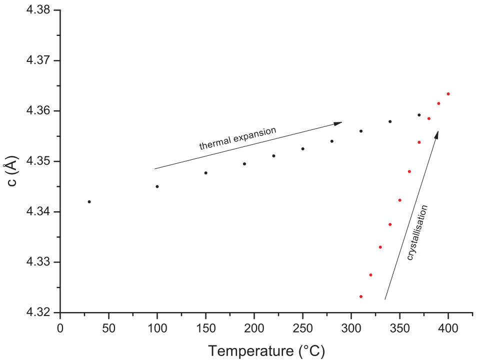

(c) c cell parameter.

Figure 2.31: The results for thermal expansion (black points) and for crystallisation with temperature (red points) for $\gamma-$TeO$_2$ cell parameters.

2.5 Conclusion

In this chapter we presented the synthesis of $\delta-\mathrm{TeO_2}$ and $\gamma-\mathrm{TeO_2}$ polymorphs of high purity (without secondary $\alpha-\mathrm{TeO_2}$ phase). The $\delta-\mathrm{TeO_2}$ was synthesised from 95%$\mathrm{TeO_2}$ + 5%$\mathrm{NbO_{2.5}}$ glassy sample and $\gamma-\mathrm{TeO_2}$ from 95%$\mathrm{TeO_2}$ + 5%PbO glassy sample. We performed the X-ray diffraction and Raman spectroscopy studies with variable temperature to define the optimal composition and temperature for synthesis.

We demonstrated, that the homogenisation of the glassy samples leads to improvement of the crystallised samples quality. Basing on X-ray diffraction and DSC studies and on synthesis attempts, we proposed the hypothesis about the mechanism explaining the effect of homogenisation of glassy samples on purity of crystallised phases. It consists in a sumption, that non-homogenised glasses contain powder grains more or less rich in modifier. Some grains (of pure glass) directly crystallise in $\alpha-\mathrm{TeO_2}$ polymorph, while other grains (rich in modifier) crystallise in $\delta-\mathrm{TeO_2}$ or $\gamma-\mathrm{TeO_2}$ polymorph.

We have also studied the evolution of the $\gamma-\mathrm{TeO_2}$ cell parameters during glass devitrification and during heating the crystallised sample. When crystallising from the glass, $\gamma-\mathrm{TeO_2}$ cell parameters ratio changes during several hours before reaching the stable state.

In perspective, it is interesting to deepen the understanding of the factors influencing on the crystallisation of pure $\delta-\mathrm{TeO_2}$ and $\gamma-\mathrm{TeO_2}$ samples. The quantity of the sample and quenching technique can strongly impact on crystallisation result. On the one hand, it is more difficult to homogeneously cool down a larger sample by conventional method and on the other hand, such techniques as twin-roller quenching allow to perform a faster quenching of the sample.

Chapter 3

Interatomic potentials for TeO_2 system

3.1 Interatomic Interactions in TeO_2 system

We discussed the theoretical background of derivation of the IAP in Chapter 1. In this chapter, we want to minimise the difference between calculated and experimental structures (*i.e.* cell parameters and atomic positions) by changing the IAP parameters. We recall that we have chosen the Buckingham potential for short-range interaction and a core-shell model for both Te and O atoms of the forms:

$$U_{ij}(r) = A_{ij} e^{-r/\rho_{ij}} - C_{ij} r^{-6}$$

$$U^i_{cs} = \frac{1}{2} k^i_2 x^2$$

where index i or j is for the atom type (Te or O). As we consider two short-range interaction types (Te–O and O–O), this leads to 10 unknown variables: A_{ij}, ρ_{ij}, C_{ij} for each pair interaction and k^i_2 and q^i_{sh} (shell charge) for each atom type. A simultaneous fitting of 10 parameters is somewhat cumbersome and prevents understanding the role of each parameter in the structure optimisation. Hence, a solution this problem requires several simplified steps.

The first obvious step is the use of the IAP from existing libraries for O–O interaction, considering that it is transferable for our system. We used the one from the Catlow library [37] and it is reported in Table 3.1.

3.1.1 Te^{4+}–O^{2-} interaction

In order to simplify more our problem, we first used a rigid ion model for Te atoms to estimate short-range interaction parameters for Te^{4+}–O^{2-} interaction. Such an idealisation is possible in the $Cs_2Te_4O_{12}$ structure, where Te^{IV} atom electronic LP does not present

Table 3.1: Parameters of the Buckingham and shell model potentials for O^{2-}–O^{2-} interaction from the Catlow library [37]

Buckingham potential

	A_{OO}, eV	ρ_{OO}, Å	C_{OO}, eVÅ^6
O^{2-}_{sh}–O^{2-}_{sh}	22764.000	0.14900	27.87900

Shell model

	k_2^{cs}, eVÅ^{-2}	q_s, e
O^{2-}	74.92	-2.86902

any stereochemical activity, as Te^{IV} atom is located in the centre of a perfect octahedron (see Fig. 1.9 in Section 1.1).

However, this complex oxide contains four species and the IAPs for Te^{4+}–O^{2-}, Te^{6+}–O^{2-} and Cs^{1+}–O^{2-} interactions are not established. For this reason we had to make some assumptions in order to have a kind of starting point. In such a manner, we used the IAPs of the neighbour elements for Te^{4+}–O^{2-}, Te^{6+}–O^{2-} and Cs^{1+}–O^{2-} interactions.

Primary fitting results showed that potentials for Te^{IV} (that has a LP) and Te^{VI} (that has no LP) atoms are quite close to each other in the framework of the rigid-ion model. This implies that the short-range interaction between tellurium (IV and VI) atoms and oxygen atoms is very similar. At the same time, this implies that we can transfer the potential between rigid Te^{6+} ion and O^{2-} ion to (core-shell) Te^{4+} ion and O^{2-} ion when Te^{IV} atom is highly polarised (in the $\alpha-TeO_2$ structure, for example). In this way, the highly polarised Te^{IV} atom consists of a denuded core with a charge $+6$ and a shell with a charge -2, which is strongly shifted with respect to the core.

The short-range forces are set between Te core and O shell only, whereas the Te shell contributes only to Coulombic energy. We have also tested the conventional interaction when the short-range interatomic interaction is set between the shells, but this did not work well. In other words, we did not succeed to model the correct asymmetric Te^{IV} atom environments in $\beta-$ and γ-TeO_2. This is the first time that the short-range forces are applied to the core while using the core-shell model (the interactions scheme is reported in Fig. 3.1).

It is worthwhile to note here, that a direct application of potential model in the rigid ion frameworks gives a rutile-type structure for $\alpha-TeO_2$ with perfect octahedron coordination of Te^{IV} atoms.

Then, we included the core-shell model for Te^{IV} atoms with the shells superimposed on the cores and fitted the spring constant and shell charge for Te atom. We performed iterative fitting and optimisation procedures for α- and γ-TeO_2 polymorphs (Fig. 3.2) to

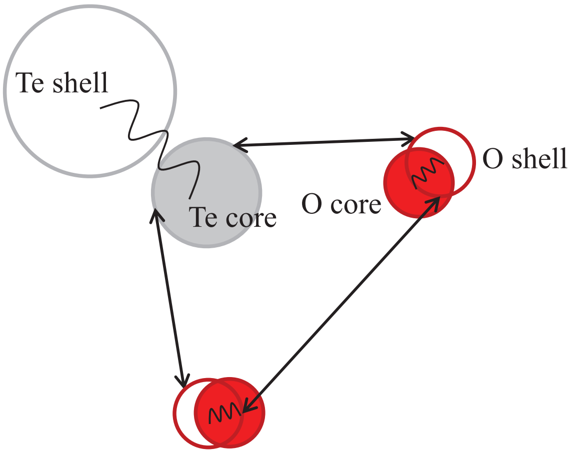

Figure 3.1: The scheme of considered interactions between atoms in TeO_2 system. The short-range interatomic interactions are indicated with arrows and intra-atomic core-shell interactions are illustrated with springs.

refine the Buckingham and core-shell parameters.

The as-obtained potential for Te^{4+}–O^{2-} interaction reproduced $\alpha-$ and $\gamma-TeO_2$ structures not very well (see Table 3.7 for the cell parameters comparison). In addition, this potential could not reproduce the correct tellurium atom coordination in $\gamma-TeO_2$. However, there is an important point to discuss. While fitting $\alpha-TeO_2$ structure, the short-range parameters A_{TeO} and ρ_{TeO} did not change significantly, unlike k_2^{Te}. One can imagine the rigid ion model as a core-shell model with an infinite spring constant value; thus by decreasing this parameter up to 35.736418 eVÅ^{-2} (*i.e.* by releasing the movement of Te atom shell 'LP') we observe transition of the Te^{IV} environment from octahedron to disphenoid. This fact confirms by means of empirical methods that the electronic LP is responsible for distorted rutile-type structure of $\alpha-TeO_2$ and the formation of TeO_4 disphenoid.

3.1.2 O^{2-}–O^{2-} interaction

The polarisation effect of oxygen atoms has a strong influence on Te^{IV} atoms environment. While fitting $\alpha-$ and $\gamma-TeO_2$ structures, we found that it is impossible to reproduce certain particularities in Te^{IV} atoms environment in $\gamma-TeO_2$ structure without changing the IAP for O–O pair. In $\gamma-TeO_2$, as we saw in section 1.1 of Chapter 1, Te^{IV} atom is coordinated with three short-bonded (< 2.02 Å) O atoms and one O atom with intermediate bond length (2.191 Å).

After refining the Catlow's O–O IAP, we obtained new Buckingham and core-shell

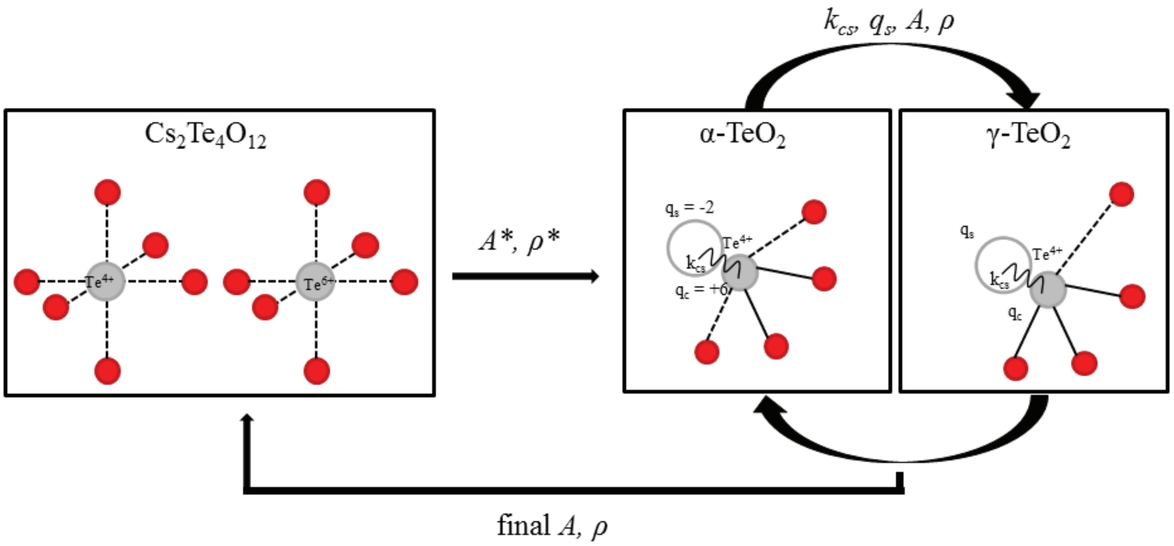

Figure 3.2: The scheme represents the fitting procedure of Buckingham potential parameters (A, ρ) and Te core-shell model parameters (k_2^{cs}, q_s) for Te^{4+}–O^{2-}. Parameters with an asterisk were derived in the frameworks of the rigid ion model against a $Cs_2Te_4O_{12}$ compound. While fitting α- and γ-TeO_2 polymorphs core-shell model for Te atom was included and iterative simultaneous fitting of all parameters was performed. Te atoms are represented in (light) grey and oxygen atoms in red (dark grey), solid lines stand for short (<2.02 Å) Te–O bonds and dotted lines for intermediate and elongated bonds (2.02 Å < Te–O distance < 2.36 Å). The Te atom shell (white circle) is shifted from the Te atom core and connected with it by spring, O atom's shells are not represented.

parameters, which allow to reproduce the correct Te^{IV} atoms coordination. If we compare the values in Table 3.1 and 3.5, we can see that all the parameters (A_{OO}, ρ_{OO}, k_2^O, q_{sh}^O) changed significantly. Let us consider in detail the core-shell parameters. The calculated O atom polarisability (the formulae 1.6 from the Chapter 1) has values of $\alpha_O = 0.11\ e\ \text{Å}^2/eV$ and $\alpha_O = 0.16\ e\ \text{Å}^2/eV$ for Catlow IAP and our potential respectively. This implies that the oxygen atoms polarisability in our potential model plays a more important role and is indeed responsible for a strong asymmetry in Te^{IV} atoms environment in γ-TeO_2 structure.

3.1.3 Te core-shell interaction

As we intend to model a glass structure with various Te–O bond lengths and bond angles, the transferability of the IAP is a property of crucial importance. This implies that the potential parameters related to a given ion-ion interaction in a specific crystal structure are likely to work fine for different crystal structures and mixed compounds.

In order to verify the transferability towards other chemical systems, we applied the derived IAPs to several TeO_2-based compounds (see Table 3.8 for the exhaustive list). Our potentials worked well for structures containing TeO_4, TeO_5 and TeO_6 units: the cell parameters and Te atom coordination were modelled correctly. However, for the structures in the M_2TeO_3 group (M = Li, Na, K, Cs) it was not the case. These structures contain TeO_3 trigonal pyramid units with short and strong Te–O bonds and strongly polarised Te^{IV} atom (see Fig. 3.3 for example).

It turned out, for these structures that the optimisation was not successful because the total energy convergence could not be achieved. The structure collapse was caused by a strong displacement of tellurium shell from its core, since the spring force was not enough strong to keep it. (See the left structure in Fig. 3.3, where the cell parameter c is 18.6 % less than the experimental value (see Table 3.6). Te atoms shells are shifted at 1.1 Å with respect to their cores and the minimum distance between Te and Cs atoms is unphysical small (2.168 Å)). Hence, the lack of the core-shell energy prevented the total energy convergence and lead to the instability of the system. Indeed, the increase of Te spring value up to 42.259877 and 46.123789 $eV\text{Å}^{-2}$ for Cs_2TeO_3 and K_2TeO_3 respectively lead to stabilisation of the systems (see the middle structure in Fig. 3.3 an Table 3.6 for the cell parameters comparison). The respective Te shells displacements with respect to their cores are 0.669 Å for Cs_2TeO_3 and 0.666 Å for K_2TeO_3. However, the set of different spring values for different structures is not satisfactorily from the transferability point of view.

Let us now consider the core-shell energy, U_{cs}, as a function of the core-shell distance for Te atom for different spring constant values (Fig. 3.4). As we can see, Cs_2TeO_3 and K_2TeO_3 structures are stable when the U_{cs} values are higher than the ones obtained with the smaller spring constant (35.736418 eVÅ^{-2}). Whereas, for $\alpha-$ and $\gamma-TeO_2$ the U_{cs} corresponding to the latter spring constant value is just enough sufficient.

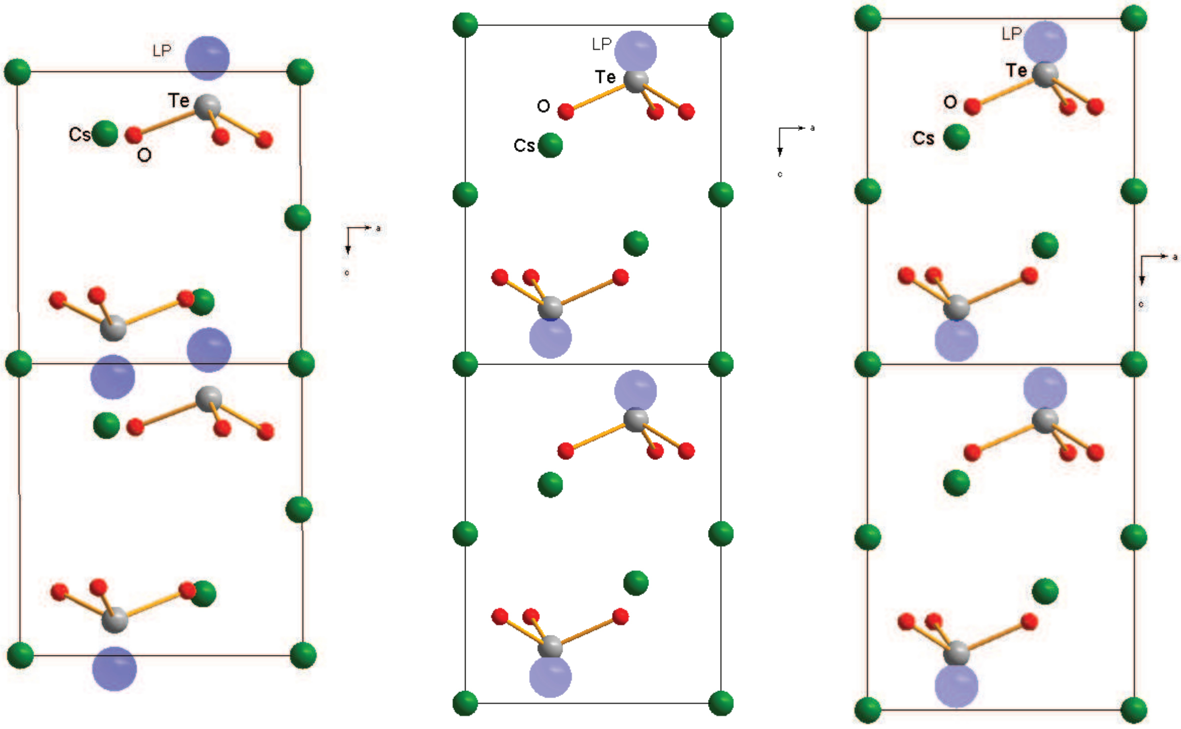

Figure 3.3: Cs_2TeO_3 structure modelled with different spring values for Te atoms core-shell model. The other IAPs parameters are from Table 3.5. The values of Te core-shell spring constants for the left, middle and right structures are k_2^{cs} = 42.259877 eVÅ^{-2}, k_2^{cs} = 46.123789 eVÅ^{-2}, and k_2^{cs} = 35.736418 eVÅ^{-2} and k_4^{cs} = 90 eVÅ^{-4} respectively.

This means that none of the values of harmonic spring constant, k_2^{cs}, can fit all the various TeO_x units with various shell separation distances. Thereby to compensate the lack of U_{cs} energy in the structures, where Te shell displacement is very significant (0.6–0.7 Å) and to avoid the excess of U_{cs} energy in the structures with smaller Te shell displacements, we fitted k_2^{cs} and k_4^{cs} parameters for anharmonic spring potential of the form:

$$U_{cs} = \frac{1}{2}k_2^{cs}x^2 + \frac{1}{24}k_4^{cs}x^4. \tag{3.1}$$

The Cs_2TeO_3 was successfully optimised with the new spring potential form (see the right structure in Fig. 3.3 and Table 3.6 for the cell parameters comparison). In such a manner, the anharmonic potential form smooths the transition between curves corresponding to different harmonic spring parameters.

3.1.4 Summary

In order to summarise and illustrate the main features of the derived IAPs, let us now demonstrate the development of the interaction model.

Firstly, if we use the rigid-ion model for Te atoms and Catlow IAP for O–O interaction, as in Table 3.2, we obtain a rutile-type structure for $\alpha-TeO_2$ with Te atoms coordinated to eight O atoms forming an octahedron. Fig. 3.5 shows a spatial view (on the left) and a c-axis projection (on the right) of such a structure.

Table 3.2: Parameters for Buckingham potential for TeO_2 system with Te atom represented in rigid-ion model and O^{2-}–O^{2-} IAP from Catlow library [37]

Buckingham potential			
	A, eV	ρ, Å	C, eVÅ^6
Te^{4+}–O^{2-}_{sh}	1595.266748	0.345867	1.0
O^{2-}_{sh}–O^{2-}_{sh}	22764.000	0.14900	27.87900

Shell model		
	k_2^{cs}, eVÅ^{-2}	q_s, e
O^{2-}	74.92	-2.86902

When we add the core-shell model for Te atoms and use the IAPs as reported in Table 3.3, we obtain a good for for of the $\alpha-TeO_2$ structure (Fig. 3.6 shows a spacial view (on the left) and a c-axis projection (on the right) of the resulting fit). However $\gamma-TeO_2$ structure is not correctly modelled: the cell parameters have large errors with respect to the experimental values (see Table 3.7) and TeO_4 units are connected with symmetrical double bridges (see Fig. 3.7).

Table 3.3: Parameters for Buckingham potential for TeO_2 system with Te atom represented in core-shell model with harmonic spring potential and O^{2-}–O^{2-} IAP from Catlow library [37]

Buckingham potential			
	A, eV	ρ, Å	C, eVÅ^6
Te^{4+}–O^{2-}_{sh}	1595.266748	0.345867	1.0
O^{2-}_{sh}–O^{2-}_{sh}	22764.000	0.14900	27.87900

Shell model		
	k_2^{cs}, eVÅ^{-2}	q_s, e
Te^{4+}	35.736418	-1.975415
O^{2-}	74.92	-2.86902

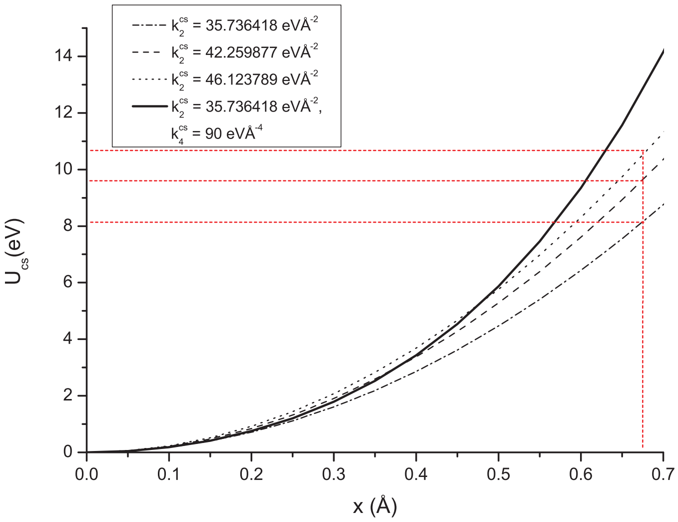

Figure 3.4: The core-shell potential energy for tellurium atom as a function of core-shell separation according to various k_2^{cs} and k_4^{cs} spring constants. Dashed-dotted, dashed and dotted lines correspond to k_2^{cs} = 32.058712, 42.259877, 46.123789 eVÅ^{-2} harmonic spring value. Bold solid line corresponds to core-shell potential including anharmonic term k_2^{cs} = 35.736419 eVÅ^{-2}, k_4^{cs} = 90 eVÅ^{-4} which provides smooth transition from low energies at short core-shell separation and higher energies at more significant core-shell separations.

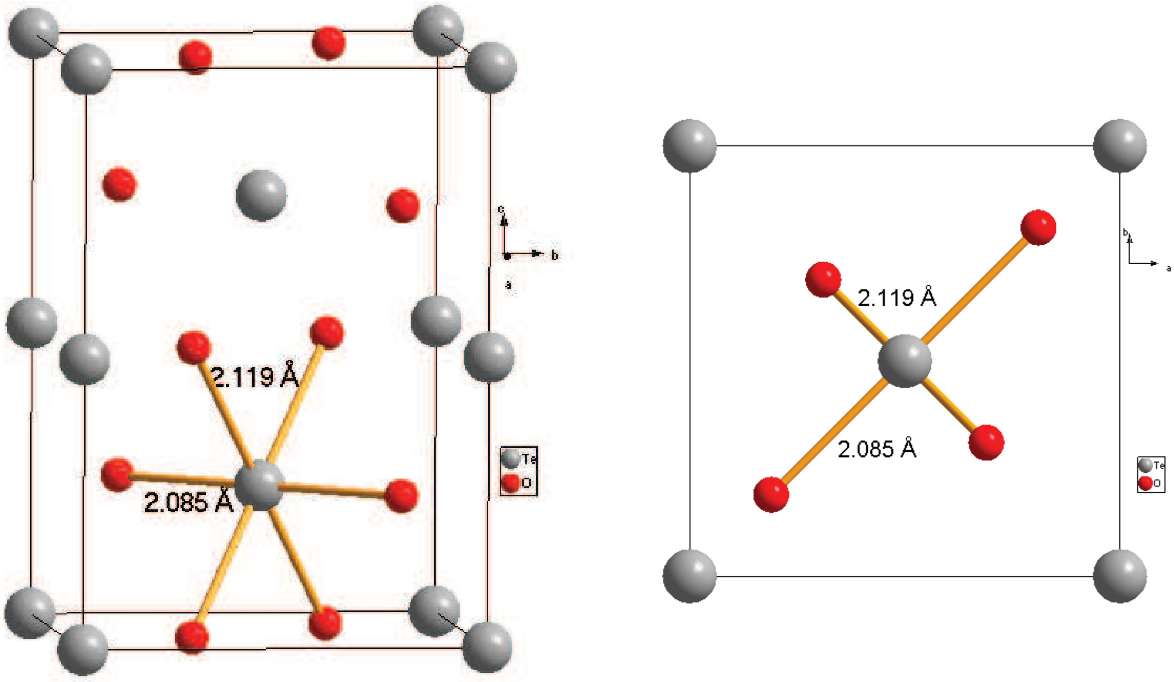

Figure 3.5: α−TeO$_2$ structure modelled with rigid-ion model for Te atoms and Catlow potential for O–O interaction (see Table 3.2). The spacial view is presented on the left and the c-axis projection on the right.

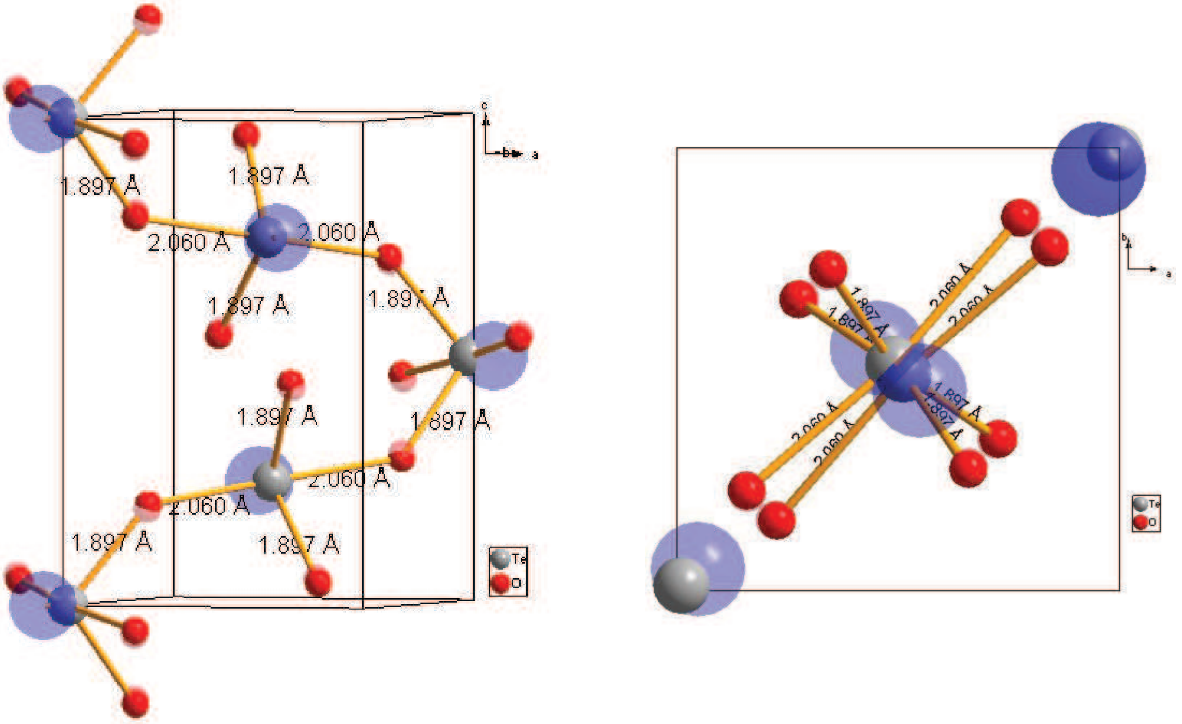

Figure 3.6: $\alpha-TeO_2$ structure modelled with core-shell model for Te atoms and Catlow potential for O–O interaction (see Table 3.3). The spacial view is presented on the left and the *c*-axis projection on the right. The transparent spheres in blue represent the Te atoms shells and in red represent the O atoms shells.

The change of the O–O IAP (Table 3.4) and particularly the increase of oxygen atoms polarisation strongly improves the fitting results for $\gamma-TeO_2$ structure. Fig. 3.8 illustrates the results for $\alpha-TeO_2$ (on the left) and $\gamma-TeO_2$ (on the right) structures. In order to emphasise the role of oxygen atom shells, they are shown in this figure as well. The values of core-shell distances for O atoms are 0.19 Å for $\alpha-TeO_2$ and 0.17 Å / 0.23 Å (for different oxygen atoms sites) for $\gamma-TeO_2$. This is 2 to 8 times larger than for the structures optimised using Catlow potential (0.05 Å for $\alpha-TeO_2$ and 0.02 Å / 0.11 Å for $\gamma-TeO_2$, see Fig. 3.6 and 3.7).

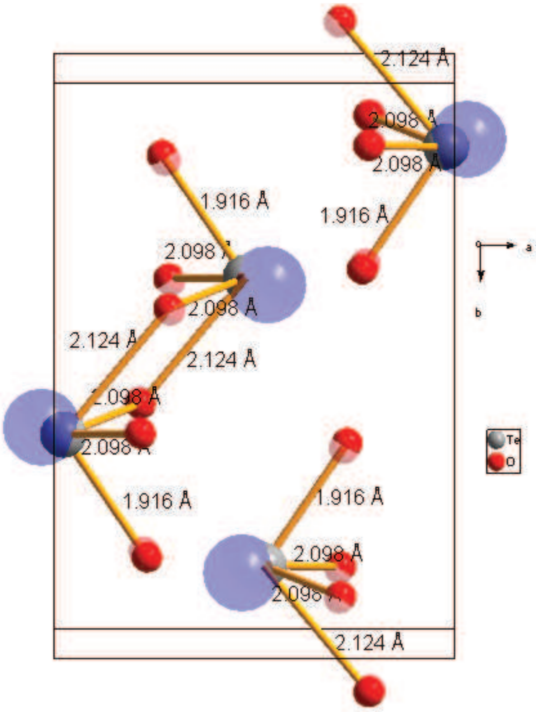

Figure 3.7: $\gamma-TeO_2$ structure modelled with core-shell model for Te atoms and Catlow potential for O–O interaction (see Table 3.3). The transparent spheres in blue represent the Te atoms shells and in red represent the O atoms shells.

Finally, as we discussed above, the addition of a quartic term to the core-shell interaction potential improves the IAPs transferability and helps to optimise the M_2TeO_3 (M = Li, Na, K, Cs) structures. Fig. 3.3 reports the Cs_2TeO_3 structures before introducing the k_4^{cs} term (left) and after (right) as an example. At the same time, it has no significant influence on the structures that were well modelled with only harmonic spring potential. The final parameters for derived IAPs are listed in Table 3.5.

Table 3.4: Parameters for Buckingham potential for Te^{4+}–O^{2-} and new O^{2-}–O^{2-} interaction and for core-shell model with harmonic spring potential for both Te and O atoms.

Buckingham potential

	A, eV	ρ, Å	C, eVÅ^6
Te_c^{4+}–O_{sh}^{2-}	1595.266748	0.345867	1.0
O_{sh}^{2-}–O_{sh}^{2-}	82970.688434	0.16099	31.361954

Shell model

	k_2^{cs}, eVÅ^{-2}	q_s, e
Te^{4+}	35.736418	-1.975415
O^{2-}	61.776616	-3.122581

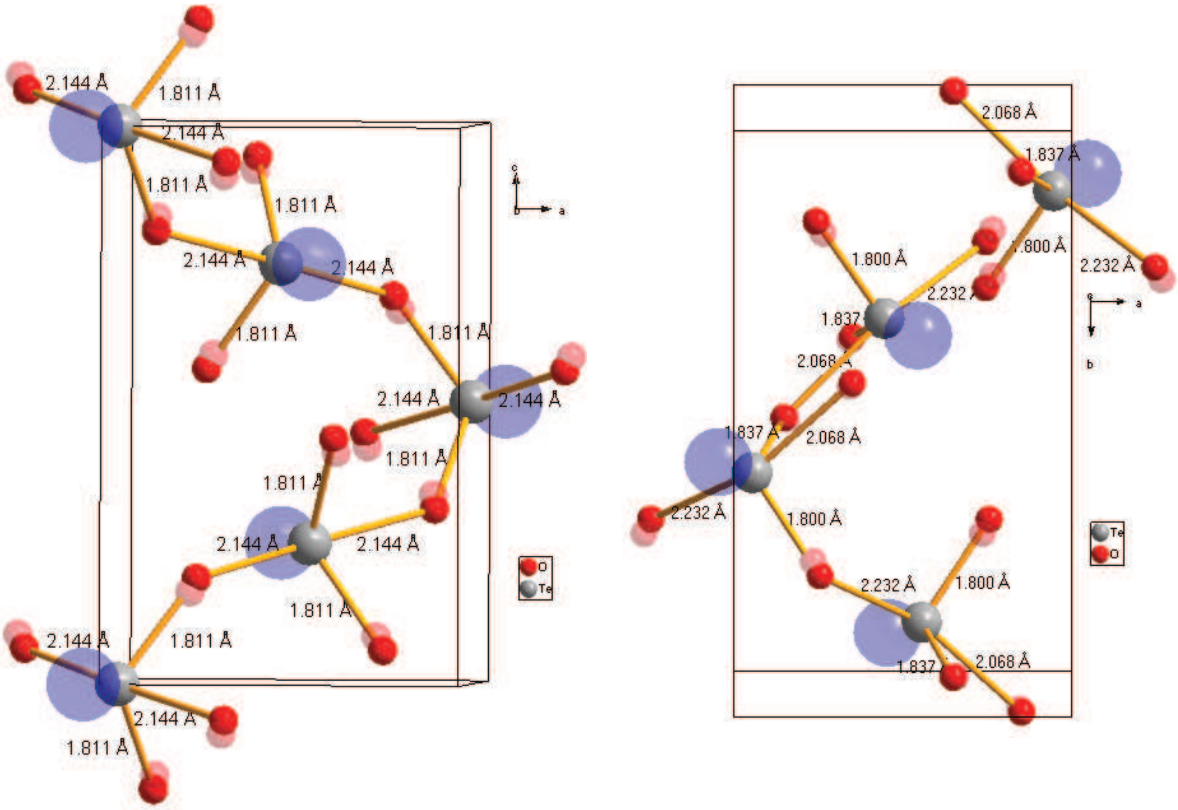

Figure 3.8: α–TeO_2 (left) and γ–TeO_2 (right) structures modelled with core-shell model for Te atoms and modified potential for O–O interaction (see Table 3.4). The transparent spheres in blue represent the Te atoms shells and in red represent the O atoms shells.

Table 3.5: Parameters for Buckingham potential for Te^{4+}–O^{2-} and O^{2-}–O^{2-} interaction and for shell model for both Te (anharmonic spring potential) and O atoms.

Buckingham potential

	A, eV	ρ, Å	C, eVÅ^6
Te_c^{4+}–O_{sh}^{2-}	1595.266748	0.345867	1.0
O_{sh}^{2-}–O_{sh}^{2-}	82970.688434	0.16099	31.361954

Shell model

	k_2^{cs}, eVÅ^{-2}	k_4^{cs}, eVÅ^{-4}	q_s, e
Te^{4+}	35.736418	90.0	-1.975415
O^{2-}	61.776616	0.0	-3.122581

Table 3.6: Characteristics for Cs_2TeO_3 structure modelled with different spring values for Te atoms core-shell model. The other IAPs parameters are from Table 3.5. The errors in percents with respect to experimental values are indicated in brackets.

Parameter, Å	k_2^{cs}, eVÅ^{-2}	42.259877*	46.123789	35.736418
	k_4^{cs}, eVÅ^{-4}	0	0	90
a, b		7.251(-6.79)	6.887 (-1.43)	6.911 (-1.78)
c		6.490 (18.59)	7.920 (0.65)	7.802 (2.14)
Te–O bond length		1.825 (1.14)	1.834 (0.65)	1.827 (1.03)
Te (c)–Te (sh) distance		1.1	0.669	0.719

**We give an example of failed modelling with this spring value, as using k_2^{cs} = 35.736418 eVÅ^{-2} leads to abortion of the program, so that it does not provide an output file with final configuration.*

Table 3.7: Cell parameters for $\alpha-TeO_2$ and $\gamma-TeO_2$ structures modelled with different IAPs from Tables 3.3, 3.4 and 3.5. The error in percents with respect to experimental values are indicated in the brackets.

Parameter, Å	IAP from Table 3.3	IAP from Table 3.4	IAP from Table 3.5
$\alpha-\mathbf{TeO_2}$			
a, b	4.656 (3.20)	4.847 (-0.77)	4.831 (-0.44)
c	7.103 (6.70)	7.546 (0.88)	7.349 (3.46)
$\gamma-\mathbf{TeO_2}$			
a	5.149 (5.13)	4.929 (-0.65)	5.084 (-3.79)
b	7.458 (13.04)	8.641 (-0.76)	8.312 (3.08)
c	3.673 (15.59)	4.286 (1.49)	4.196 (3.55)

3.2 Results and discussion

Several relatively simple ternary TeO_2-based systems were investigated. They represent all various Te^{IV} atom environments: TeO_3 units in M_2TeO_3 (M = Li, Na, K, Cs) and $MgTe_2O_5$ compounds; TeO_{3+1} units in $\gamma-TeO_2$; TeO_4 units in $\alpha-$, $\beta-TeO_2$ and $CaTe_2O_5$; TeO_5 units in $Ag_2Te_4O_{11}$ ($Ag_2Te_2^{IV}Te_2^{VI}O_{11}$), $BaTe_2O_6$ ($BaTe^{IV}Te^{VI}O_6$), $K_2Te_4O_{12}$ ($K_2Te^{IV}Te_3^{VI}O_{12}$), $Na_2Te_4O_9$, $P_2Te_3O_{11}$ and $SrTe_3O_8$ ($SrTe_2^{IV}Te^{VI}O_8$) compounds; TeO_6 units in $Cs_2Te_4O_{12}$ ($Cs_2Te^{IV}Te_3^{VI}O_{12}$); and combinations of TeO_3, TeO_4 and TeO_5 units in $Bi_2Te_4O_{11}$, $Co_6Te_5O_{16}$ and $NiTe_2O_5$ compounds. The references on the experimental structural data for these compounds are listed in Table 3.8.

Table 3.8: Pure and mixed tellurite compositions optimised with derived potential

Structural unit	Compound	Reference	Space group
TeO_3	Cs_2TeO_3	[46]	P 3 2 1
	Li_2TeO_3	[91]	C 1 2/C 1
	K_2TeO_3	[92]	P -3
	Na_2TeO_3	[93]	P 1 21/A 1
	$MgTe_2O_5$	[94]	P B C N
TeO_{3+1}	γ-TeO_2	[8]	P 21 21 21
TeO_4	α-TeO_2	[4]	P 43 21 2
	β-TeO_2	[6]	P B C A
	$CaTe_2O_5$	[95]	P 1 21/C 1'
TeO_5	$BaTe_2O_6$	[96]	C M C M
	$Na_2Te_4O_9$	[97]	P -1
	$Ag_2Te_4O_{11}$	[98]	P -1
	$SrTe_3O_8$	[99]	P 42/M
	$K_2Te_4O_{12}$	[100]	C 2/M
	$P_2Te_3O_{11}$	[101]	P 1 21/C 1
TeO_6	$Cs_2Te_4O_{12}$	[102]	R -3 M
TeO_3, TeO_4, TeO_5	$Bi_2Te_4O_{11}$	[103]	P 1 21/N 1
	$Co_6Te_5O_{16}$	[104]	P N M A
	$NiTe_2O_5$	[105]	P N M A

The Buckingham and core-shell potentials parameters used for other cation-oxygen interactions are reported in Table 3.9. They were transferred from previous studies of binary oxides [106, 107, 37]. The comparison between calculated and experimental lattice parameters is reported in Table 3.10.

In general, there is a good agreement between calculated and experimental structures. The errors in cell parameters do not exceed 5% and all various of TeO_x structural units are well represented. We list the Te–O bond lengths and angles for all investigated structures in Table 3.11. One can point out that the general feature of the derived potentials is an

Table 3.9: Buckingham IAP and shell model parameters used for optimised structures

Buckingham potential

Interaction	A, eV	ρ, Å	C, eVÅ^6	Reference
Ag^{1+}–O^{2-}	962.197	0.3	0.0	[106]
Ba^{2+}–O^{2-}	4818.416	0.3067	0.0	[107]
Bi^{+3}–O^{2-}	49529.35	0.2223	0.0	[108]
Ca^{2+}–O^{2-}	2272.741	0;2986	0.0	[107]
Cs^{1+}–O^{2-}	4013.582581	0.318831	0.0	this work
Co^{2+}–O^{2-}	778.020	0.3301	0.0	[41]
K^{1+}–O^{2-}	3587.570	0.3	0.0	[107]
Li^{1+}–O^{2-}	426.480	0.3	0.0	[107]
Mg^{2+}–O^{2-}	946.627	0.31813	0.0	[37]
Na^{1+}–O^{2-}	1271.504	0.3	0.0	[107]
Ni^{2+}–O^{2-}	1582.500	0.28820	0.0	[37]
Sr^{2+}–O^{2-}	1956.702	0.3252	0.0	[107]
Te^{6+}–O^{2-}	2296.526581	0.333786	1.0	this work
P^{5+}–O^{2-}	1273.42017	0.32272	0.0	[109]

Shell model	k_2^{cs}, eVÅ^{-2}	q_s, e	Reference
Ba^{2+}	34.05	1.831	[107]
Bi^{+3}	359.55	-5.51	[108]
Ca^{2+}	34.05	1.281	[107]
Ni^{2+}	93.70	3.344	[37]
Sr^{2+}	21.53	1.831	[107]

underestimation of short Te–O bond lengths and a slight overestimation of intermediate Te–O bond lengths. In Table 3.11 we list the total bond-valences for each Te atom site calculated with Brown and Altermatt formulae [110] as well. As we can see, calculated values for optimised structures are overestimated because of the important contribution of the short bonds into the total atom bond-valence.

In Table 3.11 we give the values of Te core-shell distances as well. They vary in the range from 0.394 Å for one of the tellurium (IV) sites in $P_2Te_3O_{11}$ to 0.719 Å in Cs_2TeO_3. These distances are quite significant and much larger than those found for other cations with lone pairs (for example, 0.125 Å for Pb^{2+} cations in several Aurivillius-type structures [111]). Thereby Te^{IV} atom polarizes strongly in all investigated structures except in $Cs_2Te_4O_{12}$, where the core-shell distance is zero, which confirms that Te^{IV} LP does not present any stereochemical activity in this environment.

The localisation of Te electronic LP was studied experimentally in α-TeO_2 [4] and by *ab initio* methods in TeO_4H_4 and $TeO_3H_3^+$ molecules [112]. Both these works estimate the distance of the electronic LP at 0.6 Å from the Te atom core, which is in a good agreement with our results (0.504 Å for α-TeO_2 and 0.394–0.719 Å for the whole set of type of units). Average core-shell distance for the oxygen atoms is about 0.2 Å. In spite of much less significant core-shell distance for the oxygen atoms in comparison with tellurium atoms, it still remains very remarkable. This implies that oxygen polarisation effect strongly contributes to the forming of Te^{IV} atom coordination in TeO_2-based materials as well. This result confirms that it is necessary to explicitly include the polarisation effect of oxygen atoms for reliable empirical modelling of TeO_2-based materials.

We have also calculated the elastic constants for all investigated structures and they are reported in Table 3.12. The experimental elastic constants data are difficult to obtain and they do not exist in literature for most of the investigated structures. Nevertheless the values calculated with our model are physically realistic and all the eigenvalues of the elastic constants matrices are positive. The experimental elastic constants for α-TeO_2 [48] and those calculated by density functional theory (DFT) methods for γ-TeO_2 [49] are in good agreement with values obtained with our potentials.

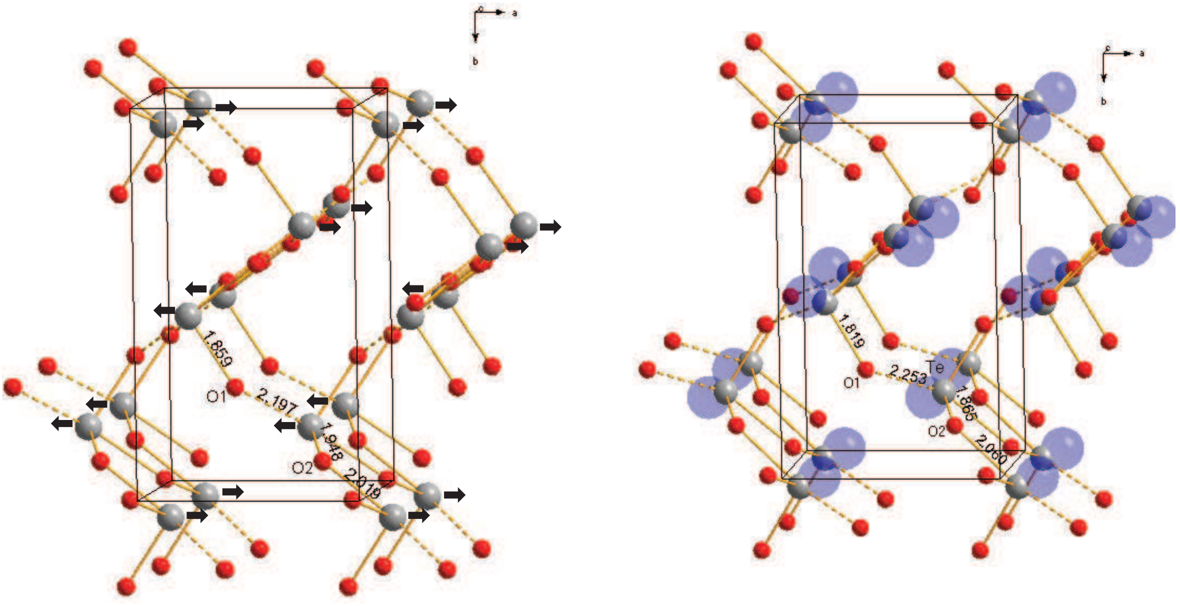

a)

b)

Figure 3.9: Spatial view of γ-TeO_2 structure: a) Experimental structure and b) Optimised structure. Solid lines represent the short and intermediate bonds (< 2.02 Å) and dashed lines represent the long bonds (> 2.02 Å). In a) the arrows indicate the direction of the Te LP and in b) the big blue spheres correspond to the Te shells. The bond lengths are in Å.

Let us now point out some subtle structural peculiarities of the γ-TeO_2 polymorph which we managed to reproduce using our IAP. This polymorph is especially interesting because in our research group it is considered the closest crystalline structure to glass.

Indeed, γ-TeO_2 polymorph crystallises first while heating the glass and the glass Raman spectra has much more common bands with γ-TeO_2 than with α-TeO_2 or β-TeO_2 polymorphs [8]. As was discussed above, γ-TeO_2 is constructed with TeO_{3+1} structural units with three short (< 2.02 Å) Te–O bonds and one elongated bond (2.197 Å), which form the three-dimensional network by sharing O_1 and O_2 corners (Fig. 3.9). Such a network forms wide rectangular tunnels containing the LPs of tellurium (IV) atoms [8].

Let us now compare the structure of the γ-TeO_2 with that of the paratellurite, α-TeO_2 (Fig.3.10). In both structures basic units are interconnected *via* Te–O–Te bridges. In α-TeO_2 there are only the essentially asymmetric bridges (1.880–2.121 Å), whereas in γ-TeO_2, the TeO_{3+1} units are alternately linked by nearly symmetric (1.948–2.019 Å) and highly asymmetric (1.859–2.197 Å) bridges. According to Champarnaud *et al.* the resemblance of Raman spectra of γ-TeO_2 and of glass comes from vibrations of symmetric Te–O–Te bridges; thus it appears that such bridges represent one of the main structural features of TeO_2 glasses. Although the errors in bond lengths exaggerate a bit the subtle difference in symmetric and asymmetric bridges in optimised structures, our IAP model has a critical ability for distinction between TeO_4 and TeO_{3+1} units for further successful application of the IAPs to glass simulation.

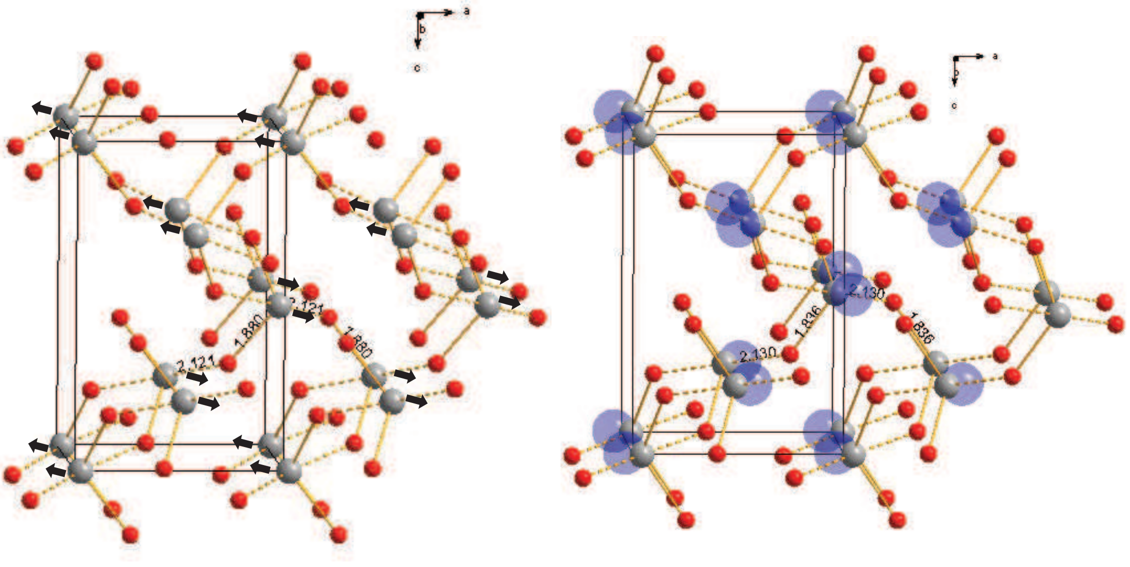

a) b)

Figure 3.10: Spatial view of α-TeO_2 structure: a) Experimental structure and b) Optimised structure. Solid lines represent the short and intermediate bonds (< 2.02 Å) and dashed lines represent the long bonds (> 2.02 Å). In a) the arrows indicate the direction of the Te LP and in b) the big blue spheres correspond to the Te shells. The bond lengths are in Å.

Among all the investigated structures there are two structures that we did not manage to optimise: K_2TeO_3 and $K_2Te_4O_{12}$. In the first case, as was discussed above, the optimisation was not successful even with improved Te core-shell anharmonic potential. In $K_2Te_4O_{12}$ case, a different problem occurred. In spite of a good agreement in cell parameters the local environment of Te^{IV} atom was incorrect. It represents a perfect TeO_6 octahedron completely similar to $Cs_2Te_4O_{12}$, whereas from experimental structural data it is a TeO_5 structural unit. The additional experimental data (elastic constants, etc.) could have helped to resolve this problem, but unfortunately we did not find any works on $K_2Te_4O_{12}$ compound except the first article on its synthesis and structure refinement [100] in 1978.

3.3 Conclusion

We derived the set of interatomic potentials for Te^{4+}–O^{2-} and O^{2-}–O^{2-} interactions which represent the structures of all known pure TeO_2 polymorphs and a set of mixed TeO_2-based compositions. All the cell parameters and bond lengths are reproduced with errors less than 5%. Generally our potentials underestimate short Te–O bonds and overestimate intermediate bonds. Our potentials are able to model all various TeO_x structural units found in investigated structures and to reflect the difference between TeO_4 unit with two short and two intermediate bonds and TeO_{3+1} unit with three short and one intermediate bonds. We found some difficulties in representing K_2TeO_3 and $K_2Te_4O_{12}$ structures, which seem to be rather particular. Our model does not manage to reproduce some subtle structural features in these phases, which would call for further studies.

Tellurium and oxygen electronic LPs are represented with a core-shell model. The short-range interaction set between Te core and O shell and the anharmonic spring potential is used for Te core-shell interaction. The tellurium atoms core-shell distance of 0.394–0.719 Å for different unit types is much larger than found in the literature for other atoms with electronic LPs and in a good agreement with values obtained by other methods. Oxygen atoms are also strongly polarised in all studied structures and their polarisation effect plays an important role in forming asymmetrical TeO_x units.

Table 3.10: Calculated and experimental lattice parameters for investigated structures

Parameter	Exp.	Calc.	Difference, %
$Ag_2Te_4O_{11}$			
a, Å	7.287	7.201	1.19
b, Å	7.388	7.304	1.14
c, Å	9.686	9.619	0.69
$Volume$, Å^3	521.459	505.884	2.99

Continued on next page

Table 3.10 – *Continued from previous page*

Parameter	Exp.	Calc.	Difference, %
α	95.67	95.82	-0.16
β	94.10	96.38	-2.42
γ	119.40	119.50	-0.09
$BaTe_2O_6$			
a, Å	5.569	5.5378	0.56
b, Å	12.796	13.285	-3.82
c, Å	7.320	7.279	0.55
$Volume$, Å^3	521.629	535.589	-2.68
α, β, γ	90	90	0.0
$Bi_2Te_4O_{11}$			
a, Å	6.991	6.797	2.78
b, Å	7.959	7.836	1.55
c, Å	18.896	18.299	3.16
$Volume$, Å^3	1047.1526	973.246	7.06
α, γ	90	90	0.0
β	95.176	93.049	2.23
$CaTe_2O_5$			
a, Å	9.382	9.3755	0.07
b, Å	5.709	5.6792	0.53
c, Å	11.132	11.0546	0.70
$Volume$, Å^3	539.953	534.479	1.01
α, γ	90	90	0.0
β	115.109	114.764	0.30
$Co_6Te_5O_{16}$			
a, Å	11.032	11.146	-1.03
b, Å	10.295	10.188	1.04
c, Å	12.876	12.807	0.54
$Volume$, Å^3	1462.385	1454.209	0.56
α, β, γ	90	90	0.0
Cs_2TeO_3			
a, b, Å	6.790	6.911	-1.78
c, Å	7.972	7.802	2.14
$Volume$, Å^3	367.542	372.608	-1.38
α, β	90	90	0.0
γ	120	120	0.0

Continued on next page

Table 3.10 – *Continued from previous page*

Parameter	Exp.	Calc.	Difference, %
$Cs_2Te_4O_{12}$			
a, b, Å	7.279	7.234	0.61
c, Å	18.299	18.057	1.33
$Volume$, Å^3	839.614	818.386	2.53
α, β	90	90	0.0
γ	120	120	0.0
$K_2Te_4O_{12}$			
a, Å	12.360	12.452	-0.74
b, Å	7.248	7.189	0.81
c, Å	11.967	12.594	-5.24
$Volume$, Å^3	1032.171	1064.409	-3.12
α, γ	90	90	0.0
β	105.680	109.243	-3.37
Li_2TeO_3			
a, Å	5.069	4.847	4.37
b, Å	9.566	9.306	2.71
c, Å	13.727	13.798	-0.52
$Volume$, Å^3	662.669	616.464	6.97
α, γ	90	90	0.0
β	95.40	97.96	-2.68
$MgTe_2O_5$			
a, Å	7.239	7.258	-0.26
b, Å	10.658	10.614	0.42
c, Å	5.988	5.964	0.40
$Volume$, Å^3	462.000	459.433	0.56
α, β, γ	90	90	0.0
Na_2TeO_3			
a, Å	6.882	7.017	-1.96
b, Å	10.315	10.740	-4.12
c, Å	4.961	4.873	1.77
$Volume$, Å^3	352.171	367.247	-4.28
α, β	90	90	0.0
γ	91.66	91.9378	-0.30
$Na_2Te_4O_9$			
a, Å	7.336	7.486	-2.04

Continued on next page

Table 3.10 – *Continued from previous page*

Parameter	Exp.	Calc.	Difference, %
b, Å	10.449	10.750	-2.88
c, Å	6.876	6.849	0.40
$Volume$, Å^3	527.072	551.147	-4.57
α	90.11	89.66	0.50
β	110.95	111.95	-0.90
γ	69.52	69.47	0.07
$NiTe_2O_5$			
a, Å	8.868	8.448	4.74
b, Å	12.126	12.376	-2.06
c, Å	8.452	8.451	0.02
$Volume$, Å^3	908.872	883.505	2.79
α, β, γ	90	90	0.0
$P_2Te_3O_{11}$			
a, Å	12.375	11.895	3.88
b, Å	7.317	7.077	3.29
c, Å	9.834	9.738	0.98
$Volume$, Å^3	881.695	807.998	8.36
α, γ	90	90	0.0
β	98.04	99.69	-1.68
$SrTe_3O_8$			
a, b, Å	6.826	6.829	-0.06
c, Å	6.760	6.636	1.83
$Volume$, Å^3	314.964	309.557	1.72
α, β, γ	90	90	0.0
α-TeO_2			
a, b, Å	4.810	4.831	-0.44
c, Å	7.613	7.349	3.46
$Volume$, Å^3	176.135	171.548	2.60
α, β, γ	90	90	0.0
β-TeO_2			
a, Å	12.035	11.550	4.03
b, Å	5.464	5.473	-0.17
c, Å	5.607	5.549	1.03
$Volume$, Å^3	368.712	350.814	4.85
α, β, γ	90	90	0.0

Continued on next page

Table 3.10 – *Continued from previous page*

Parameter	Exp.	Calc.	Difference, %
γ-TeO$_2$			
a, Å	4.898	5.084	-3.79
b, Å	8.576	8.312	3.08
c, Å	4.351	4.196	3.55
$Volume$, Å^3	182.765	177.326	2.98
α, β, γ	90	90	0.0

Table 3.11: Bond lengths, angles (only for α, β, γ-TeO$_2$), bond-valences for each tellurium site and value of Te and O shells displacements (x_{Te} and x_O) according to corresponding cores for experimental and optimised structures

Bond	Exp., Å	Calc., Å	Diff., %	V^*_{exp}	V^*_{calc}	Diff., %	x_{Te}, Å	x^{**}_O, Å
$Ag_2Te_4O_{11}$								
Te(3)–O	2.094	2.062	1.53	4.17	4.54	8.84	0.472	0.189
Te(3)–O	2.044	2.006	1.86					
Te(3)–O	1.892	1.808	4.44					
Te(3)–O	2.087	2.092	-0.24					
Te(3)–O	2.130	2.154	-1.13					
Te(4)–O	2.000	1.953	2.35	3.93	4.17	-5.99	0.4638	
Te(4)–O	2.174	2.088	3.96					
Te(4)–O	2.092	2.160	-3.25					
Te(4)–O	2.311	2.391	-3.46					
Te(4)–O	1.878	1.823	2.93					
$BaTe_2O_6$								
Te–O$_{ax}$	2.126	2.092	1.58	4.13	4.47	-8.13	0.547	0.217
Te–O	1.830	1.792	2.08					
$Bi_2Te_4O_{11}$								
Te(1)–O	1.872	1.853	1.01	3.91	4.22	-7.79	0.543	0.169
Te(1)–O	1.876	1.856	1.07					
Te(1)–O	1.93	1.916	0.73					
Te(2)–O	1.895	1.866	1.53	3.96	4.23	-6.83	0.544	
Te(2)–O	2.498	2.519	-0.84					
Te(2)–O	1.972	1.943	1.47					
Te(2)–O	1.870	1.842	1.50					
Te(3)–O	2.284	2.352	-2.98	3.83	4.30	-12.24	0.559	
Te(3)–O	2.074	1.989	4.10					
Te(3)–O	1.899	1.832	3.53					
Te(3)–O	1.870	1.833	1.98					
Te(4)–O	1.955	1.903	2.66	4.07	4.28	-4.98	0.543	

Continued on next page

Table 3.11 – *Continued from previous page*

Bond	Exp., Å	Calc., Å	Diff., %	V^*_{exp}	V^*_{calc}	Diff., %	x_{Te}, Å	x^{**}_O, Å
Te(4)–O	1.848	1.846	0.11					
Te(4)–O	1.890	1.890	0.00					
Te(4)–O	2.408	2.539	-5.44					
$CaTe_2O_5$								
Te(1)–O	1.852	1.838	0.76	4.04	4.25	-5.19	0.609	0.204
Te(1)–O	1.832	1.815	0.93					
Te(1)–O	1.979	1.992	-0.66					
Te(1)–O	2.450	2.276	7.10					
Te(2)–O	2.009	1.949	2.99	4.01	4.15	-3.67	0.595	
Te(2)–O	1.853	1.833	1.08					
Te(2)–O	1.898	1.856	2.21					
Te(2)–O	2.179	2.310	-6.01					
$Co_6Te_5O_{16}$								
Te(1)–O	1.866	1.851	0.80	4.03	4.20	-4.17	0.629	0.181
Te(1)–O	1.886	1.874	0.64					
Te(1)–O	1.863	1.841	1.18					
Te(2)–O	1.904	1.884	1.05	4.03	4.20	-4.14	0.58	
Te(2)–O	1.904	1.884	1.05					
Te(2)–O	1.833	1.846	-0.71					
Te(3)–O	1.858	1.857	0.05	4.17	4.37	-4.69	0.604	
Te(3)–O	1.858	1.857	0.05					
Te(3)–O	1.894	1.848	2.43					
Te(4)–O	2.060	1.985	3.64	3.86	4.29	-10.94	0.624	
Te(4)–O	2.060	1.985	3.64					
Te(4)–O	1.921	1.875	2.39					
Te(4)–O	1.888	1.896	-0.42					
Cs_2TeO_3								
Te–O	1.846	1.827	1.03	3.97	4.15	-4.74	0.719	0.236
$Cs_2Te_4O_{12}$								
Te–O	2.112	2.084	1.33	4.15	4.44	-7.07	0.0	0.184
$K_2Te_4O_{12}$								
Te–O(5)	1.973	2.074	-5.12	3.64	4.55	-24.93	0.0	0.188
Te–O(5)	2.017	2.074	-2.83					
Te–O(5)	2.017	2.074	-2.83					
Te–O(5)	2.275	2.074	8.83					
Te–O(5)	2.275	2.074	8.83					
Te–O(5)	–	2.074	100					
Li_2TeO_3								
Te–O	1.848	1.838	0.54	3.72	4.14	-11.28	0.649	0.200
Te–O	1.929	1.843	4.45					
Te–O	1.871	1.842	1.55					
$MgTe_2O_5$								
Te–O	1.859	1.828	1.66	4.01	4.23	-5.46	0.5606	0.181

Continued on next page

Table 3.11 – *Continued from previous page*

Bond	Exp., Å	Calc., Å	Diff., %	V^*_{exp}	V^*_{calc}	Diff., %	x_{Te}, Å	x^{**}_O, Å
Te–O	1.990	1.982	0.40					
Te–O	1.850	1.832	0.97					
Te–O	2.405	2.366	1.62					
Na_2TeO_3								
Te–O	1.882	1.858	1.27	3.92	4.16	-6.13	0.648	0.214
Te–O	1.875	1.853	1.17					
Te–O	1.874	1.848	1.38					
$Na_2Te_4O_9$								
Te(1)–O	1.964	1.870	4.78	4.16	4.24	-2.05	0.5294	0.204
Te(1)–O	2.054	2.061	-0.34					
Te(1)–O	2.238	2.344	-4.73					
Te(1)–O	1.899	1.859	2.10					
Te(1)–O	2.146	2.255	-5.08					
Te(2)–O	2.450	2.502	-2.12	3.93	4.19	-6.84	0.575	
Te(2)–O	1.889	1.862	1.43					
Te(2)–O	1.919	1.863	2.92					
Te(2)–O	1.905	1.877	1.47					
Te(3)–O	1.823	1.809	0.76	3.85	4.09	-6.03	0.579	
Te(3)–O	2.013	2.09	-3.82					
Te(3)–O	1.934	1.845	4.60					
Te(3)–O	2.319	2.236	3.57					
Te(4)–O	1.902	1.871	1.63	4.01	4.20	-4.74	0.570	
Te(4)-O	2.119	2.060	2.78					
Te(4)–O	1.821	1.799	1.21					
Te(4)–O	2.123	2.176	-2.50					
$NiTe_2O_5$								
Te(1)–O	1.944	2.011	-3.45	3.96	4.25	-7.34	0.543	0.1828
Te(1)–O	1.863	1.817	2.47					
Te(1)–O	1.877	1.854	1.23					
Te(1)–O	2.472	2.302	6.88					
Te(2)–O	1.886	1.845	2.17	4.07	4.36	-6.98	0.539	
Te(2)–O	1.996	1.902	4.71					
Te(2)–O	1.996	1.902	4.71					
Te(2)–O	2.247	2.398	-6.72					
Te(2)–O	2.247	2.398	-6.72					
Te(3)–O	1.895	1.859	1.90	3.90	4.20	-7.55	0.563	
Te(3)–O	1.877	1.862	0.80					
Te(3)–O	1.877	1.862	0.80					
$P_2Te_3O_{11}$								
Te(1)–O	1.876	1.821	2.93	4.12	4.25	-3.05	0.394	0.254
Te(1)–O	2.080	2.066	0.67					
Te(1)–O	2.104	2.131	-1.28					
Te(1)–O	2.164	2.202	-1.76					

Continued on next page

Table 3.11 – *Continued from previous page*

Bond	Exp., Å	Calc., Å	Diff., %	V^*_{exp}	V^*_{calc}	Diff., %	x_{Te}, Å	x^{**}_O, Å
Te(1)–O	2.145	2.241	-4.48					
Te(2)–O	2.093	2.086	0.33	4.31	4.45	-3.41	0.406	
Te(2)–O	1.894	1.842	2.75					
Te(2)–O	1.973	1.977	-0.20					
Te(2)–O	2.090	2.101	-0.53					
Te(2)–O	2.202	2.259	-2.59					
Te(3)–O	2.485	2.603	-4.75	4.16	4.25	-2.02	0.461	
Te(3)–O	1.984	2.018	-1.71					
Te(3)–O	1.830	1.805	1.37					
Te(3)–O	1.956	1.948	0.41					
Te(3)–O	2.293	2.284	0.39					
$SrTe_3O_8$								
Te–O	1.917	1.901	0.83	4.07	4.31	-5.94	0.476	0.175
Te–O	2.083	2.065	0.86					
Te–O	2.212	2.153	2.66					
Te–O	2.075	2.061	0.67					
Te–O	1.908	1.962	-2.83					
Te–O	1.936	1.96	-1.24					
α-TeO_2								
Te–$O_{1,2}$	1.879	1.836	2.31	4.06	4.32	-6.39	0.504	0.182
Te–$O_{3,4}$	2.121	2.130	-0.42					
Angles, °								
O_1–Te–O_2	103.34	110.45	-6.87					
O_3–Te–O_4	167.94	174.49	-3.90					
β-TeO_2								
Te–O	1.877	1.836	2.34	3.93	4.20	-6.95	0.501	0.194
Te–O	1.927	1.886	2.28					
Te–O	2.070	2.025	2.17					
Te–O	2.196	2.299	-4.97					
γ-TeO_2								
Te–O_1	1.859	1.819	2.15	3.99	4.27	-7.20	0.525	0.199
Te–O_2	1.948	1.865	4.26					
Te–O_1^1	2.197	2.253	-2.55					
Te–O_1^2	2.019	2.06	-2.03					
Angles, °								
O_1–Te–O_2	99.13	102.18	-3.00					
O_1^1–Te–O_1^2	153.62	147.88	3.72					

**Bond-valences are calculated using re-determined bond-valence parameters for* $Te^{4+} - O^{2-}$*:* $r_0 = 1.9605, b = 0.41$ *[113] and neighbours out to 3.5 Å were included*

***Core/shell distances for O atoms are averaged over all oxygen sites in the structure*

Table 3.12: Calculated and experimental (if exist) elastic constants for investigated structures

C_{ij}, *GPa*	C_{11}	C_{12}	C_{13}	C_{14}	C_{15}	C_{16}
		C_{22}	C_{23}	C_{24}	C_{25}	C_{26}
			C_{33}	C_{34}	C_{35}	C_{36}
				C_{44}	C_{45}	C_{46}
					C_{55}	C_{56}
						C_{66}
Compound						
$Ag_2Te_4O_{11}$						
	254.03	87.62	26.45	-4.39	-13.62	1.17
		259.29	18.43	-1.49	-6.49	-12.01
			175.74	-18.35	-9.77	4.64
				35.29	-9.56	0.15
					30.97	0.33
						88.90
$BaTe_2O_6$						
	276.45	46.03	103.62	0.00	0.00	0.00
		104.45	40.83	0.00	0.00	0.00
			276.94	0.00	0.00	0.00
				29.73	0.00	0.00
					5.15	0.00
						20.34
$Bi_2Te_4O_{11}$						
	133.01	36.19	35.74	0.00	2.89	0.00
		120.03	40.18	0.00	-19.44	0.00
			139.77	0.00	-7.35	0.00
				50.51	0.00	-7.97
					45.37	0.00
						77.32
$CaTe_2O_5$						
	69.86	6.03	26.03	0.00	-9.24	0.00
		62.15	12.57	0.00	-4.79	0.00
			65.68	0.00	-16.83	0.00
				16.31	0.00	-2.36
					26.09	0.00
						9.43
$Co_6Te_5O_{16}$						
	133.73	52.13	29.96	0.00	0.00	0.00
		144.96	26.72	0.00	0.00	0.00
			113.25	0.00	0.00	0.00
				21.45	0.00	0.00
					33.53	0.00
						33.32

Continued on next page

Table 3.12 – *Continued from previous page*

C_{ij}, *GPa*	C_{11}	C_{12}	C_{13}	C_{14}	C_{15}	C_{16}
		C_{22}	C_{23}	C_{24}	C_{25}	C_{26}
			C_{33}	C_{34}	C_{35}	C_{36}
				C_{44}	C_{45}	C_{46}
					C_{55}	C_{56}
						C_{66}
Compound						
Cs_2TeO_3						
	45.32	18.44	12.04	1.70	0.00	0.00
		45.32	12.04	-1.70	0.00	0.00
			16.62	0.00	0.00	0.00
				4.96	0.00	0.00
					4.96	1.70
						13.44
$Cs_2Te_4O_{12}$						
	303.80	114.48	96.84	9.09	0.00	0.00
		303.80	96.84	-9.09	0.00	0.00
			275.12	0.00	0.00	0.00
				76.38	0.00	0.00
					76.38	9.09
						94.66
$K_2Te_4O_{12}$						
	303.14	109.96	86.97	0.00	12.24	0.00
		301.07	89.12	0.00	-15.83	0.00
			263.99	0.00	1.31	0.00
				72.75	0.00	-15.84
					70.59	0.00
						93.79
Li_2TeO_3						
	42.45	38.61	4.92	0.00	0.62	0.00
		111.35	7.72	0.00	-3.29	0.00
			19.07	0.00	-1.98	0.00
				9.25	0.00	-2.69
					24.91	0.00
						41.28
$MgTe_2O_5$						
	114.47	40.55	56.87	0.00	0.00	0.00
		117.20	41.19	0.00	0.00	0.00
			98.39	0.00	0.00	0.00
				28.04	0.00	0.00
					61.97	0.00
						42.21
Na_2TeO_3						
	67.04	-3.17	27.14	0.00	-9.29	0.00

Continued on next page

Table 3.12 – *Continued from previous page*

C_{ij}, *GPa*	C_{11}	C_{12}	C_{13}	C_{14}	C_{15}	C_{16}
		C_{22}	C_{23}	C_{24}	C_{25}	C_{26}
			C_{33}	C_{34}	C_{35}	C_{36}
				C_{44}	C_{45}	C_{46}
					C_{55}	C_{56}
						C_{66}
Compound						
		78.22	30.17	0.00	0.99	0.00
			63.11	0.00	-8.56	0.00
				34.03	0.00	-3.87
					32.83	0.00
						11.74
$Na_2Te_4O_9$						
	52.47	16.74	27.25	-5.31	-15.51	12.62
		51.05	12.66	-2.31	-3.41	14.41
			94.44	6.59	-26.35	0.92
				16.49	-1.57	-10.84
					21.41	-2.44
						20.78
$NiTe_2O_5$						
	77.75	46.76	52.41	0.00	0.00	0.00
		129.04	38.49	0.00	0.00	0.00
			93.66	0.00	0.00	0.00
				55.41	0.00	0.00
					39.32	0.00
						44.92
$P_2Te_3O_{11}$						
	89.35	20.59	30.99	0.00	-12.84	0.00
		74.39	8.55	0.00	-7.09	0.00
			81.96	0.00	6.34	0.00
				21.40	0.00	-7.39
					46.67	0.00
						24.09
$SrTe_3O_8$						
	133.62	68.29	47.39	0.00	0.00	7.77
		133.62	47.39	0.00	0.00	-7.77
			354.17	0.00	0.00	0.00
				25.39	0.00	0.00
					25.39	0.00
						62.59
α-TeO_2						
	62.1982	41.0189	19.1431	0.0000	0.0000	0.0000
		62.1982	19.1431	0.0000	0.0000	0.0000
			132.9107	0.0000	0.0000	0.0000

Continued on next page

Table 3.12 – *Continued from previous page*

C_{ij}, *GPa*	C_{11}	C_{12}	C_{13}	C_{14}	C_{15}	C_{16}
		C_{22}	C_{23}	C_{24}	C_{25}	C_{26}
			C_{33}	C_{34}	C_{35}	C_{36}
				C_{44}	C_{45}	C_{46}
					C_{55}	C_{56}
						C_{66}
Compound						
				43.4442	0.0000	0.0000
					43.4442	0.0000
						80.4861
Exp.*						
	59.5	55.1	24.7	0.0000	0.0000	0.0000
		59.5	24.7	0.0000	0.0000	0.0000
			115.6	0.0000	0.0000	0.0000
				26.9	0.0000	0.0000
					26.9	0.0000
						72.9
β-TeO_2						
	47.8665	16.9458	14.2551	0.0000	0.0000	0.0000
		71.3909	35.1699	0.0000	0.0000	0.0000
			129.5418	0.0000	0.0000	0.0000
				49.8254	0.0000	0.0000
					31.5029	0.0000
						26.0381
γ-TeO_2						
	52.1588	15.9202	10.4847	0.0000	0.0000	0.0000
		42.2653	2.6836	0.0000	0.0000	0.0000
			65.4133	0.0000	0.0000	0.0000
				40.0072	0.0000	0.0000
					32.4874	0.0000
						48.1753
Calc. (DFT)**						
	66.42	38.36	18.3	0.0000	0.0000	0.0000
		51.95	17.45	0.0000	0.0000	0.0000
			67.43	0.0000	0.0000	0.0000
				37.03	0.0000	0.0000
					32.34	0.0000
						51.67

* *Reference* [48]

***Reference* [49]

Chapter 4

Structure of the pure TeO_2 glass and δ–TeO_2 polymorph

In this chapter we perform the classical MD simulations of pure TeO_2 glass structure and δ–TeO_2 polymorph. To this end we use the MD methods described in Section 1.2.2 of Chapter 1 and the IAPs derived in the previous chapter. We also use the experimental techniques described in Section 1.3 of Chapter 1 in order to obtain the PDF for δ–TeO_2 polymorph. We analyse the modelled structures with the help of PDFs and in terms of bond angle distribution (BAD), structural units distribution, rings distribution, etc.

4.1 Classical Molecular Dynamics Simulations of the pure TeO_2 glass structure

4.1.1 Computational details

The glass model in MD simulations should be normally prepared as much as possible like the real glass, *i.e.* the initial configuration is firstly heated and then cooled down to room temperature with an appropriate cooling rate. The ideal way of creating the glass model is a slow continuous cooling of the system from the melting temperature T_m to glass formation temperature T_g. Undoubtedly, classical MD has the advantage over *ab initio* MD in terms of simulation times but even though we are still limited from a technical point of view. Particularly, the use of the relaxation algorithm for the core-shell model is especially time-consuming and hardly possible at high temperatures. Technically it means that frequent and random abortions of a simulation job occurred because of convergence problem in the shell relaxation algorithm in DL_POLY, when the shell model was "turned on" for all types of atoms. For this reason, we had to simplify the model during the quenching procedure and we used the rigid-ion model for only one atom type while cooling the system.

Using the simplified model, we managed to perform a continuous simulation job. We preferred to use the core-shell model for tellurium atoms as their polarisation effect has a stronger influence in TeO_2 system. However, the use of shell-model MD for tellurium atoms required some technical "tricks". As we discussed in the previous chapter, the distances between Te core and Te shell are very significant (up to 0.719 Å), which could provoke the mentioned above technical difficulties.

Let us now consider some tips, which we used to overcome the mentioned technical problems. Normally, one does an equilibration run before MD production. It allows the system to move in the phase-space from arbitrarily assigned initial conditions to the region of equilibrium states [53]. However, for the new simulation runs (*i.e.* they are not continuation of previous ones by restarting) the shells are moved on to the top of their respective cores in DL_POLY . As the shells displacements in our system are very large, this could prevent the shell relaxation algorithm to converge, because the positions "on the core" are not natural in tellurites case. To bypass this we did no equilibration steps in simulation jobs, but in the meantime we used reasonable initial conditions and sufficiently long simulation times.

The other useful feature, which helped to perform the continuous job, is the `rlxtol` parameter in the CONTROL file. It resets the force tolerance for the shell relaxation to a given value. This parameter was increased up to 10 (in DL_POLY units) at the high temperatures. Sometimes the forces on shells were manually set to zero in output configuration file (REVCON) when job aborted, and the run was restarted with manually relaxed shells.

Nevertheless, the test runs showed that the use of polarisable potential for oxygen atoms at 300 K is necessary even if no diffusion is expected to occur at this temperature. Indeed, let us compare two total PDFs in Fig. 4.1. PDF presented with dash-dotted line is calculated for the glass model obtained using rigid-ion oxygen atoms. Further this model was treated at 300K with the core-shell model for oxygen atoms. The corresponding PDF is presented with solid line. It is clear that the inclusion of the shell model even at 300 K improved significantly the short- and medium-range order in the modelled glass structure.

4.1.2 Glass preparation

The final model of the pure TeO_2 glass was obtained starting from the draft glass model obtained after test runs. The simulation box (31.76 Å×34.62 Å×30.58 Å) contained 4032 particles (= 2016 cores and 2016 shells). We used the NPT ensemble and a time step of 1.0 fs for integration of the equations of motion. Firstly, the system was heated up to 2050 K (the γ-TeO_2 melting temperature according to the test runs) and kept for about 150 ps

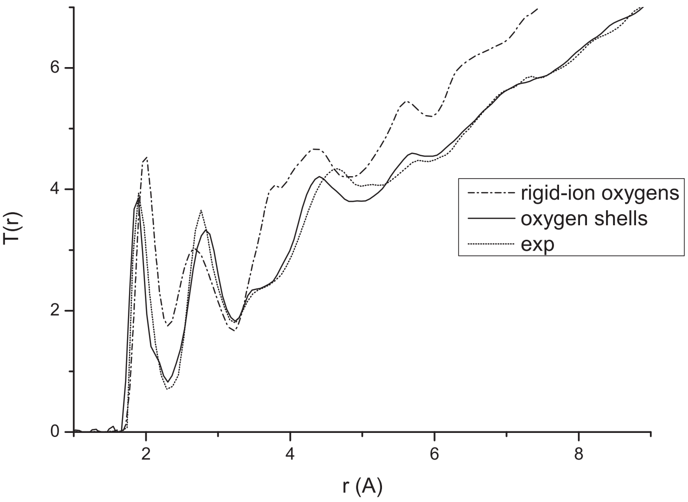

Figure 4.1: Total PDFs for the glass at 300K modelled in the rigid-ion framework (dash-dotted line) and in the core-shell model (solid line) for oxygen atoms, and an experimental total PDF.

following which it was cooled down to 1000 K and kept for about 70 ps more, and after it was cooled down to 500 K and kept at this temperature for about 70 ps more. Then, the system was cooled down to 300 K and kept at this temperature for about 50 ps. The final configuration was obtained by annealing the system at 300 K during about 20 ps with the full shell model, *i.e.* with harmonic spring potential interaction for O(core)–O(shell) system and quartic spring potential interaction for Te(core)–Te(shell) system. The fact that the shell model for oxygen atoms was not activated when the atomic diffusion is high may induce defects in the medium range-order of the glass model (as discussed in Sec. 4.1.4.1). The temperature variation as a function of time is shown in Fig. 4.2 and corresponds to $5.4 \cdot 10^{12}$ K/s cooling rate in average. The final atomic density of the modelled glass structure is 0.0626 at/$\AA^3$.

One can argue that, in fact, our system was cooled down with infinite rate between 2050 K and 1000 K within the reported preparation procedure. It is possible that T_g for the modelled glass lies above 1000 K, thus the structural relaxation is expected to be incomplete and the resulting structure contains more defects than a fully relaxed glass model. Effectively, the step-wise cooling within this temperature region seems to be more reasonable, however the choice of the infinite cooling rate is due to some peculiarities of using the rigid-ion model for oxygen atoms. In fact, we tried to decrease very slowly the temperature of the melt, as shown in Fig. 4.3. This quenching procedure lead to rather unusual and interesting results, which would call for a deeper investigation.

Indeed, already at a high temperature (1800 K) we remarked the beginning of

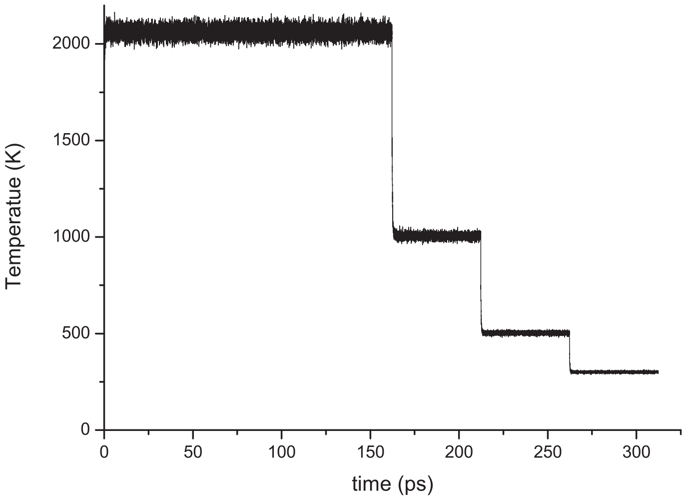

Figure 4.2: Temperature as a function of time in the TeO_2 glass preparation procedure.

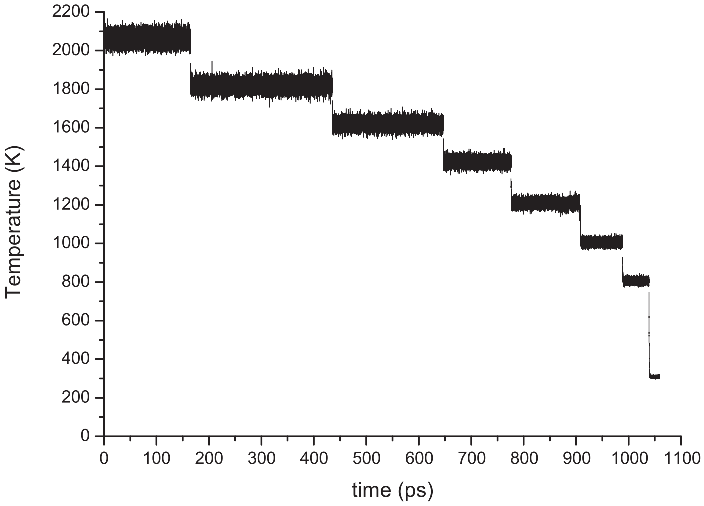

Figure 4.3: Temperature as a function of time in the test TeO_2 glass preparation procedure.

a crystallisation of a small germ in our system. (We recall here that the starting configuration was a disordered system, which did not have any "memory" of the crystalline state.) Fig. 4.4 shows an intermediate configuration at T = 1200 K, where we can see the layers of Te atoms forming into a crystalline lattice. The partial PDFs corresponding to this configuration are reported in Fig. 4.5. One can remark that Te–Te partial PDF looks like the one for FCC lattice with the cell parameter $a = 5.22$ Å. The Fig. 4.6 reports the evaluation of total distribution function with temperature during slow cooling. As we can see, the peaks become thinner and more pronounced, which indicates the ordering of the germ. That is why we preferred a long annealing at T = 2050 K and an immediate cooling down to T = 1000 K in order to avoid any nucleation of crystalline germs in our system.

It is also interesting to note that traces of crystallised germ disappeared when the oxygen shells were "turned on" at T = 300 K so that the final total PDF became alike to that one of the final glass configuration, but with final atomic density of 0.0635 at/Å^3

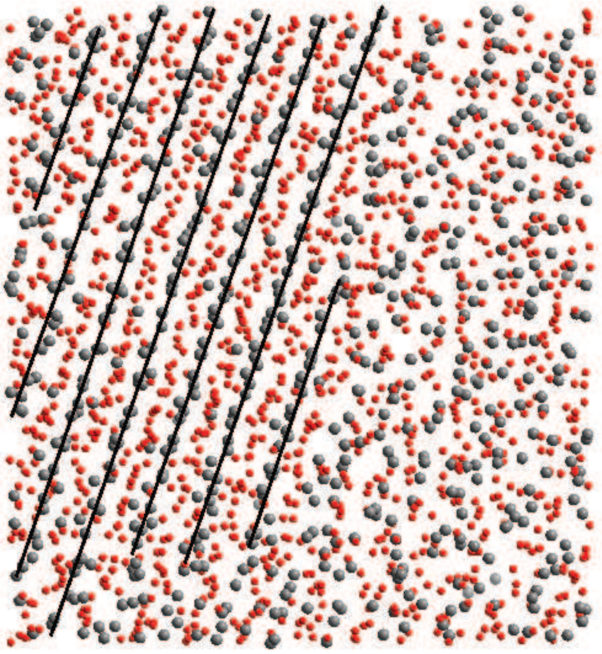

Figure 4.4: Projection of a configuration at T = 1200 K in the slow cooling procedure. The tellurium atoms are represented in grey and the oxygen atoms are represented in red. The black lines are the guides for an eye.

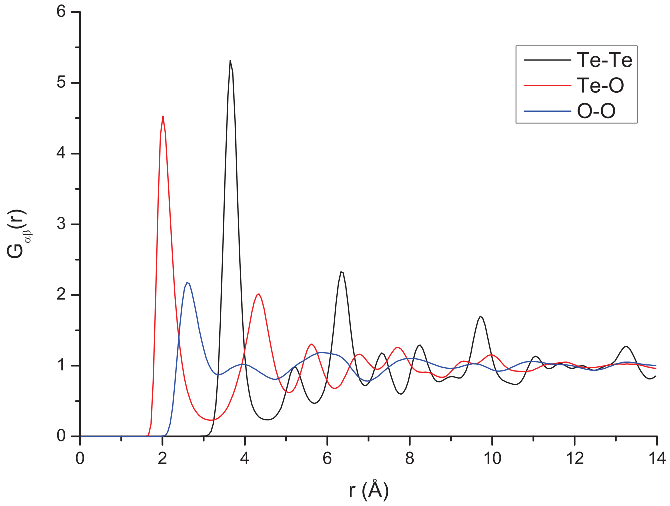

Figure 4.5: Partial PDFs for intermediate configuration at T = 1200 K.

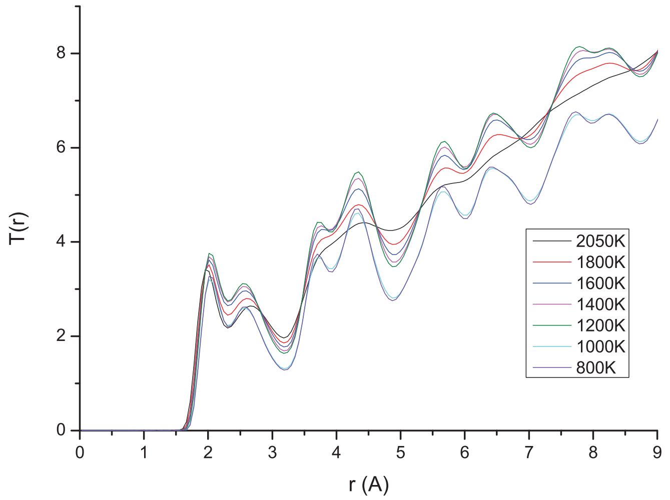

Figure 4.6: Total PDFs for different temperatures during the slow cooling procedure.

4.1.3 Experimental PDF

The synthesis of the TeO_2 glass sample and the obtaining of its PDF were performed several years ago in the laboratory. The pure TeO_2 glass sample was synthesised starting from orthotelluric acid H_6TeO_6 (Aldrich 99.9%). Orthotelluric acid was first thermally decomposed at 550°C for 24 hours in order to obtain powdered $\alpha-TeO_2$. The powder was then put in a platinum crucible and melted at 800°C for 30 minutes and finally quenched using a mixture of water, NaCl and ethanol at about -10 °C. As only a small quantity of glass (few decigrams) was obtained after each synthesis, this procedure was repeated in order to obtain a few grams. The measured density of the sample is $\rho_{exp} = 5.57$ g/cm^3, which corresponds to a atomic density 0.063 at/Å^3.

The experimental PDF was obtained thanks to a neutron total scattering experiment carried out at the 7C2 diffractometer of the LLB (Laboratoire Lèon Brillouin), Saclay, France. The used wavelength of 0.701 Å enabled us to record intensities up to Q_{max} = 16Å^{-1} ($Q = 4\pi sin\theta/\lambda$). The powder samples were placed in a thin-walled (2.5 micrometers) vanadium container of 6 mm in diameter. The experiment was performed under vacuum at room temperatures. Raw data were corrected for empty cell, absorption, inelastic and multiple scattering and normalised using the program CORRECT [114]. The total PDF was then derived from the structure factor using the MCGR program [115]. This Monte Carlo-based inversion method allows in contrast to the conventional direct Fourier transform, to correctly handle noise, truncation of data and the finite resolution of the instrument.

4.1.4 Results

4.1.4.1 Pair distribution functions

In Fig. 4.7 we report the calculated total distribution function $T(r)$ together with the experimental one. Without going into the details, let us precise that the simulated $T(r)$ was slightly broadened to take into account the effect of truncation of the experimental data at Q_{max}. For this, we first calculated the Fourier transform of $T(r)$, then we multiplied by a function $e^{-\alpha Q^2}$ and finally Fourier transform again to obtain the smeared $T(r)$ corresponding to experiment. Note that only the first peaks of $T(r)$ are affected by this broadening. The envelope of calculated $T(r)$ is in good agreement with the experimental one, which lets us conclude that the modelled glass structure is consistent with the real one. The first peak of the calculated $T(r)$ corresponds to the shortest Te–O distances and is slightly shifted to smaller r values with respect to the experimental data. This is in accordance with the underestimation of the Te–O bond lengths found using the crystalline structures optimised with our IAPs . Also it shows a more explicit shoulder at

≈ 2.13 Å than the experimental $T(r)$, which is attributed to elongated axial Te–O bonds. The second peak shows a more significant inaccuracy in calculated $T(r)$. This peak has the main contribution from the O–O partial distribution function (see Fig. 4.8) and is shifted to the larger r values (2.83 Å) with respect to the experimental one (2.77 Å). It implies that in our model the O–O distances are slightly exaggerated, but this does not affect either Te atom coordination or TeO_x units interconnection. The third peak at 3.47 Å is very representative for TeO_x units interconnections, as it corresponds to the shortest Te–Te distances, and it fits very well the experimental data. The most important disagreement between calculated and experimental $T(r)$ is in the fourth peak position. The calculated value is 4.40 Å and corresponding experimental value is 4.67 Å. As seen in Fig. 4.8, all three partial PDFs contribute to this peak to a large extent, so that it is difficult to define the origin of this error. Possibly, this error is due to the use of the rigid-ion model for oxygen atoms during the quenching process.

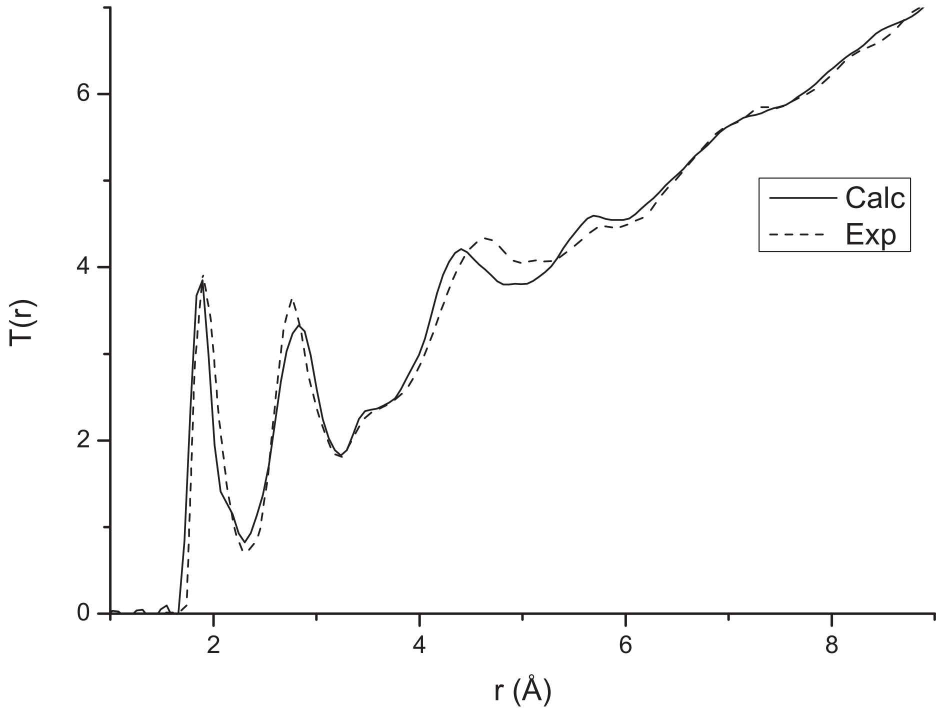

Figure 4.7: Total distribution function obtained with MD simulations (solid line) compared with the neutron diffraction data (dotted line).

Fig. 4.8 shows all the partial PDFs, which have no oscillations in the region for $r > 9$ Å. This indicates an appropriate choice of the simulation box size. The Te–O partial PDF has a sharp first peak with the maximum at 1.896 Å and a broad asymmetric shoulder up to the first minimum at 2.46 Å. The average coordination numbers of Te and O atoms

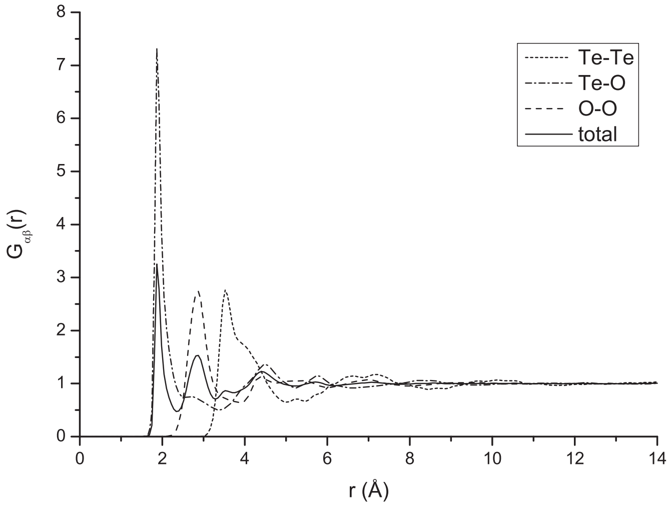

Figure 4.8: Partial and total radial pair distribution functions for modelled TeO_2 glass.

(n_{TeO} and n_{OTe}) calculated by integrating $T_{TeO}(r) = 4\pi r^2 \rho G_{TeO}(r)$ with cutoff radius $R_{cutoff} = 2.46$ Å have values of 3.93 and 1.97 respectively. These values are lower than those in crystalline structures (4 and 2). They are also in a good agreement with the *ab initio* MD results of Pietrucci *et al.* (n_{TeO} = 3.69 and n_{OTe} = 1.85) and with experimental results of Barney *et al.* (n_{TeO} = 3.68(4) and n_{OTe} = 1.84(1)) obtained with total neutron scattering techniques. In these works, a cutoff radius of 2.36 Å (proposed in [22] as well) was used. If we now calculate the coordination numbers with this cutoff value, we obtain n_{TeO} = 3.73 for tellurium atom and n_{OTe} = 1.86 for oxygen atom, which are in better agreement with the literature. As we can see, the Te atoms coordination number in tellurites is very sensitive to R_{cutoff} value and we will develop a detailed discussion on this problem in the next section.

4.1.4.2 Tellurium coordination number

Let us now discuss in more detail the problem of tellurium coordination number and cutoff radius for Te–O bonds. Fig. 4.9 (solid line) shows coordination number of Te atoms as a function of the cutoff radius. The coordination number curve keeps increasing without any flat region indicating a large variety of Te–O distances. This means that there is no characteristic cutoff radius that could unambiguously define the first coordination sphere of the tellurium atom and its coordination number. This problem of the broad Te–O distances distribution and no unequivocal definition of cutoff radius was already raised in [38, 26], but it has never been considered more elaborately. In this work we propose to explicitly take into account the presence of the Te LP, when defining the cutoff radius for Te–O bonds. Each TeO_x unit has its stereo-chemically active Te LP on one side and the bonded oxygen atoms on the other side. So it is incorrect to consider oxygen atoms on the LP side as being bonded to the Te atoms even if they lie within the given cutoff radius.

The explicit treatment of tellurium LP as a shell allows us to distinguish between bonded and non-bonded oxygen atoms in the Te coordination sphere of given radius. For this purpose we considered the distribution of the angles (ϕ) between oxygen atom inside the Te coordination sphere of the radius R_{cutoff} = 2.46 Å, Te core and Te shell (the LP) (Fig. 4.10). As we can see, this distribution consists of three regions: two broad peaks at 80–100 degrees and at 110–140 degrees which correspond to axial and equatorial oxygen atoms respectively, and a shoulder between 50 and 80 degrees on the left. This last interval corresponds to the oxygen atoms that lie on the LP side of the TeO_x unit and should not be taken into account when calculating Te coordination number.

We investigated the Te atom environment in a number of crystalline tellurite structures and defined a new criterion ϕ_{cutoff} = 75° for oxygen atoms that contribute to Te coordination number. The dotted line in Fig. 4.9 shows a new accumulated coordination number for Te–O pairs considering the new cutoff criterion and this time the curve has a characteristic flat region that starts from approximately 2.4 Å. Now when calculating the coordination numbers of Te and O atoms from the glass structure configuration and taking into account two cutoff criteria ϕ_{cutoff} = 75° and R_{cutoff} = 2.46 Å, we obtain n_{TeO} = 3.63 and n_{OTe} = 1.81. These values are clearly smaller than those obtained with the same cutoff radius but without the ϕ_{cutoff} criterion. This indicates that not taking into account this latter criterion systematically overestimates the coordination number by including incorrect oxygen atoms from a chemical point of view. In addition, using R_{cutoff} = 2.36 Å and ϕ_{cutoff} = 75° does not change so much the coordination numbers (n_{TeO} = 3.55 and n_{OTe} = 1.77), which confirms the robustness of the ϕ criterion. From these remarks it appears that for tellurite glass systems, the first minimum of the $T_{TeO}(r)$ (2.46 Å) is not the best choice for calculating the coordination number, and that a smaller cutoff radius value (for example, 2.36 Å) gives a better estimation if the ϕ_{cutoff} criterion is not considered.

4.1.4.3 Structural units distribution

The structural units distribution of the glass structure model obtained with the best criteria (R_{cutoff} = 2.46 Å and ϕ_{cutoff} = 75°) are reported in Table 4.1. It shows that the structure contains a large variety of Q_m^n polyhedra with a large proportion (about 43%) of threefold units. This directly contributes to the decrease of Te coordination number to n_{TeO} = 3.63. There is about 50% of four-coordinated Te atoms and a small amount (7%) of five-coordinated Te atoms. A large content (21%) of terminal oxygen atoms bonded

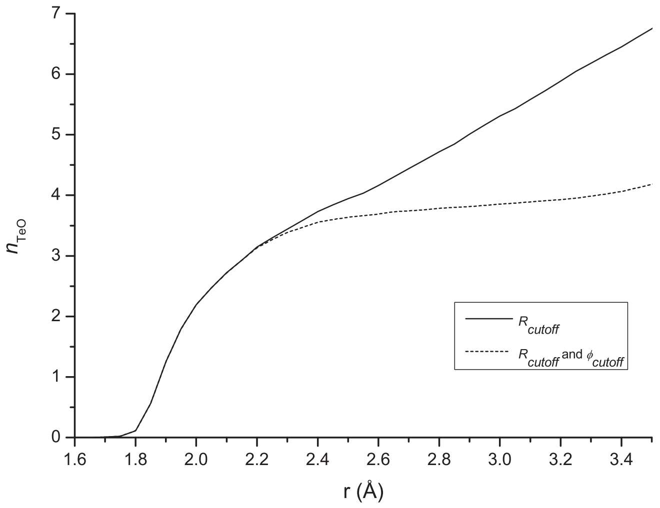

Figure 4.9: Accumulated tellurium atom coordination number with only R_{cutoff} criterion (solid line) and with two cutoff criteria ϕ_{cutoff} = 75° and R_{cutoff} (dotted line).

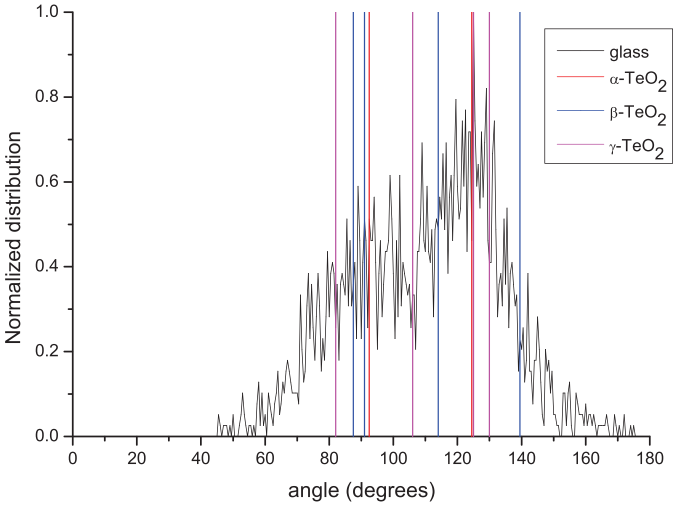

Figure 4.10: Normalised O–Te(core)–Te(shell) angle distribution with R_{cutoff} = 2.46 Å in the TeO_2 glass model. Color vertical lines correspond to these angles in α- (red), β- (blue) and γ-TeO_2 (magenta) crystalline structures (optimised with used IAP).

only to one Te atom was found in the glass structure and a negligible amount (about 3%) of three-coordinated oxygen atoms.

In Table 4.1 we also give the Q^n_m polyhedra distribution calculated with other cutoff values discussed in previous section. As we can see, considering the R_{cutoff} = 2.46 Å without ϕ cutoff criterion gives the highest discrepancies, which emphasises the discussion of Sec. 4.1.4.2.

The O–Te–O and Te–O–Te bond-angle distributions (BAD) are reported in Fig. 4.11. The O–Te–O BAD has two peaks: one between 70° – 110° and the other, much less intense, between 150° – 180°. The peak at smaller angles includes the O_{eq}–Te–O_{eq} angles of α–, β– and γ–TeO_2 phases (99° – 103°), but its maximum is shifted to 90° that corresponds more to O_{eq}–Te–O_{ax} angles. The second peak corresponds to O_{ax}–Te–O_{ax} angles. A quite narrow peak of Te–O–Te BAD argues for rather corner-sharing character of polyhedra connection and the absence of edge-sharing polyhedra. The BAD statistics does not differ significantly when considering only R_{cutoff} criterion.

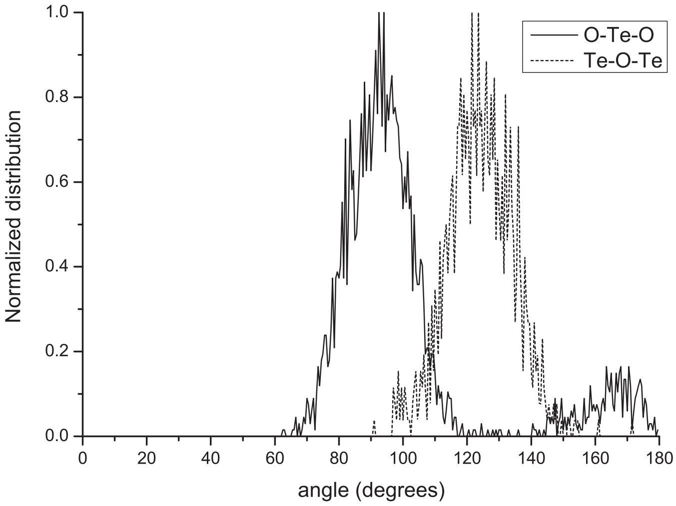

Figure 4.11: Normalised BAD. The solid line is for O–Te–O BAD and the dashed line is for Te–O–Te BAD.

4.1.4.4 Rings statistics

In order to obtain the information on the Intermediate Range Order (IRO) of the glass, we performed a rings statistics analysis of the final MD configuration. We used the RINGS code [116] for this purpose. RINGS allows obtaining the following quantities: $R_C(n)$, the number of rings of n nodes per cell in the material, $P_N(n)$, the proportion of nodes, which form at least one ring of size n, and, $P_{max}(n)$ and $P_{min}(n)$, the probabilities that a ring with n nodes represents respectively the longest or the shortest ring for given node [116].

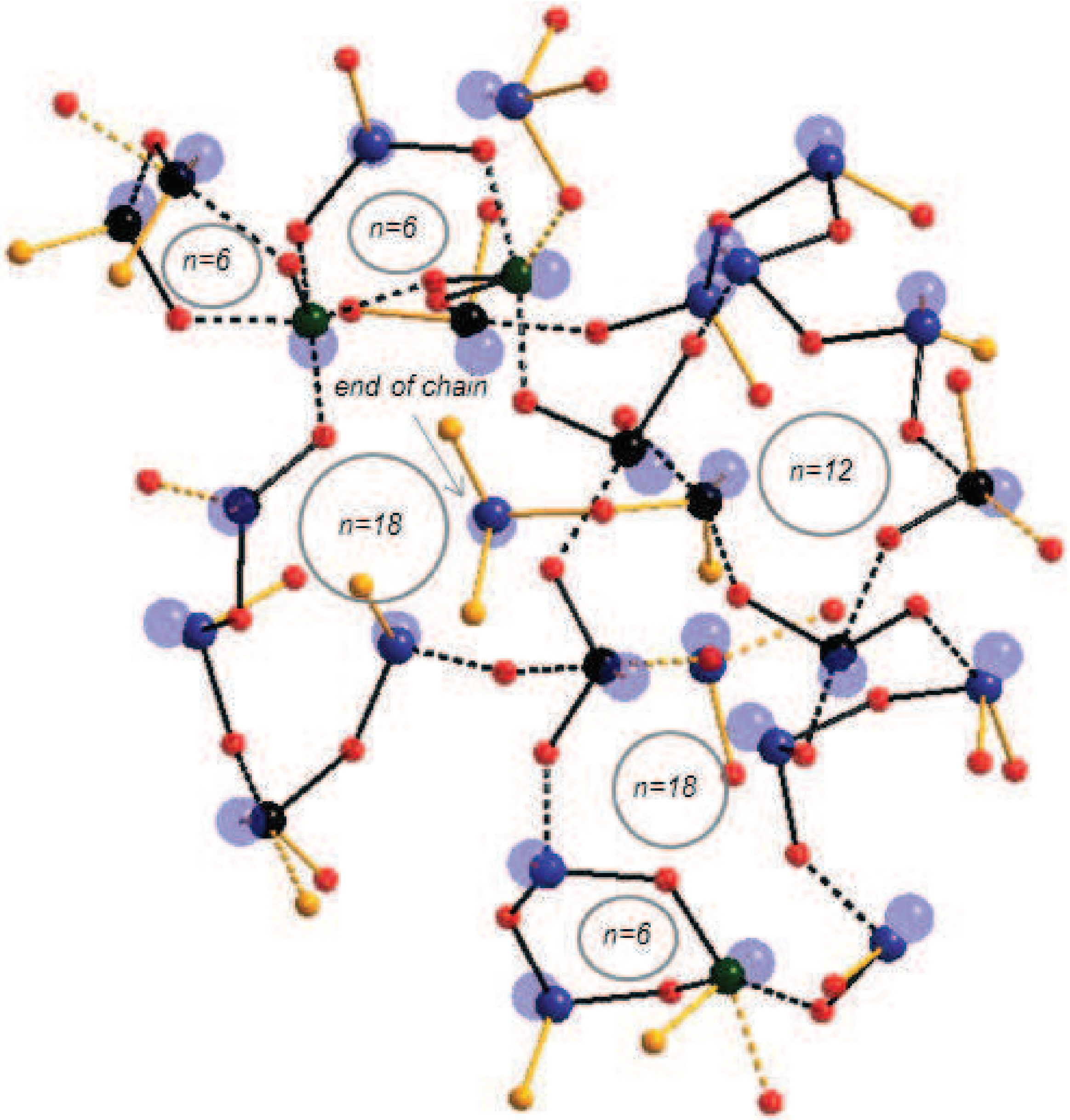

Figure 4.12: A fragment of the TeO_2 glass model as-obtained with MD simulations and illustrating typical chains and rings present in the structure. Oxygen atoms are presented in the small spheres (red for BO and yellow for NBO), tellurium atoms are the medium size spheres (black for four-coordinated, indigo for three-coordinated and dark green for five-coordinated Te) and Te LPs are the big transparent blue spheres. The solid lines represent the short Te–O bonds (< 2.02 Å) and dashed lines represent intermediate and long bonds ($2.02 < d < 2.36$ Å). The black bonds emphasise the rings in the structure and n in the circles indicates the amount of nodes in each found ring.

Table 4.1: The Q_m^n units distribution in % in the TeO_2 modelled glass structure.

	Q_3^1	Q_3^2	Q_3^3	Q_4^2	Q_4^3	Q_4^4	Q_5^4	Q_5^5
This work (ϕ_{cutoff} and R_{cutoff} = 2.46 Å)	1.19	18.15	23.96	0.59	19.05	30.51	2.08	4.46
This work (R_{cutoff} = 2.46 Å)	0.0	4.76	20.68	0.29	10.27	46.13	3.27	13.99
This work (ϕ_{cutoff} and R_{cutoff} = 2.36 Å)	1.49	22.17	26.04	0.74	18.75	25.6	2.08	3.13
This work (R_{cutoff} = 2.36 Å)	0.45	12.8	24.4	0.59	14.29	37.95	2.83	6.55
Ab initio MD [26]	0.6	14.9	20.4	0	17.1	35.9	0	9.4

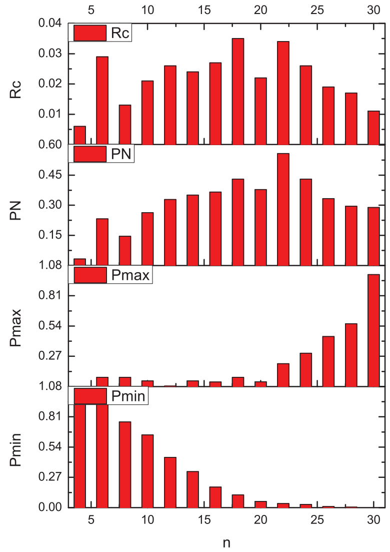

Figure 4.13: Primitive rings statistics for pure TeO_2 modelled glass. $R_C(n)$ is the number of rings of n nodes per cell in the material, $P_N(n)$ is the proportion of nodes, which form at least one ring of size n, and $P_{max}(n)$ and $P_{min}(n)$ are the probabilities, that a ring with n nodes represents respectively the longest or the shortest ring for given node.

A n-membered ring is a ring containing n nodes and the results are reduced to the total number of nodes in the networks. In such a manner, it is possible to compare the results for systems with different number and/or nature of nodes.

In Fig. 4.13 we present the rings statistics of the final MD configuration obtained for primitive rings search. A ring is primitive [117] if it can not be decomposed into two smaller rings. It is significant, that for rings statistics analysis with RINGS we could use only $R_{cutoff} = 2.36$ Å criterion, but we suppose that consideration of the ϕ_{cutoff} criterion would have changed the results not very strongly so that qualitative conclusions would have rested the same. The rings analysis was carried out using 30 nodes as maximum search depth.

The $R_C(n)$ values for TeO_2 system are really low, which indicates the small amount of rings in the system and hence the weak network connectivity. Furthermore, the rings with $n \geq 10$ predominate in the TeO_2 glass configuration. As $P_N(n)$, the proportion of nodes, is high for rings with $n \geq 10$, they can be considered as a global characteristic of the network.

Let us now consider the $P_{min}(n)$ and $P_{max}(n)$ values. For $n < 8$ we get $P_{min}(n) \cong 1$ meaning that the small rings of 4–8 nodes are always the shortest path for the given node and, hence, one particular node can not be the origin of several small rings. Otherwise it would be an evidence for a quite compact glass structure. The $P_{max}(n)$ reaches the value of 1 only for 30 nodes search. This implies, that the shortest paths of 30 nodes could be found and points out on the openness of the network and the presence of voids in the structure.

4.1.4.5 Te–O–Te bridges distribution

In the previous chapter it was discussed that the γ−TeO_2 polymorph is the closest crystalline structure to pure TeO_2 glass as it has common band in Raman spectra, which corresponds to the vibrations of symmetrical Te–O–Te bridges. We recall here that we consider the bridge as nearly symmetrical for $\delta = 2.019$ Å−1.948 Å= 0.07 Å (in γ−TeO_2) and as essentially asymmetrical for $\delta = 2.197$ Å−1.895 Å= 0.34 Å (in γ−TeO_2) and $\delta = 2.121$ Å−1.880 Å= 0.241 Å(in α−TeO_2).

Let us now consider the results for the optimised γ−TeO_2 and α−TeO_2 structures. We obtain the following values of δ: $\delta = 2.060$ Å−1.865 Å= 0.20 Å in γ−TeO_2 ("symmetrical" bridges) and $\delta = 2.253$ Å−1.819 Å= 0.43 Å in γ−TeO_2 and $\delta = 2.130$ Å−1.836 Å= 0.294 Å in α−TeO_2 (essentially asymmetrical bridges). As was discussed in Chapter 3, these subtle differences are slightly exaggerated as our IAPs tend to underestimate short bond lengths and to overestimate long bond lengths. In such a manner, the difference between symmetrical and asymmetrical bridges is shifted to larger δ values. For our modelled glass

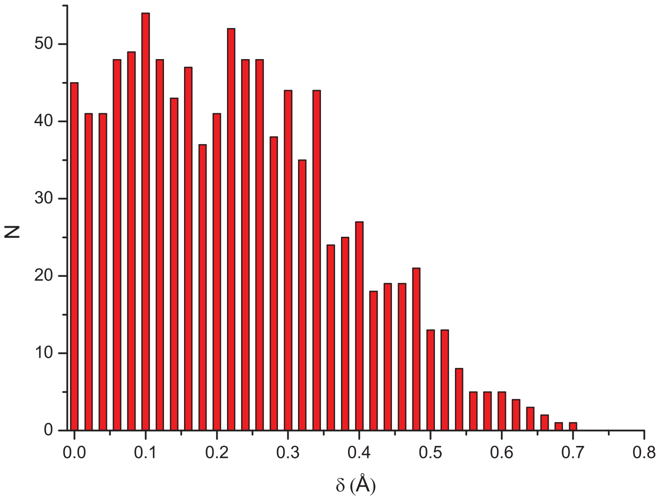

Figure 4.14: Distribution of the differences in bond lengths δ for all BO atoms in the modelled glass.

structure we will consider the bridges with $\delta < 0.2$ Å as symmetrical.

Let us now consider the distribution of the bridges in the modelled glass structure. Fig. 4.14 reports the absolute number of bridges with the difference in the bond lengths δ. The distribution demonstrates the predominance of the bridges with $\delta < 0.5$ Å with the tail up to 0.7 Å. The nearly symmetrical bridges make up about 48% considering the $\delta < 0.2$ Å criterion. Hence, the symmetrical bridges make a very important contribution to bridges distribution, which reinforces the idea that the glass structure is closer to $\gamma-TeO_2$ polymorph than to $\alpha-TeO_2$ polymorph.

4.1.5 Discussion

Having done the statistics description of the glass structure let us consider a fragment chosen randomly in the modelled glass structure. In Fig. 4.12 several rings are presented as well as chains with terminal oxygen (NBO) atoms. TeO_x units tend to form large rings ($n \geq 10$), probably, because of the tellurium LP (big blue transparent spheres in Fig. 4.12) steric effect. Indeed, when forming small rings, all the LPs could hardly be oriented inside the small ring so that each TeO_x unit should take into account its orientation with respect to the other. Accordingly, this could be a reason why TeO_2 glass forms such an open network with voids created by the LP steric effect.

From the rings statistics and from. Fig. 4.12 we can see that a large amount of NBO atoms (see Sec. 4.1.4.3) in the glass structure plays an important role (together with electronic LP steric effect) in forming the glass network. This could be due to the high proportion of terminal oxygen atoms that prevents the closure of the rings and indicates a more open network [118].

Our model of the amorphous TeO_2 structure agrees in general with the one proposed in [27], but it is much more irregular and consists of a larger variety of TeO_x units. Indeed, our model of open network with weak connectivity and a large amount of terminal oxygen atoms supports the concept that NBO atoms and low tellurium coordination numbers are the reason of facile accommodation of modifier atoms, as expressed in [27]. Possibly, the amount of NBO atoms allows stabilising the glass structure when adding a modifier (M_nO_m) by creating M–O bonds with terminal oxygen atoms thus reinforcing the connectivity of the glass network.

Let us now compare our amorphous TeO_2 model with the one obtained by *ab initio* MD simulations in [26]. The Q_m^n structural units distribution in that work is quite close to those for our model (particularly if considering only R_{cutoff} criterion). Pietrucci *et al.* report about 14% of NBO atoms which is 7% less than in our model. As mentioned above, the authors suppose that such a large concentration of NBO atoms is due to a high cooling rate used in the quenching protocol, which might have brought the system to the frozen liquid state. The glass model in their work was obtained as a result of 16 ps cooling the liquid at a rate of $\cong 10^{14}$ K/s, as *ab initio* simulations are very time-consuming. With our classical MD simulations, we could perform a much longer quenching protocol. As it was mentioned in Sec. 4.1.2, the total simulated time is about 350 ps which is significantly longer. Nevertheless, we found even more NBO atoms and weaker connectivity of the network as in *ab initio* MD simulated glass structure. Thus we suppose that these are really characteristics of the TeO_2 amorphous state.

4.1.6 Conclusions

MD simulation of the pure TeO_2 glass was performed for a system containing 672 TeO_2 units and a total simulation time of about 350 ps. The calculated total PDF is in a good agreement with the experimental one obtained by neutron diffraction method. Hence we consider our glass structure model as realistic.

The glass structure model has a broad Q_m^n units distribution with a large variations of Te–O bond lengths. We developed a new criterion, which allows us to precisely define the first coordination sphere of Te atom by explicitly taking into account the stereochemically active Te electronic LP. This criterion is the angle between oxygen atom inside the Te coordination sphere of the radius $R_{cutoff} = 2.46$ Å, Te core and Te shell (the LP) and it was set to 75°.

The Te coordination number in the modelled glass is $n_{TeO} = 3.63$ and is in good agreement with these ones obtained by *ab initio* MD simulation [26] and by neutron diffraction methods [27]. This result together with Q_m^n units distribution implies a large amount of NBO atoms (21%) in the glass structure, which confirms the results of the mentioned above studies as well.

We carried out the rings statistics analysis and investigated the modelled glass structure. The pure amorphous TeO_2 network has a weak connectivity, terminated chains and large ($n \geq 10$) rings. This is due to large number of NBO atoms and the stereochemical effect of Te electronic LP that the TeO_2 glass has such a badly connected network. Possibly, these peculiarities explain the instability of the glass towards to devitrification and its good ability to accommodate the modifiers.

The MD simulations of modified TeO_2 glasses would be of a great interest. It could clarify the role of the modifiers oxides in TeO_2-based glasses, how modifiers atoms incorporate into the glass network, the role of the NBO atoms and the changing of the Te coordination number, *etc.* There are a number of well studied experimentally systems and some of them were briefly reviewed in Chapter 1. One can be interested in such systems as K_2O–TeO_2, Cs_2O–TeO_2, V_2O_5–TeO_2, Tl_2O–TeO_2. However, one have to be sure in the quality and transferability of the IAPs for modifiers oxide. As we discussed in Sec. 3.2 of Chapter 3, it seems that IAP for K^{1+}–O^{2-} system is not suitable to use together with our IAPs for Te^{4+}–O^{2-} system. To the best of our knowledge there are no established potentials of a good quality and high transferability for V^{5+}–O^{2-} and Tl^{1+}–O^{2-} systems. In such a manner, the MD study of modified TeO_2 glasses is a complex problem and requires a solid approach.

4.2 Structure of δ−TeO_2 polymorph. Theoretical and experimental approaches.

4.2.1 Average structure

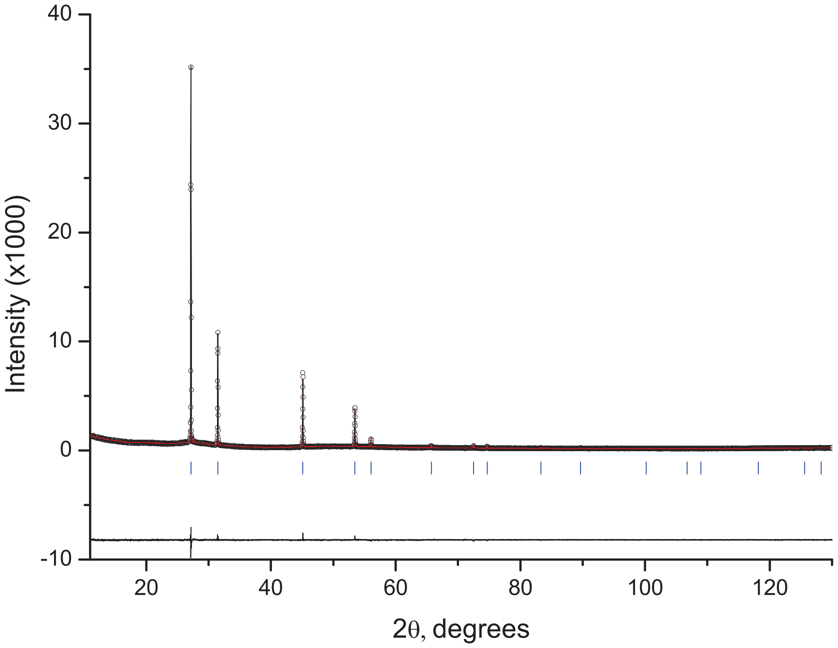

Figure 4.15: Rietveld fit of the XRD powder diffraction pattern of the δ−TeO_2 sample. $R_p = 4.66\%; R_{wp} = 6.09\%; R_B = 5.97\%; \chi^2 = 1.40; DW = 1.47$.

The X-ray powder diffraction pattern of the δ−TeO_2 polymorph is reported in Fig. 4.15. The diffraction lines are relatively thin, indicating that the structure has a fairly well-defined long-range order. The peaks intensity decreases rapidly with the diffraction angle θ and is hardly observable above $2\theta = 80°$.

The fit of the pattern was performed with the Rietveld method using the FULLPROF [73] software. We used the model of the perfect fluorite lattice (F $m\bar{3}m$ space group) with cations occupying the positions 4a (0, 0, 0) and anions the positions 8c (0.25, 0.25, 0.25). The refinement results are presented in Table 4.2. The refined cell parameter is $a = 5.679$ Å. The atomic displacement parameters (ADPs) are very large (9.89 Å^2 for the cations and 27.12 Å^2 for the anions), which clearly indicates the large atomic displacements with respect to their average positions. In addition, as was discussed in Section 1.1.1.4 of Chapter 1, the Te–O distances obtained with average atomic positions are equal to 2.46 Å and strongly larger than those usually found in tellurites.

The obtained fit is rather good but not perfect. The fit can be improved with a split

Table 4.2: Results of the Rietveld refinement of the XRD pattern of $\delta-TeO_2$ polymorph. Two models are reported: perfect fluorite model ($4a$ sites for Te atoms and $8c$ sites for O atoms) and split atom refinement ($32f$ sites for both atoms).

		Model parameters			
Atom type	Model	x/a	y/a	z/a	B_{iso}, Å^2
Te	Perfect fluorite	0	0	0	9.89
	Split atoms at $32f$	0.043	0.043	0.043	5.55
O	Perfect fluorite	0.25	0.25	0.25	27.12
	Split atoms at $32f$	0.326	0.326	0.326	8.32

atom refinement, in which tellurium and oxygen atoms fill the $32f$ (x, x, x) positions. The refined positions are $x = 0.043$ and $x = 0.326$ for Te and O atom respectively, and the isotropic displacement parameters drop to $B_{Te} = 5.55$ Å^2 and $B_O = 8.32$ Å^2. The reliability factors are the following: $R_p = 4.57\%; R_{wp} = 5.95\%; R_B = 3.66\%; \chi^2 = 1.33; DW = 1.53$. Split atom refinements generally enable to take into account a non-Gaussian probability density function of the atomic positions. Thus, the large displacement obtained in the $< 111 >$ direction indicates that whereas its average position is (0.25, 0.25, 0.25), few atoms are likely shifted towards the centre of the cell or the middle of the edges [17]. The structure obtained with such a model is presented in Fig. 4.16. The Te–O distances in such a model (1.93 Å, 2.16 Å, 2.35 Å and 2.37 Å) are closer to those found in tellurites.

Effectively, the average structure of $\delta-TeO_2$ polymorph really resembles the one of $\beta-Bi_2Te_4O_{11}$ studied in [17] and briefly discussed in Section 1.1.1.4 of Chapter 1. However, the isotropic ADPs for $\delta-TeO_2$ are significantly larger than those for $\beta-Bi_2Te_4O_{11}$ ($B_{Te} = B_{Bi} = 4.7$ Å^2 and $B_O = 14.6$ Å^2), indicating that the disorder in $\delta-TeO_2$ is much more important.

Hence, the description of this structure with the fluorite model is incomplete and require an atomistic modelling approach.

4.2.2 Molecular dynamics simulations

4.2.2.1 Computational details

The starting configuration for MD simulations was build from the perfect fluorite-type lattice discussed in previous section (F $m\bar{3}m$, $a = 5.679$ Å, Te $(4a) : x = y = z = 0$, O $(8c) : x = y = z = 0.25$). The simulation box comprised 6 × 6 × 6 unit cells (34.07 Å× 34.07 Å× 34.07 Å) so that it contained 864 TeO_2 units (5184 particles including Te and O atoms shells). The Te and O atoms shells were initially superposed on the corresponding

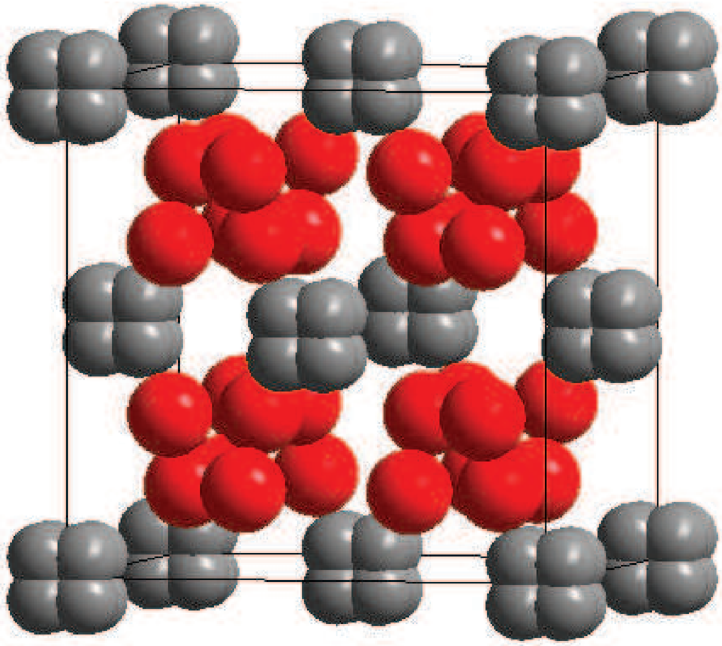

Figure 4.16: Representation of the average structure of the $\delta-TeO_2$ polymorph with the split atom refinement with $32f$ (x,x,x) positions. $B_{Te} = 5.55$ Å^2 and $B_O = 8.32$ Å^2.

cores.

We performed several simulation jobs in order to investigate the evolution of our model with different MD conditions. Firstly, we performed the simulation job of a total time of 100 ps at 300K (room temperature (RT)) in the NPT ensemble. Then the final configuration obtained at RT was heated up to 900K and kept at this temperature for 200 ps and then cooled down to 300K with infinite cooling rate in one case and with finite cooling rate in the other case. For the simplicity, the final configurations of these simulations will be referred to as the: (i) RT configuration; (ii) FC (fast cooling) configuration; and SC (slow cooling) configuration.

In order to judge the quality of the obtained models, we used the data obtained from the Rietveld refinement: the cell parameter, average atoms positions and ADPs. Basing on the refinement results we expected to obtain a final model of $\delta-TeO_2$ polymorph with highly disordered Te atoms around average position $x = y = z = 0$ and about 3 times (in terms of B parameters) more disordered O atoms around average position $x = y = z = 0.25$. So let us now briefly discuss the way of the calculation of B parameters for the modelled structures.

4.2.2.2 Calculation of atomic displacement parameters.

By definition (*e.g.* [119]) the isotropic atomic displacement parameter B is

$$B = 8\pi^2 U = 8\pi^2 < u^2 > \tag{4.1}$$

where u is the atomic displacement of a given type of atom with respect to an ideal position. The average <> can be performed both in space and time. The square root of U provides an r.m.s. (root-mean-square) value for the atomic displacement.

In order to obtain the distribution of the atoms around their perfect atomic positions in the final configuration, we did as follows. Firstly, the simulation box of 6 × 6 × 6 unit cells was projected into one unit cell and further we applied the site symmetry operations to each atom in such a way to bring it to its Wyckoff position. We, hence, calculated the anisotropic ADPs B_{xx}, B_{yy}, B_{zz} for Te and for O atoms as:

$$B_{ii} = 8\pi^2 \frac{1}{N} \sum_j (i_j - i_0)^2 \tag{4.2}$$

where $i = x, y, z$ is the coordinate of the atom j, $i_0 = x_0, y_0, z_0$ is its Wyckoff position coordinate ($x = y = z = 0$ for Te atoms or $x = y = z = 0.25$ for O atoms) and the sum is over all atoms of considered type. The equivalent isotropic ADPs were calculated as was proposed by [120] and [119]:

$$B_{eq} = \frac{1}{3}(B_{xx} + B_{yy} + B_{zz}). \tag{4.3}$$

4.2.2.3 Room temperature molecular dynamics simulation

So, the first obtained RT configuration is characterised by the cell parameter $a = 5.599$ Å, which is 1.4 % less than the experimental value, and by ADPs $< B_{Te} >= 9.69$ Å^2 and $< B_O >= 15.03$ Å^2. The ratio of these values is then 0.645, which is almost twice larger than the experimental one (0.365). Effectively, our system changed strongly with respect to the initial configuration. We can clearly see it from the strong decrease of configurational energy (E_{cfg}) with the time (Fig. 4.17). (In our model the configurational potential energy consists of the potential energy of Van der Waals, Coulombic and core-shell interactions.) However, the estimated 3D diffusion coefficients are rather small at room temperature ($2.6 \cdot 10^{-13}$ m^2/s for Te atoms and $9.9 \cdot 10^{-13}$ m^2/s for O atoms). Hence, one can suppose that at RT, the system was just locally relaxed and a more appropriate approach requires the MD simulation at a higher temperature, when the atoms can better explore the phase-space. To do so, we aimed to correctly choose the simulation temperature so that the atoms had enough of mobility and in the same time the chosen temperature was below the melting point.

4.2.2.4 Molecular dynamics simulation at 900K

We performed several short test MD runs at different temperatures and monitored the values of system configurational energy with the time. The results are presented in Fig. 4.18. As we can see, at 1700 K, 1600 K and 1500 K the $E_{cfg}(t)$ function has a remarkable

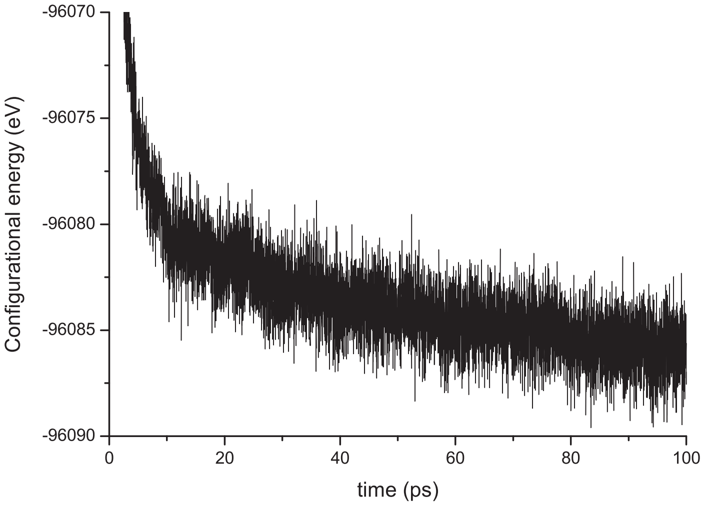

Figure 4.17: Configurational energy E_{cfg} of the system as a function of simulation time. Room temperature MD simulation.

slope that indicates the expansion of the system, possibly, leading to the system melting. At 1200 K we still observe a very slight slope, whereas at 900 K one can even remark that E_{cfg} tends to slightly decrease with the time. As such a subtle energy changes are very interesting to observe with the time, we performed a long simulation job of 200 ps at this temperature.

Fig. 4.19 reports the $E_{cfg}(t)$ for the simulation at 900 K together with the evolution of the ADPs ratio. The values of the approximate diffusion coefficients for this run are $3.4 \cdot 10^{-11}$ m^2/s for Te atoms and $4.6 \cdot 10^{-11}$ m^2/s for O atoms (two orders larger than at 300 K). Indeed, the configurational energy slightly tends to decrease with the time and it seems that the ADPs ratio is correlated with E_{cfg}. However, such fluctuations of the $E_{cfg}(t)$ and the ADPs ratio are provoked by rather subtle changes in atoms arrangement. Hence, we cannot expect that the ADPs values will approach to the experimental values.

4.2.2.5 Influence of the cooling rate.

We followed two cooling procedures for the configuration obtained at the end of the 200 ps run at 900 K: an infinite cooling rate, *i.e.* the temperature was directly set to 300 K, and a finite cooling rate with average cooling rate of 10 K/ps. The temperature as a function of time for the slow cooling simulation is reported in Fig. 4.20.

Let us now compare the configurational energies for three simulations (RT, FC and SC) reported in Fig. 4.21. The average values for the FC and SC configurations are clearly smaller than those for the RT configuration. The difference between E_{cfg} for FC and SC configurations is much more subtle. Both FC and SC configurations are the results of

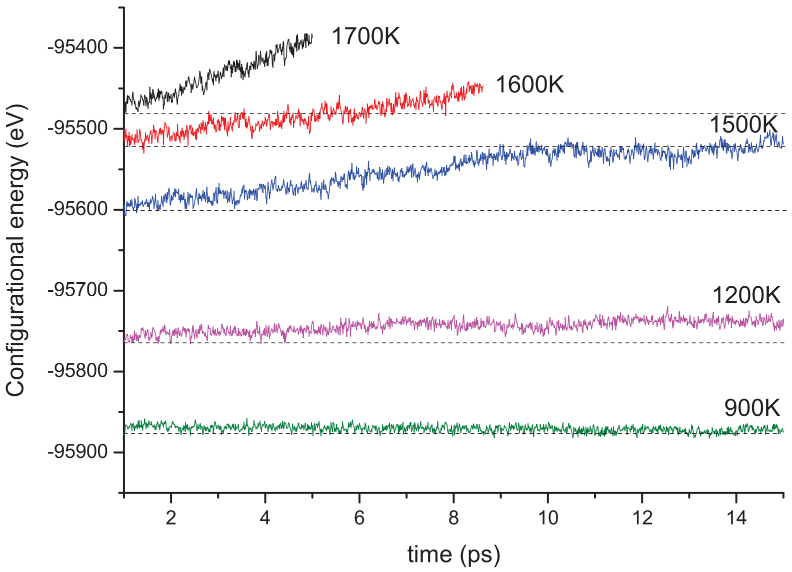

Figure 4.18: Configurational energy E_{cfg} of the system as a function of simulation time. MD simulations at 1700 K (black), 1600 K (red), 1500 K (blue), 1200 K (magenta) and 900 K (green).

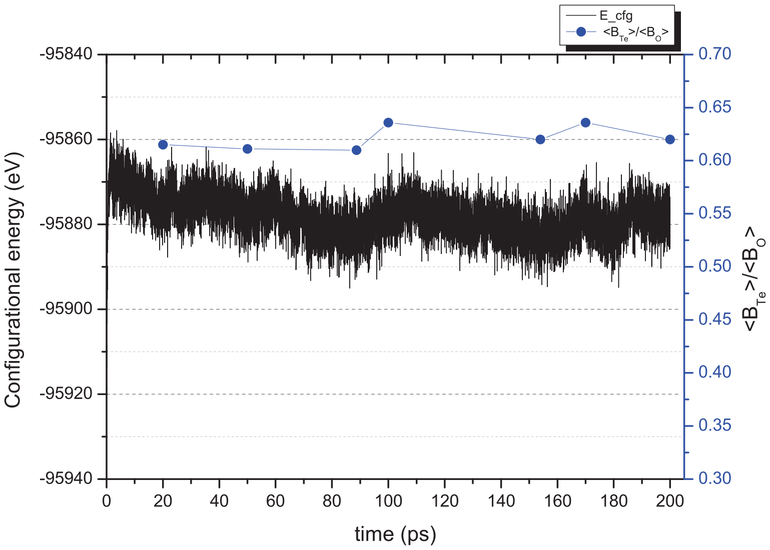

Figure 4.19: Configurational energy E_{cfg} (black) of the system and the ADPs ratio (blue) as the functions of simulation time. MD simulation at 900 K.

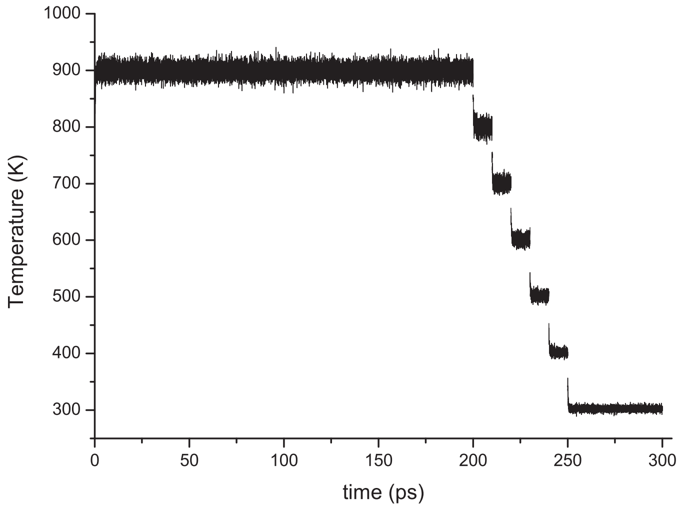

Figure 4.20: Temperature as a function of time in the slow cooling procedure for $\delta-TeO_2$ MD simulations.

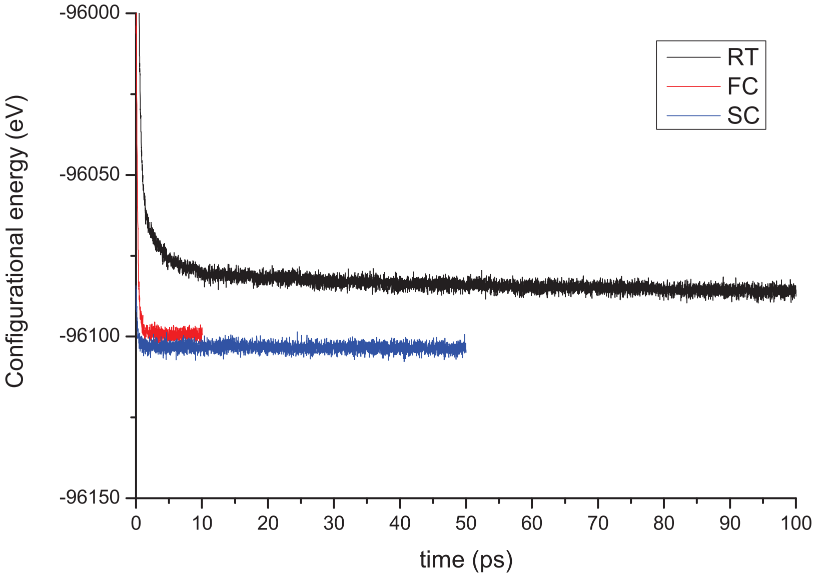

Figure 4.21: Configurational energy E_{cfg} of the system as a function of simulation time at 300 K for RT configuration (black), FC configuration (red) and SC configuration (blue).

Table 4.3: Values of equivalent isotropic displacement parameters $< B_{Te} >$ and $< B_O >$ and their ratios $< B_{Te} > / < B_O >$ and cell parameter a for $\delta-TeO_2$ modelled structures for different MD simulations (RT, FC, SC). The error (in %) in the cell parameter compare to experimental value in indicated in brackets.

	$< B_{Te} >$, Å^2	$< B_O >$, Å^2	$< B_{Te} > / < B_O >$	a, Å
RT	9.69	15.03	0.65	5.599 (1.4)
FC	9.92	16.05	0.62	5.611 (1.2)
SC	9.53	15.90	0.60	5.602 (1.4)

Table 4.4: The Q^n_m units distribution and NBO atoms population in % in $\delta-TeO_2$ modelled structures for different MD simulations: RT, FC and SC.

	Q^1_3	Q^2_3	Q^3_3	Q^2_4	Q^3_4	Q^4_4	Q^4_5	Q^5_5	NBO
RT	1.27	21.30	19.91	0.58	22.80	30.21	1.97	1.97	24.9
FC	0.69	19.56	20.14	0.58	22.34	30.09	1.50	4.63	23.1
SC	0.92	18.75	20.95	1.16	21.18	30.32	2.31	4.28	23.3

a much longer MD run compared to the RT configuration. The SC configuration was furthermore treated for some more time, which allowed our system to find a state with the smallest (among studied cases) configurational energy at the end.

An interesting question is how this difference in E_{cfg} is reflected in the statistical description of atomic arrangement in the modelled $\delta-TeO_2$ structures. In Table 4.3 we report the values of cell parameter a, isotropic APDs for Te and O atoms and their ratios; and in Table 4.4 we report the Q^n_m units distribution and NBO atoms population for obtained configurations. It is difficult to make any claims about significant changes from one configuration to another, but one can remark that the RT configuration differs stronger from the FC and SC configurations than the FC and SC configurations between each other. We can, however, state that the ratio $< B_{Te} > / < B_O >$ and NBO atoms population are slightly less for the SC configuration. We then consider this latter configuration as the best one as it has the smallest E_{cfg}, $< B_{Te} > / < B_O >$ and NBO atoms values. Hence, we will further consider the SC configuration as a $\delta-TeO_2$ structure model and use it for analysis.

4.2.3 Analysis of the final configuration.

4.2.3.1 Average structure.

We report the snapshots of the final SC configuration in Fig. 4.22, where Te and O atoms are represented in grey and red spheres correspondingly and the atoms shells are not represented. Fig. 4.22a presents the $< 0\ 0\ 1 >$ direction projection of our $\delta-TeO_2$ model and Fig. 4.22b its average structure in the same direction. These figures demonstrate its disordered nature and its relation to the fluorite structure. The cell parameter of the

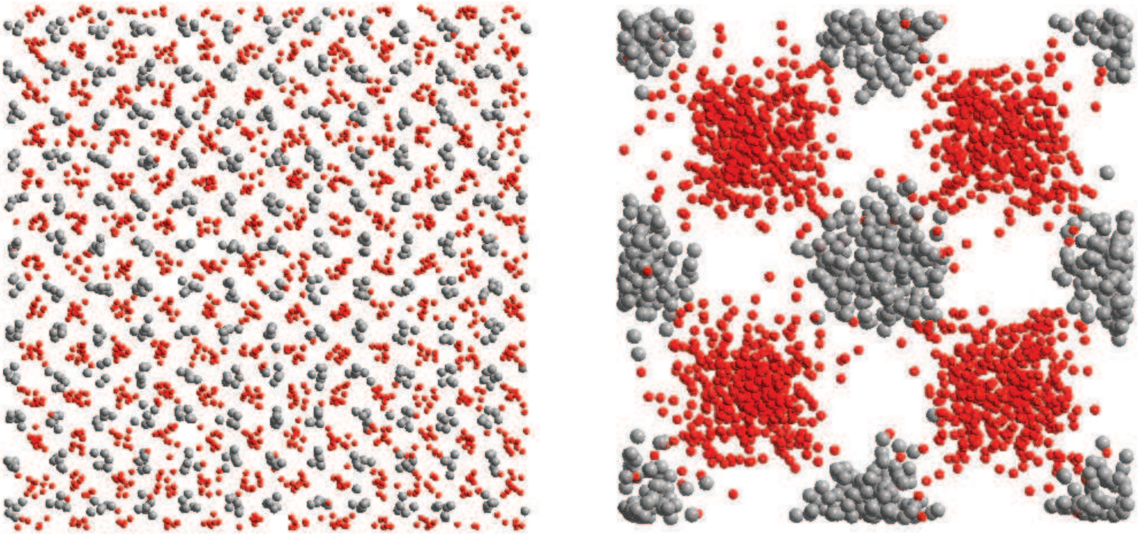

(a) $6 \times 6 \times 6$ unit cells simulation box.

(b) Average structure.

Figure 4.22: Projection in $< 0\ 0\ 1 >$ direction of the final SC configuration. Te atoms are represented in grey spheres and O atoms in red.

Table 4.5: Values of anisotropic and isotropic displacement parameters $< B_{Te} >$ and $< B_O >$ and their ratios $< B_{Te} > / < B_O >$ for modelled $\delta-TeO_2$ structure, experimental $\delta-TeO_2$ structure and experimental $\beta-Bi_2Te_4O_{11}$ structure [17].

		B_{Te}, Å^2	B_O, Å^2	$< B_{Te} > / < B_O >$
Modelled $\delta-TeO_2$				
	B_{xx}	8.91	16.02	
	B_{yy}	9.49	15.76	
	B_{zz}	10.21	15.90	
	$< B >$	9.53	15.90	0.60
Experimental $\delta-TeO_2$		9.89	27.09	0.35
Experimental $\beta-Bi_2Te_4O_{11}$		4.7	14.6	0.32

modelled $\delta-TeO_2$ structure is a = 5.602 Å (1.4 % error with respect to the experimental value).

In Table 4.5 we report the calculated displacement parameters for $\delta-TeO_2$ model together with the values obtained from the Rietveld analysis of X-ray powder diffraction data for $\delta-TeO_2$ and $\beta-Bi_2Te_4O_{11}$. As was discussed above, the ADPs ratio for Te and O atoms in our model is almost twice larger than experimental values. However, the Rietveld analysis shows a very important disorder in Te atoms (B_{Te} = 9.89 Å^2) and our model reproduces this result very well (B_{Te} = 9.53 Å^2). But according to our model, the disorder in O atoms is of the same order as in $\beta-Bi_2Te_4O_{11}$, whereas the B_O for $\delta-TeO_2$ is significantly higher (B_O = 27.12 Å^2).

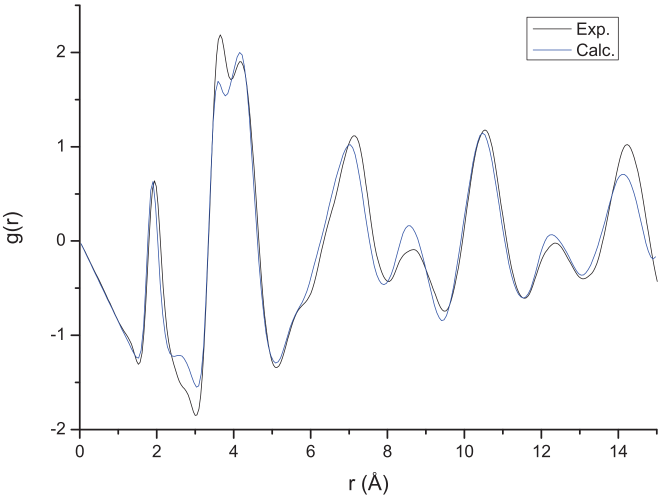

Figure 4.23: Total distribution function for $\delta-TeO_2$ structure obtained with X-ray total scattering (black line) and with MD simulations (blue line).

4.2.3.2 Experimental PDF from X-ray total scattering.

In the previous section we showed that the average structure of our $\delta-TeO_2$ model is in a good agreement with the information obtained with the Bragg scattering. Let us now consider the real structure, which could be described with the help of PDF. It can be obtained from the X-ray diffuse scattering signal and calculated from the modelled configuration.

The experimental PDF was obtained by means of X-ray total scattering experiment as described in Section 1.3 and reported in Fig. 4.23. The calculated PDF for our $\delta-TeO_2$ model is reported in the same figure. The envelope of the calculated PDF is in a very good agreement with the experimental one, which indicates that the obtained model is correct. The peaks of the calculated function are very slightly shifted towards the smaller values of r according to the slight underestimation of the calculated atomic density with respect to experimental one.

The PDFs obtained with X-ray total scattering experiment focuses mainly on the tellurium atoms arrangement as their X-ray atomic form factors are more important than those for oxygen atoms. Hence, the first less intensive PDF peaks at 1.9 Å and at 2.8 Å correspond to the shortest Te–O distances and to the typical O–O distances found in TeO_3 and TeO_4 polyhedra respectively. The further more intensive peaks at 3.65 Å and 4.16 Å correspond to Te–Te atomic distances. The use of the reduced PDF $g(r) = 4\pi\rho r^2(G(r)-1)$ reported in Fig. 4.23 allows to better demonstrate the peaks lying at the larger r values. Hence, the explicit oscillations of the $g(r)$ after 6 Å indicate the periodic character of the Te atoms arrangement.

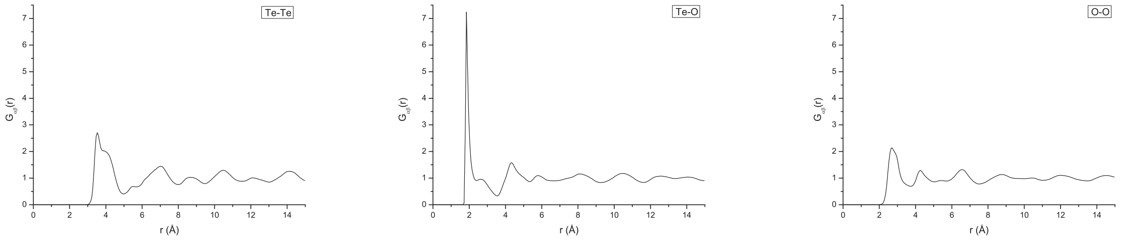

(a) Te–Te partial PDF. (b) Te–O partial PDF. (c) O–O partial PDF.

Figure 4.24: Partial PDFs for modelled $\delta-TeO_2$ structure.

4.2.3.3 The short and intermediate range orders

Let us now consider the partial pair distribution functions obtained from our MD model and reported in Fig. 4.24. The Te–Te partial PDF exhibits rather broad peaks with almost the same width and positions corresponding to FCC lattice. The remarkable intensity oscillations are observed up to the cutoff radius of the PDF. The Te–O partial PDF has an intensive and sharp maximum at 1.84 Å with an explicit broad shoulder at 2.66 Å and a broad maximum at 4.34 Å. The next coordination shells are barely resolved. The O–O distribution function exhibits the first maximum at 2.72 Å, which corresponds to the typical shortest O–O distances. Then it has two broad peaks at 4.28 Å and 6.59 Å and further becomes almost flat.

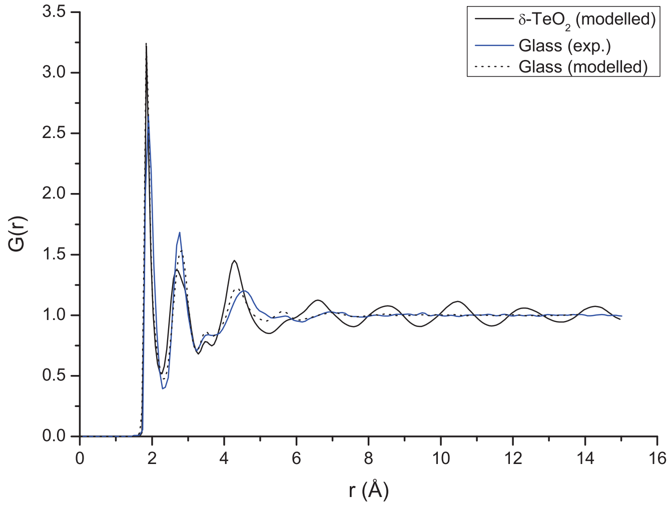

Figure 4.25: Total PDF for $\delta-TeO_2$ calculated for neutron scattering (black solid line) and compared with the calculated (black dashed line) and experimental (blue solid line) PDFs for pure TeO_2 glass.

One can see, that the partial pair distribution functions for $\delta-TeO_2$ are very similar to those for the pure TeO_2 glass (see Fig. 4.8 in Section 4.1.4.1), except the long-range order in Te-Te sublattice. Indeed, if we compare the calculated total PDF for neutron scattering for $\delta-TeO_2$ and for TeO_2 glass (Fig. 4.25), we find the same peaks positions up to ~5 Å. These peaks of $\delta-TeO_2$ PDF are slightly more intense and narrow than for the glass, which corresponds to a better atoms ordering in the short-range order in disordered crystalline phase. Hence, the first Te–O, Te–Te and O–O coordination shells are very similar for $\delta-TeO_2$ and the pure TeO_2 glass structure.

Let us now consider the total PDF peak at 4.28 Å. We recall here that this peak in the total PDF for modelled glass structure had the largest position error with respect to the experimental data. It was supposed in Section 4.1.4.1 that this error could be due to the use of the rigid-ion model for oxygen atoms and/or high cooling rate during the quenching process.The $\delta-TeO_2$ model was obtained with completely different MD conditions (*i.e.* simulations time and temperature) and core-shell model for both atom types (thanks to the lower working temperatures). However, we find the same position error for the peak at 4.28 Å, which means that this feature comes from the IAPs rather than from MD simulation conditions.

4.2.3.4 Distribution of Te and O atoms around their average positions

Let us now discuss in more detail the distribution of Te and O atoms around their average positions. The calculated anisotropic displacement parameters B_{xx}, B_{yy} and B_{zz} (with respect to 4*a* and 8*c* Wyckoff positions) for Te and O atoms are given in Table 4.5. For both atoms we have $B_{xx} \approx B_{yy} \approx B_{zz}$, which corresponds to a spherical distribution with the probability maximum centred at (0, 0, 0) for Te atoms and at (0.25, 025, 025) for O atoms. Indeed, it seems to be a reasonable description for Te atoms, as seen in Fig. 4.22b. However, in the same figure one can note that in the $< 0\ 0\ 1 >$ projection the distribution of O atoms have a nearly square form. Moreover, if we now consider the $< 1\ 0\ 1 >$ projection of the average $\delta-TeO_2$ structure (Fig. 4.26a), we can see that the O atoms distribution has a triangle form.

One can imagine this distribution as a tetrahedron with an origin at the 8*c* position and the vertices at the 32*f* positions: (x, x, x), $(x, 1/2 - x, 1/2 - z)$, $(1/2 - x, 1/2 - x, z)$ and $(1/2 - x, x, 1/2 - z)$. Fig. 4.26b shows all the atoms in the simulation box gathered in the 4*a* and 8*c* positions with O atoms represented in transparent red spheres for the sake of convenience. One can note that the density of such a tetrahedron distribution is not homogeneous. Such a distribution could be rather modelled with the thermal anisotropic ellipsoids inscribed in a tetrahedron. This is to say, that thermal anisotropic ellipsoids have their origins at 32*f* positions. Such a configuration is shown in figures 4.27a, 4.27b, 4.27c. Indeed, this model for oxygen atoms distribution represents very well

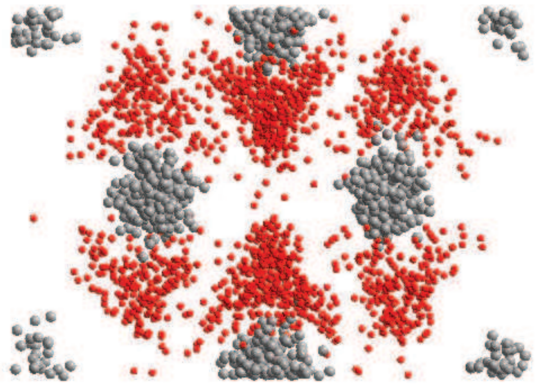

(a) Projection of average structure in the < 1 0 1 > direction.

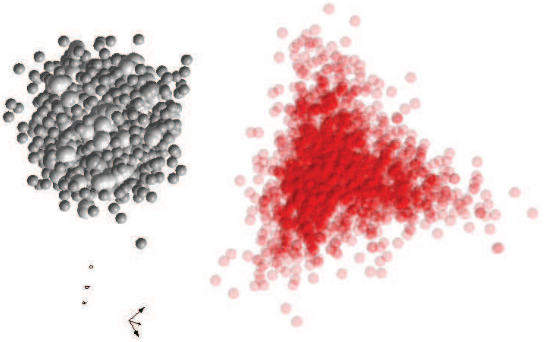

(b) All Te and O atoms in simulation box assembled in 4a and 8c positions respectively. O atoms are represented in transparent red spheres for the sake of convenience.

Figure 4.26: Modelled $\delta-TeO_2$ structure. Te atoms are represented in grey spheres and O atoms in red.

(a) 3D view.

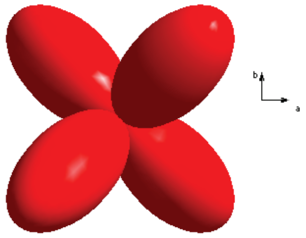

(b) Projection in the < 0 0 1 > direction.

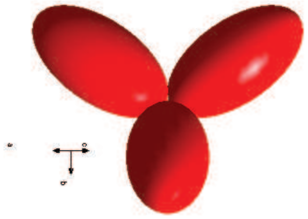

(c) Projection in the < 1 0 1 > direction.

Figure 4.27: Thermal anisotropic ellipsoids with the origin at 32f positions.

the distribution obtained with MD simulations.

The presented description of the oxygen atoms distribution around 32f positions accords with the results of a split atom refinement of the X-ray powder diffraction pattern presented in Section 4.2.1. Let us now wonder about the effect of the anisotropic ADPs on the Rietveld refinement results. We report the results of such a fit in Table 4.6. (We considered anisotropic ADPs for both atom types.) The equivalent isotropic parameters are slightly larger than for the case of refinement with isotropic parameters, but the

Table 4.6: Results of the Rietveld refinement of the XRD pattern of $\delta-TeO_2$ polymorph considering split atom model (32f sites for both atoms) and anisotropic B_{ij}.

	Model parameters				
Atom type	x/a	y/a	z/a	B_{ii}, Å^2	B_{ij}, Å^2
Te	0.0342	0.0342	0.0342	7.35	-1.29
O	0.3194	0.3194	0.3194	12.65	3.55

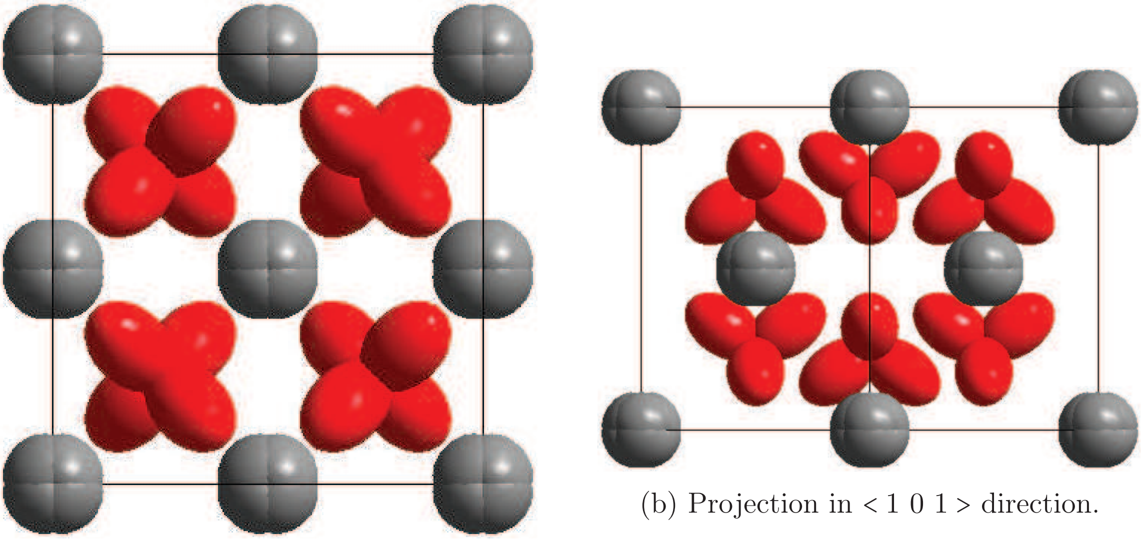

(a) Projection in $< 0\ 0\ 1 >$ direction.

(b) Projection in $< 1\ 0\ 1 >$ direction.

Figure 4.28: Representation of the average structure of the $\delta-TeO_2$ polymorph with the split atom refinement with $32f$ (x, x, x) positions. Anisotropic ADPs for Te atoms: $B_{ii} = 7.35$ Å^2, $B_{ij} = -1.29$ Å^2; and for O atoms: $B_{ii} = 12.65$ Å^2, $B_{ij} = 3.55$ Å^2.

reliability factors of the fit are improved a bit: $R_p = 4.53\%$; $R_{wp} = 5.89\%$; $R_B = 3.90\%$; $\chi^2 = 1.31$; $DW = 1.56$. The visualisation of the $\delta-TeO_2$ structure obtained with this fit is given in Fig. 4.28. We report here the projections in $< 0\ 0\ 1 >$ (Fig. 4.28a) and $< 1\ 0\ 1 >$ (Fig. 4.28b) directions. Such a model with split atoms and anisotropic thermal ellipsoids is in a perfect agreement with our MD simulations model considering qualitative description of the atoms distribution around their average positions (compare with figures 4.22b and 4.26a).

4.2.3.5 Structural units distribution

As we have shown in the Section 4.2.3.3, the short range order in modelled $\delta-TeO_2$ is very close to the one in the modelled glass. Namely, the first peak of Te–O partial PDF with a broad shoulder indicates that the coordination number of Te and O atoms is very sensitive to the R_{cutoff} value. That is why we used the same cutoff criteria as in the modelled glass ($R_{cutoff} = 2.46$ Å and $\phi_{cutoff} = 75°$) for the structural units analysis in modelled $\delta-TeO_2$. The structural units distribution for $\delta-TeO_2$ model compared to the glass model is reported in Table 4.7. The coordination numbers are $n_{TeO} = 3.66$ and $n_{OTe} = 1.83$. The Q^n_m units distribution for $\delta-TeO_2$ model is almost the same as for the glass and shows that the free- and four-fold units are the principal structural units. The population of the NBO atoms in $\delta-TeO_2$ model is very important, which is highly unusual for pure crystalline TeO_2, where all oxygen atoms are bridging and the structural units form the sinusoidal (in $\alpha-TeO_2$) or zigzag chains (in $\gamma-TeO_2$) or the double oxygen

Table 4.7: The Q_m^n units distribution and NBO atoms population in % for modelled $\delta-TeO_2$ structure compared with the modelled glass structure.

	Q_3^1	Q_3^2	Q_3^3	Q_4^2	Q_4^3	Q_4^4	Q_5^4	Q_5^5	NBO
$\delta-TeO_2$	0.92	18.75	20.95	1.16	21.18	30.32	2.31	4.28	23.3
glass	1.19	18.15	23.96	0.59	19.05	30.51	2.08	4.46	21.0

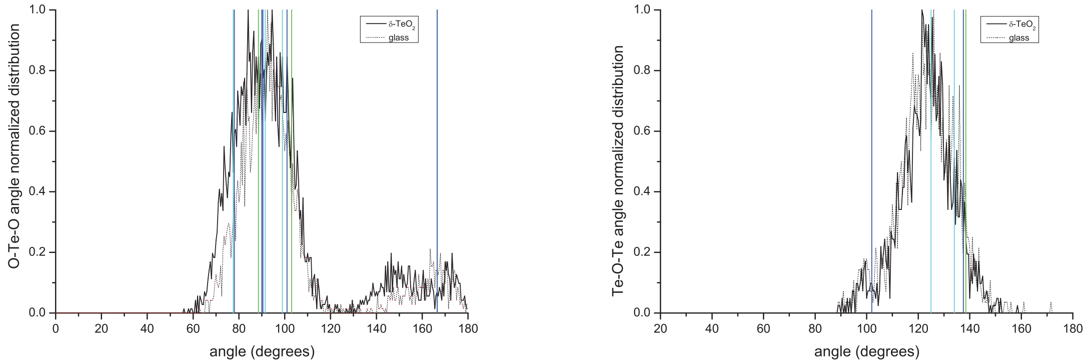

(a) O–Te–O BAD

(b) Te–O–Te BAD

Figure 4.29: Normalised BAD for modelled $\delta-TeO_2$ structure (solid line) compared to the BAD for modelled glass structure (dotted line). The vertical lines correspond to the angle values found in TeO_2 crystalline structures: $\alpha-$ (green), $\beta-$ (dark blue) and $\gamma-TeO_2$ (light blue).

bridges like in $\beta-TeO_2$.

The O–Te–O and Te–O–Te BAD are given in Fig. 4.29. Once again the resemblance with the glass structure is clearly indicated. Hence, broad O–Te–O BAD comprises all characteristic angles for $\alpha-$, $\beta-$ and $\gamma-TeO_2$ and Te–O–Te BAD indicates rather a corner-sharing character of polyhedra connection and a small amount of edge-sharing polyhedra (double oxygen bridges).

4.2.3.6 Structural units interconnection.

Let us now closely inspect the obtained $\delta-TeO_2$ model. Fig. 4.30 reports the slices of the simulation box in $a-$, $b-$ and $c-$axis projections. Each slice was cut in such a way to contain all Te atoms lying on the one face of FCC lattice, so that the width of each slice is about 5 Å. The criteria for the bond definition were chosen as for Q_m^n units distribution calculation, *i.e.* R_{cutoff} = 2.46 Å and ϕ_{cutoff} = 75°. The bonds are represented as follows: the short Te–O bonds (< 2.02 Å) are represented in solid yellow lines, the intermediate Te–O bonds (2.02 Å< d < 2.2 Å) in dashed yellow lines and the long Te–O bonds (> 2.2 Å) in dashed dark green lines. (The "isolated" TeO_x units in Fig. 4.30 are not really isolated, they are connected with units in other (parallel) slices. It is clear from Table 4.7 that

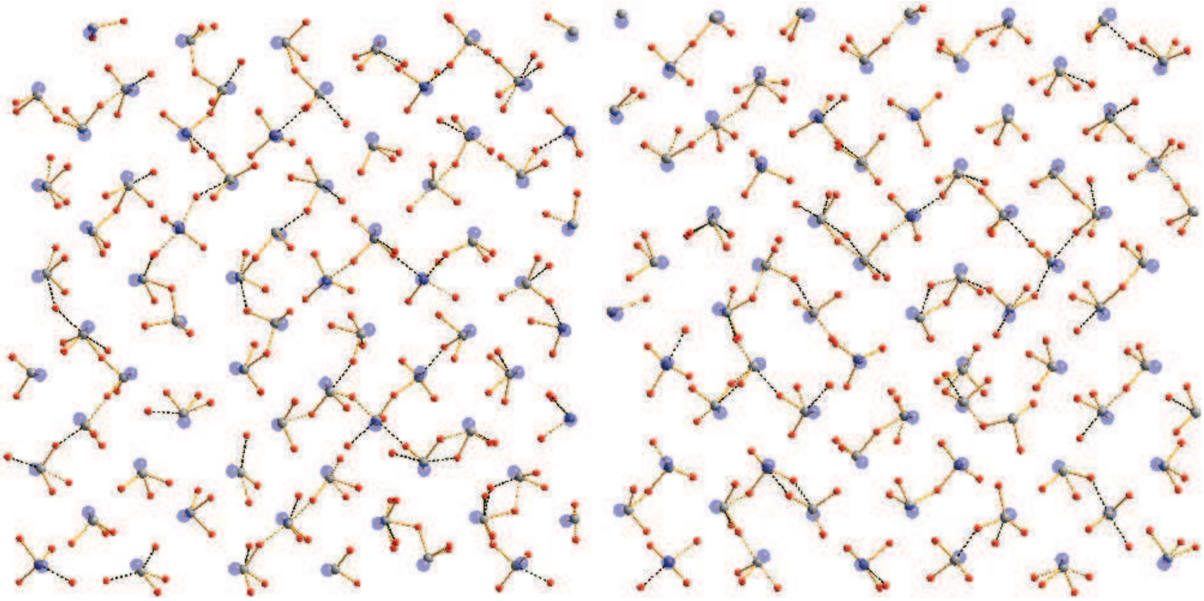

(a) Slice in the < 1 0 0 > direction.

(b) Slice in the < 0 1 0 > direction.

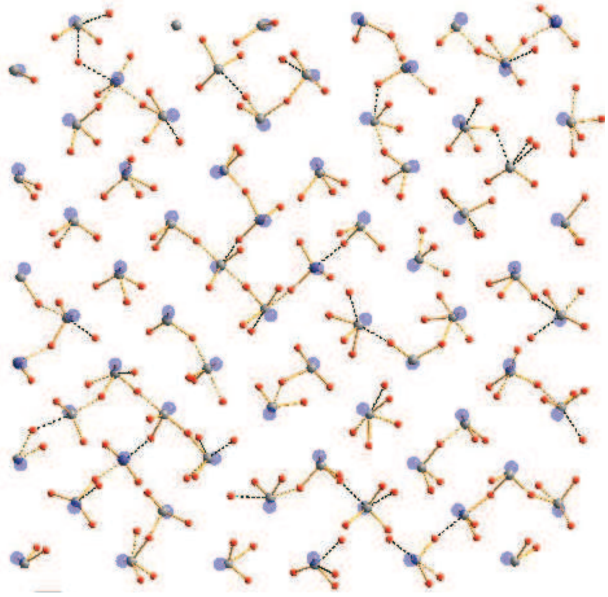

(c) Slice in the < 0 0 1 > direction.

Figure 4.30: The slices of the final configuration cut in different directions. Each slice has a width of about 5 Å.

there is no true isolated Q_m^0 structural units. The "isolated" Te atoms on the borders of simulation box are actually coordinated with oxygen atoms *via* periodic boundaries conditions.)

As we can see, the units interconnection is indeed very poor. In each projection we find the fragments of the short chains and a very few of double oxygen bridges. Fig. 4.30 shows that there is no preferred crystallographic direction, where the units are more or less interconnected. The chains consist of four structural units in average and of eight structural units maximum. One can note that these chains almost always contain the long and weak Te–O bonds.

This can explain the instability of the $\delta-TeO_2$ polymorph towards re-crystallisation with heating into $\gamma-$ or $\alpha-TeO_2$ polymorphs. Possibly, a very subtle changes in temperature are required to reinforce the existing weak bonds in the chains germs and to construct the longer chain linkages as in more stable $\gamma-$ and $\alpha-TeO_2$ polymorphs.

4.2.3.7 The role of tellurium LP.

It was discussed in Section 4.1.5 that the tellurium LP plays a very important role in our modelled glass structure. Firstly, we define with its help wether the oxygen atom is bonded to a given tellurium atom and, secondly, the structural units have to take into account its steric effect when arranging one with respect to another.

Let us now consider the role of the tellurium LP in the modelled $\delta-TeO_2$. Fig. 4.31a reports the LP–LP partial PDF $G_{LPLP}(r)$ compared with Te–Te partial PDF $G_{TeTe}(r)$. They drastically differ one from another. Surely, the peak positions of the both functions correspond to the FCC lattice (a = 5.602 Å) formed by tellurium atoms, but the resolution of the $G_{LPLP}(r)$ peaks is significantly better. Its peaks are thin and intense indicating a much better ordering of the LPs than of Te cores. Indeed, the calculated ADP for tellurium LPs is $< B_{LP} >= 2.58$ Å^2, which is almost four times less than $< B_{Te} >$. Apparently, the cation FCC lattice is not so disordered as we could conclude considering only tellurium cores, but ordered in such a way that tellurium shells form a better defined FCC lattice. The $c-$axis projection of the average structure with only Te shells and O cores is given in Fig. 4.32.

In contrast, the O(LP)–O(LP) partial PDF does not really differs from the O(core)–O(core) partial PDF as shown in Fig. 4.31c. If we consider the Te(LP)–O pair correlation function (Fig. 4.31b), we observe the shift of the most intensive peaks to the larger r values, which corresponds to the shift of tellurium LPs with respect to tellurium cores at 0.4–0.6 Å distances.

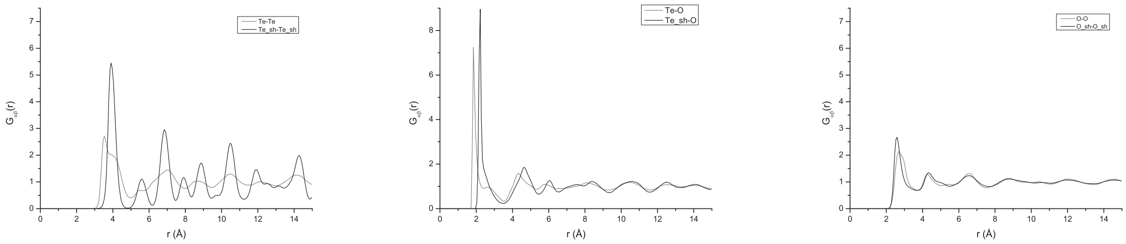

(a) Te_{sh}–Te_{sh} partial PDF. (b) Te_{sh}–O partial PDF. (c) O_{sh}–O_{sh} partial PDF.

Figure 4.31: Partial PDFs for pairs containing Te or O shells compared to core-core partial PDFs.

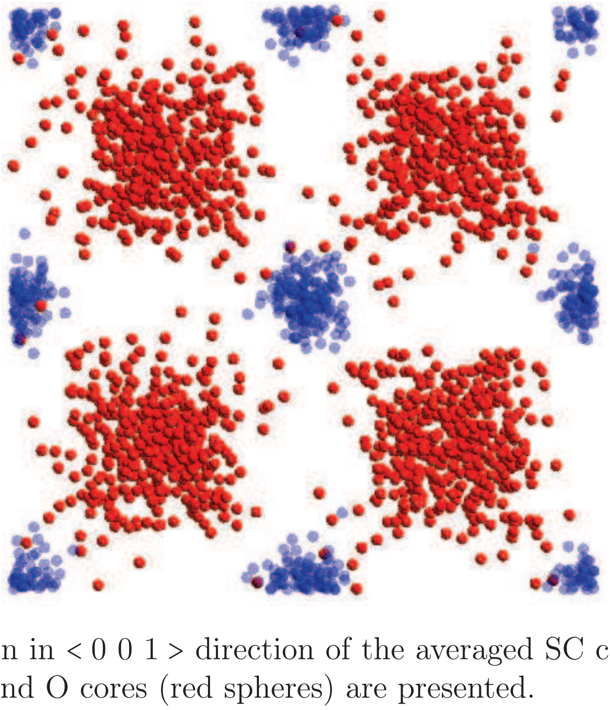

Figure 4.32: Projection in < 0 0 1 > direction of the averaged SC configuration. Only Te shells (blue spheres) and O cores (red spheres) are presented.

4.2.4 Conclusions

In this chapter we presented for the first time a detailed study of the $\delta-TeO_2$ polymorph based on the experimental and theoretical approaches. The X-ray diffraction pattern and PDF from X-ray diffuse scattering signal were obtained for the $\delta-TeO_2$ sample without any secondary phases. The Rietveld refinement of the X-ray diffraction pattern considering the perfect fluorite model gives very important ADPs for both Te and O atoms. In addition, the perfect fluorite model is inconsistent as it gives overestimated values for the shortest Te–O and Te–Te bonds (2.46 Å and 4.02 Å respectively). The use of the split atoms model improves the refinement reliability factors and decreases significantly the isotropic ADPs as well as bond lengths values. The total PDF from X-ray diffuse scattering signal gives a more precise insight on the interatomic distances. It exhibits the first peaks at 1.9 Å 2.8 Å and 3.65 Å, which can be unambiguously attributed to the shortest Te–O, O–O and Te–Te distances respectively.

We, then, performed MD simulations of the $\delta-TeO_2$ polymorph. The obtained model is in a very good agreement with experimental data: the calculated ADPs for Te atoms are in perfect agreement with experimental one, although the ADPs for O atoms are underestimated. The calculated PDF accords very well with experimental one.

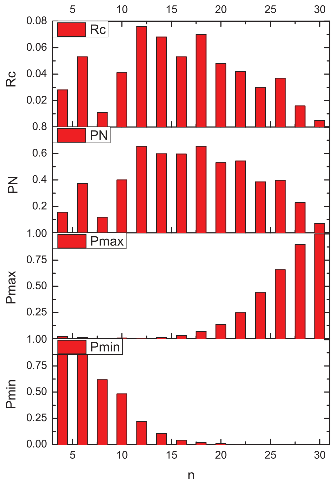

Figure 4.33: Primitive rings statistics for $\delta-TeO_2$ polymorph. $R_C(n)$ is the number of rings of n nodes per cell in the material, $P_N(n)$ is the proportion of nodes, which form at least one ring of size n, and $P_{max}(n)$ and $P_{min}(n)$ are the probabilities, that a ring with n nodes represents respectively the longest or the shortest ring for given node.

In general, $\delta-TeO_2$ polymorph seems to be very similar to $\beta-Bi_2Te_4O_{11}$ phase: in both systems the cations form a crystalline (FCC) lattice and the anions exhibit a large displacement disorder with respect to the tetrahedral sites. Also, the both phases consist of mainly TeO_3 and TeO_4 polyhedra connected in a coner-sharing way. However, the disorder in $\delta-TeO_2$ polymorph is more important for both type of atoms. In addition, a large concentration of small rings was found in $\beta-Bi_2Te_4O_{11}$ phase in [17]. If we consider the rings statistics analysis for $\delta-TeO_2$ (Fig. 4.33), we find that the distribution of the rings of different size is very similar to the one in the glass and does not present the evidences of the high concentration of small rings. We should note, however, that we used a different way of rings statistics calculations than the authors in [17].

We studied in detail the distribution of Te and O atoms around their average positions for our $\delta-TeO_2$ model. The tellurium atoms are distributed almost isotropically and form a spherical distribution around $4c$ (0, 0, 0) position. Whereas the distribution of the oxygen atoms is more complex and can be described by anisotropic thermal ellipsoids with the origins at $32f$ positions (x, x, x). The consideration of the anisotropic ADPs in Rietveld refinement slightly improves the reliability parameters and gives the structure model, which is in perfect agreement with the model obtained by means of MD simulations.

The close inspection of the obtained model showed that the connectivity between structural units is very weak. In contrast to $\alpha-$, $\beta-$ and $\gamma-TeO_2$ pure polymorphs, our $\delta-TeO_2$ model has a large proportion of the NBO atoms, which is completely similar to the modelled glass structure. This leads to formation of short and terminated chains. These chains are often formed with the help of long (> 2.2 Å) and weak Te–O bonds, which indicates the instability of such structural features. This means that very subtle changes in temperature are sufficient for initiating the structural rearrangement.

The LPs of tellurium atoms play a surprising role in our $\delta-TeO_2$ model. We found that the Te LPs are rather well organised in crystalline FCC lattice in contrast to Te cores. The ration of ADPs, B_{iso}, for Te and O atoms is almost four times smaller for Te LPs than for Te cores. Hence, apparently, the cation sub-lattice is not so disordered as we could think, but it is ordered in such a way to form a fairly well-ordered Te LPs sub-lattice.

We presented here a detailed analysis of the modelled $\delta-TeO_2$ polymorph. However, there are still a lot of open questions about this phase. We recall here that this phase has never been obtained from the pure TeO_2 glass but always from slightly modified glass. The understanding of the role of the modifiers in $\delta-TeO_2$ crystallisation requires primarily a thorough experimental study. For example, this could be the X-ray total scattering experiments for the $\delta-TeO_2$ samples prepared from glasses with different modifiers (*e.g.* WO_3, Nb_2O_5) and different modifiers content. On the other hand, the MD simulations of $\delta-TeO_2$ shows that this phase exists within the pure TeO_2 system. Hence, this indicates the processing side of the problem of $\delta-TeO_2$ formation from the pure glass.

General conclusion

This work presents the structural study of the pure TeO_2 glass and disordered $\delta-TeO_2$ phase by means of experimental and atomistic simulations methods. The used experimental techniques are: X-ray diffraction, X-ray total scattering and Raman spectroscopy. For the structural modelling we use molecular dynamics simulations, which require the derivation of the empirical interatomic potentials for TeO_2 system.

First of all, we performed the study on the synthesis of $\gamma-$ and $\delta-TeO_2$ polymorphs. These phases are very difficult to synthesise as pure as possible, *i.e.* without any secondary phases. We optimised the synthesis parameters in order to improve the quality of the crystallised samples. We demonstrated that the homogenisation of the glassy samples improved the crystallised samples quality. We observed the effect of homogenisation of glassy samples is crucial for the purity of the crystallised phases. According to that we proposed that different parts of the sample crystallise in different phases: the powder grains of pure glass directly crystallise in $\alpha-TeO_2$ polymorph, while the grains rich in modifier crystallise in $\delta-TeO_2$ or $\gamma-TeO_2$ polymorph. The sample of pure $\delta-TeO_2$ phase obtained by crystallisation of homogenised glass was then used for the X-ray total scattering experiment.

The problem of interatomic potentials derivation led us to studying of the local environment of Te atom in pure $\alpha-$, $\beta-$ and $\gamma-TeO_2$ and some mixed TeO_2-based crystalline structures. In these structures tellurium atom has different oxygen atoms environment. Consideration of the different crystalline structures helps to understand how the interaction model effects the TeO_x units modelling results. In such a manner, we showed by means of empirical methods that the electronic LP of tellurium atom is responsible for distorted rutile-type structure of $\alpha-TeO_2$ and the formation of TeO_4 disphenoid with two equal short bonds and two equal elongated bonds. The $\gamma-TeO_2$ consists of asymmetrical TeO_{3+1} units with three short Te–O bonds and one elongated bond. We showed that in this case, the oxygen atoms polarisability in potential model plays an important role and is responsible for a strong asymmetry in Te^{IV} atoms environment. We found out that the use of an anharmonic term in Te(core)–Te(shell) interaction allows a better modelling of Te^{IV} atom coordination in various mixed TeO_2-based compounds.

In such a way, we derived a simple but nontrivial potential model, in which the short-range interatomic interaction in the core-shell model frameworks is set between the Te atom core and O atom shell and the core-shell model for Te atom uses an anharmonic spring potential form. This approach is reported for the first time in the literature and works well for different TeO_2-based compounds. The core-shell model for O atom is used in conventional harmonic spring form.

The application of the derived potentials to 19 TeO_2-based compounds (pure and mixed) demonstrated their high transferability. The cell parameters and TeO_x basic units are reproduced very well for all the investigated structures except K_2TeO_3 and $K_2Te_4O_{12}$ structures. Generally, our potentials underestimate short Te–O bonds and overestimate intermediate bonds. The subtle difference between TeO_4 unit in $\alpha-TeO_2$ and TeO_{3+1} unit in $\gamma-TeO_2$ is well reproduced, which makes our IAPs appropriate for MD simulation glass modelling.

We considered the effect of the Te atom polarisation on TeO_x structural unit configuration. The core-shell displacement for Te atom varies in 0.394–0.719 Å interval. Generally, the stronger the polarisation of Te atom, the lower its coordination and the stronger the Te–O bonds (TeO_3 tp in Cs_2TeO_3, for example), whereas the weaker the polarisation of Te atom, the higher its coordination (5 to 6) and the weaker some of the Te–O bonds.

The derived potentials were applied to MD simulations of pure TeO_2 glass and disordered $\delta-TeO_2$ phase structures. The glass structure model was obtained for a system containing 672 TeO_2 units and with a total simulation time of about 350 ps. We considered our glass structure model as realistic as the calculated total PDF is in a good agreement with the experimental one obtained by neutron diffraction experiment. In order to analyse correctly the glass structure model, we established a criterion that allows us to precisely define the first coordination sphere of Te atom by explicitly taking into account the Te stereochemically active electronic LP. Indeed, the glass structure model has a very broad bond lengths distribution with a large variations of Te–O bond lengths so that there is no clear criterion to define the usual cutoff radius. Our criterion is the angle between oxygen atom inside the Te coordination sphere of the radius R_{cutoff} = 2.46 Å, Te core and Te shell (the LP) and it was set to 75°.

The modelled glass network is described as poorly connected, with terminated chains and large ($n \geq 10$) rings. The Q_n^m units distribution is broad and presents different units types: Q_3^1, Q_3^2, Q_3^3, Q_4^2, Q_4^3, Q_4^4, Q_5^4, Q_5^5. The three- and four-coordinated Te atoms make up the largest contribution into Q_n^m units population, which leads to the Te coordination number decreased with respect to pure crystalline structures (n_{TeO} = 3.63). The units interconnection has rather corner-sharing character, and the edge-sharing polyhedra are almost absent. We demonstrated that the large number of NBO (21%) and stereochemical effect of Te electronic LP lead to such a badly connected TeO_2 glass network.

In this work we also presented for the first time a detailed study of the $\delta-TeO_2$ polymorph based on the experimental and theoretical approaches. The experimental study included the X-ray diffraction, X-ray total scattering and Raman spectroscopy characteristics of the pure $\delta-TeO_2$ sample obtained in this work. The Rietveld refinement of the X-ray diffraction pattern considering the perfect fluorite model gives very important ADPs for both Te and O atoms. The perfect fluorite model implies that the shortest Te–O and Te–Te bond lengths are equal to 2.46 Å and 4.02 Å respectively. However, according to X-ray diffuse scattering experiment, the shortest interatomic distances in $\delta-TeO_2$ have the values of 1.9 Å 2.8 Å and 3.65 Å, which can be unambiguously attributed to the shortest Te–O, O–O and Te–Te distances respectively. We performed the MD simulations in order to clarify the structure of $\delta-TeO_2$ polymorph.

The obtained MD model is in a very good agreement with experimental data. The calculated ADPs for Te atoms are in perfect agreement with those obtained with Rietveld refinement, although the ADPs for O atoms are underestimated. The average structure of $\delta-TeO_2$ polymorph can be described as follows: the cations form a crystalline (FCC) lattice and the anions exhibit a large positional disorder with respect to the tetrahedral sites. The structure consists of mainly TeO_3 and TeO_4 polyhedra connected in a conner-sharing way and the distribution of the rings of different size is very similar to the one in the glass. The tellurium atoms are distributed almost isotropically and form a spherical distribution around $4c$ (0, 0, 0) position, whereas the distribution of the oxygen atoms is more complex and can be described by anisotropic thermal ellipsoids with the origins at $32f$ positions (x, x, x). This information permitted to slightly improve the Rietveld refinement by taking into account the anisotropic ADPs.

The MD study has also demonstrated that the structure of $\delta-TeO_2$ polymorph is very similar to that of the glass and not to the $\alpha-$, $\beta-$ and $\gamma-TeO_2$ pure polymorphs. The connectivity between structural units is very weak, the model has a large proportion of NBO atoms, and the chains are short and broken. These chains are often formed with the help of long (> 2.2 Å) and weak Te–O bonds, which indicates the instability of such structural features.

Thanks to the accurate interatomic potentials developed in this work we could model the structure of the pure TeO_2 glass and the $\delta-TeO_2$ polymorph. The detailed analysis of the obtained configurations allowed us to improve the description of the glass structure and to give a deep insight into the $\delta-TeO_2$ polymorph structure for the first time.

Bibliography

[1] M. Trömel, W. Hützler, and E. Münch, "Anti-glass phases and other lanthanide tellurates with fluorite-related structures," *Journal of the Less Common Metals*, vol. 110, no. 1, pp. 421–424, 1985.

[2] B. Stehlik and L. Balak, "Crystal structure of tellurium dioxide I," *Chemical Papers*, vol. 2, no. 1, pp. 6–12, 1948.

[3] O. Lindqvist, "Refinement of the structure of α-TeO$_2$," *Acta Chem. Scand*, vol. 22, pp. 977–82, 1968.

[4] I. P. Kondratyuk, L. A. Murdoyan, Y. V. Pisarevskij, and V. I. Simonov, "Precision X-ray structural investigation of acoustooptical α-TeO$_2$ single crystals," *Kristallografiya*, vol. 32, pp. 609–617, 1987.

[5] P. A. Thomas, "The crystal structure and absolute optical chirality of paratellurite, α–TeO$_2$," *Journal of Physics C: Solid State Physics*, vol. 21, no. 25, p. 4611, 1988. [Online]. Available: http://stacks.iop.org/0022-3719/21/i=25/a=009

[6] H. Beyer, "Verfeinerung der kristallstruktur von tellurit, dem rhombischen TeO$_2$," *Zeitschrift für Kristallographie*, vol. 124, no. 3, pp. 228–237, 1967.

[7] T. Worlton and R. Beyerlein, "Structure and order parameters in the pressure-induced continuous transition in TeO$_2$," *Physical Review B*, vol. 12, no. 5, p. 1899, 1975.

[8] J. Champarnaud-Mesjard, S. Blanchandin, P. Thomas, A. Mirgorodsky, T. Merle-Mejean, and B. Frit, "Crystal structure, Raman spectrum and lattice dynamics of a new metastable form of tellurium dioxide: γ-TeO$_2$," *Journal of Physics and Chemistry of Solids*, vol. 61, no. 9, pp. 1499 – 1507, 2000. [Online]. Available: http://www.sciencedirect.com/science/article/pii/S0022369700000123

[9] S. Blanchandin, P. Marchet, P. Thomas, J. C. Champarnaud-Mesjard, B. Frit, and A. Chagraoui, "New investigations within the TeO$_2$-WO$_3$ system: phase equilibrium diagram and glass crystallisation," *Journal of Materials Science*,

vol. 34, pp. 4285–4292, 1999, 10.1023/A:1004667223028. [Online]. Available: http://dx.doi.org/10.1023/A:1004667223028

[10] A. Mirgorodsky, T. Merle-Méjean, J.-C. Champarnaud, P. Thomas, and B. Frit, “Dynamics and structure of TeO_2 polymorphs: model treatment of paratellurite and tellurite; Raman scattering evidence for new $\delta-$ and $\gamma-$phases,” *Journal of Physics and Chemistry of Solids*, vol. 61, no. 4, pp. 501 – 509, 2000. [Online]. Available: http://www.sciencedirect.com/science/article/pii/S0022369799002632

[11] S. Blanchandin, “Etude cristallochimique de quelques phases cristallisées et vitreuses appartenant aux systémes TeO_2–WO_3 et TeO_2–Nb_2O_5–Bi_2O_3,” Ph.D. dissertation, Thèse de l’Université de Limoges, 2000.

[12] M. Dutreilh-Colas, “Nouveaux matèriaux pour l’optique non linèaire : Synthése et ètude structurale de quelques phases cristallisées et vitreuses appartenant aux systémes TeO_2-Tl_2O-Ga_2O_3 et TeO_2-Tl_2O-PbO,” Ph.D. dissertation, Thèse de l’Université de Limoges, 2001.

[13] D. Hamani, “Cristallochimie de matériaux à base de dioxyde de tellure: vers un modèle structural pour étude des composés vitreux,” Ph.D. dissertation, Limoges, 2010.

[14] S. Blanchandin, P. Thomas, P. Marchet, J. Claude Champarnaud-Mesjard, and B. Frit, “Equilibrium and non-equilibrium phase diagram within the TeO_2-rich part of the TeO_2-Nb_2O_5 system,” *J. Mater. Chem.*, vol. 9, pp. 1785–1788, 1999. [Online]. Available: http://dx.doi.org/10.1039/A900788A

[15] K. Shioya, T. Komatsu, H. G. Kim, R. Sato, and K. Matusita, “Optical properties of transparent glass-ceramics in K_2O–Nb_2O_5–TeO_2 glasses,” *Journal of non-crystalline solids*, vol. 189, no. 1, pp. 16–24, 1995.

[16] Z. Szaller, L. Pöppl, G. Lovas, and I. Dodony, “Study of the formation of $Bi_2Te_4O_{11}$,” *Journal of Solid State Chemistry*, vol. 121, no. 2, pp. 251–261, 1996.

[17] O. Masson, P. Thomas, O. Durand, T. Hansen, J. Champarnaud, and D. Mercurio, “On the structure of the disordered $Bi_2Te_4O_{11}$ phase,” *Journal of Solid State Chemistry*, vol. 177, no. 6, pp. 2168 – 2176, 2004. [Online]. Available: http://www.sciencedirect.com/science/article/pii/S0022459604001070

[18] T. Sekiya, N. Mochida, A. Ohtsuka, and M. Tonokawa, “Raman spectra of $MO_{1/2}$–TeO_2(M= Li, Na, K, Rb, Cs and Tl) glasses,” *Journal of non-crystalline solids*, vol. 144, pp. 128–144, 1992.

[19] A. Mirgorodsky, M. Colas, M. Smirnov, T. Merle-Mejean, R. El-Mallawany, and P. Thomas, "Structural peculiarities and Raman spectra of TeO_2/WO_3-based glasses: A fresh look at the problem," *Journal of Solid State Chemistry*, vol. 190, no. 0, pp. 45 – 51, 2012. [Online]. Available: http://www.sciencedirect.com/science/article/pii/S0022459612001028

[20] S. Sakida, S. Hayakawa, and T. Yoko, "Part 1. ^{125}Te NMR study of tellurite crystals," *Journal of non-crystalline solids*, vol. 243, no. 1, pp. 1–12, 1999.

[21] ——, "Part 2. ^{125}Te NMR study of M_2O-TeO_2 (M= Li, Na, K, Rb and Cs," *Journal of non-crystalline solids*, vol. 243, no. 1, pp. 13–25, 1999.

[22] J. C. McLaughlin, S. L. Tagg, J. W. Zwanziger, D. R. Haeffner, and S. D. Shastri, "Structure of tellurite glass: A combined NMR, neutron diffraction, and X-ray diffraction study," *Journal of Non-Crystalline Solids*, vol. 274, no. 1, pp. 1–8, 2000.

[23] J. C. McLaughlin, S. L. Tagg, and J. W. Zwanziger, "The structure of alkali tellurite glasses," *The Journal of Physical Chemistry B*, vol. 105, no. 1, pp. 67–75, 2001. [Online]. Available: http://pubs.acs.org/doi/abs/10.1021/jp0025779

[24] J. W. Zwanziger, J. C. McLaughlin, and S. L. Tagg, "Sodium distribution in sodium tellurite glasses probed with spin-echo NMR," *Physical Review B - Condensed Matter and Materials Physics*, vol. 56, no. 9, pp. 5243–5249, 1997.

[25] U. Hoppe, I. Gugov, H. Bürger, P. Jóvári, and A. Hannon, "Structure of tellurite glasses – Effects of K_2O or P_2O_5 additions studied by diffraction," *Journal of Physics Condensed Matter*, vol. 17, no. 15, pp. 2365–2386, 2005.

[26] F. Pietrucci, S. Caravati, and M. Bernasconi, "TeO_2 glass properties from first principles," *Phys. Rev. B*, vol. 78, p. 064203, Aug 2008. [Online]. Available: http://link.aps.org/doi/10.1103/PhysRevB.78.064203

[27] E. R. Barney, A. C. Hannon, D. Holland, N. Umesaki, M. Tatsumisago, R. G. Orman, and S. Feller, "Terminal oxygens in amorphous TeO_2," *The Journal of Physical Chemistry Letters*, pp. 2312–2316, 2013.

[28] H. Niida, T. Uchino, J. Jin, S.-H. Kim, T. Fukunaga, and T. Yoko, "Structure of alkali tellurite glasses from neutron diffraction and molecular orbital calculations," *Journal of Chemical Physics*, vol. 114, no. 1, pp. 459–467, 2001.

[29] T. Uchino and T. Yoko, "Ab initio cluster model calculations on the vibrational frequencies of teo< sub> 2</sub> glass," *Journal of non-crystalline solids*, vol. 204, no. 3, pp. 243–252, 1996.

[30] T. Uchino, S.-H. Kim, T. Yoko, and T. Fukunaga, "Medium-range structure of teo2 glass from molecular orbital calculations," *Nippon seramikkusu kyokai gakujutsu ronbunshi*, vol. 105, no. 3, pp. 201–205, 1997.

[31] T. Sekiya, N. Mochida, A. Ohtsuka, and M. Tonokawa, "Normal vibrations of two polymorphic forms of teo2 crystals and assignments of raman peaks of pure teo2 glass," *Nippon seramikkusu kyokai gakujutsu ronbunshi*, vol. 97, no. 12, pp. 1435–1440, 1989.

[32] W. H. Zachariasen, "The atomic arrangement in glass," *Journal of the American Chemical Society*, vol. 54, no. 10, pp. 3841–3851, 1932.

[33] S. Neov, V. Kozhukharov, I. Gerasimova, K. Krezhov, and B. Sidzhimov, "A model for structural recombination in tellurite glasses," *Journal of Physics C: Solid State Physics*, vol. 12, no. 13, p. 2475, 1979.

[34] Y. Himei, A. Osaka, T. Nanba, and Y. Miura, "Coordination change of Te atoms in binary tellurite glasses," *Journal of non-crystalline solids*, vol. 177, pp. 164–169, 1994.

[35] C. Becker, S. Tagg, J. Huffman, and J. Zwanziger, "Crystal structures of potassium tetratellurite, $K_2Te_4O_9$, and potassium ditellurite, $K_2Te_2O_5$, and structural trends in solid alkali tellurites," *Inorganic chemistry*, vol. 36, no. 24, pp. 5559–5564, 1997.

[36] J. McLaughlin and J. Zwanziger, "Modeling glasses using the reverse Monte Carlo algorithm: addition of nuclear magnetic resonance and expanded coordination number constraints," *Journal of Molecular Graphics and Modelling*, vol. 17, no. 5, pp. 275–284, 1999.

[37] [Online]. Available: http://www.ucl.ac.uk/klmc/Potentials/Library/catlow.lib

[38] H. Matsumoto, T. Mabuchi, Y. Shigesato, and I. Yasui, "Structure analysis of Zno–TeO_2 glasses by means of neutron diffraction and molecular dynamics," *Japanese Journal of Applied Physics*, vol. 35, no. Part 1, No. 2A, pp. 694–698, 1996. [Online]. Available: http://jjap.jsap.jp/link?JJAP/35/694/

[39] C. R. A. Catlow, R. James, W. C. Mackrodt, and R. F. Stewart, "Defect energetics in α-Al_2O_3 and rutile TiO_2," *Physical Review B (Condensed Matter)*, vol. 25, pp. 1006–1026, Jan. 1982.

[40] C. M. Freeman and C. R. A. Catlow, "A computer modelling study of defect and dopant states in SnO_2," *Journal of Solid State Chemistry*, vol. 85, no. 1, pp.

65 – 75, 1990. [Online]. Available: http://www.sciencedirect.com/science/article/B6WM2-4GSCH0T-C/2/ba8ce00947e2fb234fa8090ef8e95167

[41] D.J.Binks, "Computational modelling of zinc oxide and related oxide ceramics," Ph.D. dissertation, University of Surrey, 1994.

[42] M. Sanders, M. Leslie, and C. Catlow, "Interatomic potentials for SiO_2," *Journal of the Chemical Society, Chemical Communications*, no. 19, pp. 1271–1273, 1984.

[43] B. G. Dick and A. W. Overhauser, "Theory of the dielectric constants of alkali halide crystals," *Phys. Rev.*, vol. 112, pp. 90–103, Oct 1958. [Online]. Available: http://link.aps.org/doi/10.1103/PhysRev.112.90

[44] J. D. Gale, "The general utility lattice program v.3.1 users manual." [Online]. Available: http://projects.ivec.org/gulp/help/manuals.html

[45] M. C. Wojcik and K. Hermansson, "The problem of the detaching shell in the shell model potential for oxides," *Chemical Physics Letters*, vol. 289, no. 1, pp. 211 – 218, 1998. [Online]. Available: http://www.sciencedirect.com/science/article/pii/S0009261498004345

[46] B. Loopstra and K. Goubitz, "The structures of four caesium tellurates," *Acta Crystallographica Section C: Crystal Structure Communications*, vol. 42, no. 5, pp. 520–523, 1986.

[47] J. D. Gale, "Gulp: A computer program for the symmetry-adapted simulation of solids," *J. Chem. Soc., Faraday Trans.*, vol. 93, no. 4, pp. 629–637, 1997.

[48] H. Ogi, M. Fukunaga, M. Hirao, and H. Ledbetter, "Elastic constants, internal friction, and piezoelectric coefficient of α-TeO_2," *Phys. Rev. B*, vol. 69, p. 024104, Jan 2004. [Online]. Available: http://link.aps.org/doi/10.1103/PhysRevB.69.024104

[49] Q.-J. Liu, Z.-T. Liu, L.-P. Feng, and H. Tian, "First-principles study of structural, elastic, electronic, and optical properties of α-TeO_2," *Physica B: Condensed Matter*, vol. 405, no. 15, pp. 3159 – 3163, 2010. [Online]. Available: http://www.sciencedirect.com/science/article/pii/S0921452610003960

[50] M. Born and K. Huang, *Dynamical theory of crystal lattices.* Clarendon Press Oxford, 1954.

[51] J. F. Nye, *Physical Properties of Cristals: Their Representation by Tensors and Matrices.* Oxford University Press, 1985.

[52] M. P. Allen and D. J. Tildesley, *Computer simulation of liquids.* Oxford university press, 1989.

[53] J. M. Haile, *Molecular dynamics simulation: elementary methods.* John Wiley & Sons, Inc., 1992.

[54] B. J. Alder and T. Wainwright, "Studies in molecular dynamics. I. general method," *The Journal of Chemical Physics*, vol. 31, p. 459, 1959.

[55] B. Alder and T. Wainwright, "Phase transition for a hard sphere system," *The Journal of Chemical Physics*, vol. 27, no. 5, pp. 1208–1209, 1957.

[56] A. Rahman, "Correlations in the motion of atoms in liquid argon," *Physical Review*, vol. 136, no. 2A, p. A405, 1964.

[57] [Online]. Available: http://www.ccp5.ac.uk/DL_POLY_CLASSIC/

[58] L. Verlet, "Computer 'experiments' on classical fluids. ii. equilibrium correlation functions," *Physical Review*, vol. 165, no. 1, p. 201, 1968.

[59] P. J. Mitchell and D. Fincham, "Shell model simulations by adiabatic dynamics," *Journal of Physics: Condensed Matter*, vol. 5, no. 8, p. 1031, 1993. [Online]. Available: http://stacks.iop.org/0953-8984/5/i=8/a=006

[60] P. J. D. Lindan and M. J. Gillan, "Shell-model molecular dynamics simulation of superionic conduction in CaF_2," *Journal of Physics: Condensed Matter*, vol. 5, no. 8, p. 1019, 1993. [Online]. Available: http://stacks.iop.org/0953-8984/5/i=8/a=005

[61] S. Adelman and J. Doll, "Generalized langevin equation approach for atom/solid-surface scattering: General formulation for classical scattering off harmonic solids," *The Journal of Chemical Physics*, vol. 64, no. 6, pp. 2375–2388, 1976.

[62] H. C. Andersen, "Molecular dynamics simulations at constant pressure and/or temperature," *The Journal of chemical physics*, vol. 72, no. 4, pp. 2384–2393, 1980.

[63] D. J. Evans and O. Morriss, "Non-newtonian molecular dynamics," *Computer Physics Reports*, vol. 1, no. 6, pp. 297–343, 1984.

[64] H. J. Berendsen, J. P. M. Postma, W. F. van Gunsteren, A. DiNola, and J. Haak, "Molecular dynamics with coupling to an external bath," *The Journal of chemical physics*, vol. 81, p. 3684, 1984.

[65] W. G. Hoover, "Canonical dynamics: Equilibrium phase-space distributions," *Physical Review A*, vol. 31, no. 3, p. 1695, 1985.

[66] P. H. Hünenberger, "Thermostat algorithms for molecular dynamics simulations," in *Advanced Computer Simulation*. Springer, 2005, pp. 105–149.

[67] Y. Andoh, N. Yoshii, K. Fujimoto, K. Mizutani, H. Kojima, A. Yamada, S. Okazaki, K. Kawaguchi, H. Nagao, K. Iwahashi *et al.*, "MODYLAS: A highly parallelized general-purpose molecular dynamics simulation program for large-scale systems with long-range forces calculated by fast multipole method (FMM) and highly scalable fine-grained new parallel processing algorithms," *Journal of Chemical Theory and Computation*, 2013.

[68] M. Born and T. von Kármán, "On fluctuations in spatial grids," *Physikalische Zeitschrift*, vol. 13, no. 297-309, p. 18, 1912.

[69] B. E. Warren, *X-ray Diffraction*. Dover Publications, 1969.

[70] H. Rietveld, "A profile refinement method for nuclear and magnetic structures," *Journal of applied Crystallography*, vol. 2, no. 2, pp. 65–71, 1969.

[71] R. A. Young, "The Rietveld method," *Crystal research and technology*, vol. 30, no. 4, 1995.

[72] V. Petricek, M. Dusek, and L. Palatinus, "Jana2006. Structure determination software programs," 2000.

[73] J. Rodriguez-Carvajal, "Fullprof program: Rietveld pattern matching analysis of powder patterns," *ILL, Grenoble*, 1990.

[74] O. Durand, "Propriétés structurales et vibrationnelles des phases désordonnées dans le système TeO_2-Bi_2O_3," Ph.D. dissertation, Thèse de l'Université de Limoges, 2006.

[75] R. Mayet, "Propriétés structurales de nanocristaux d'oxydes métalliques: utilisation de la diffusion total des rayon X et des calculs quantiques," Ph.D. dissertation, Université de Limoges, 2008.

[76] L. Portal, "Synthèse et caractérisation structurale de nanocristaux d'oxydes métalliques," Ph.D. dissertation, Université de Limoges, 2013.

[77] T. Egami and S. J. Billinge, *Underneath the Bragg peaks: structural analysis of complex materials*. Elsevier, 2003, vol. 16.

[78] S. J. Billinge and M. Kanatzidis, "Beyond crystallography: the study of disorder, nanocrystallinity and crystallographically challenged materials with pair distribution functions," *Chemical communications*, no. 7, pp. 749–760, 2004.

[79] M. T. Dove and D. A. Keen, “Atomic structure of disordered materials,” *NATO ASI Series C: mathematical and physical sciences*, vol. 543, pp. 371–388, 1999.

[80] F. Frey, “Diffuse scattering from disordered crystals,” *Acta Crystallographica Section B: Structural Science*, vol. 51, no. 4, pp. 592–603, 1995.

[81] O. Masson and P. Thomas, “Exact and explicit expression of the atomic pair distribution function as obtained from X-ray total scattering experiments,” *Journal of Applied Crystallography*, vol. 46, no. 2, pp. 461–465, 2013.

[82] O. Masson, “Xtsscan.”

[83] ——, “Corrections.”

[84] C. V. Raman, “A new radiation,” *Indian Journal of physics*, vol. 2, pp. 387–398, 1928.

[85] L. Mandelstam and G. Landsberg, “Eine neue Erscheinung bei der Lichtzerstreuung in Kristallen,” *Naturwissenschaften*, vol. 16, pp. 557–558, Jul. 1928.

[86] A. Smekal, “Zur quantentheorie der dispersion,” *Naturwissenschaften*, vol. 11, no. 43, pp. 873–875, 1923.

[87] F. A. Cotton, *Chemical applications of group theory.* John Wiley & Sons, 2008.

[88] A. Oufkir, A. Ramdani, P. Marchet, P. Thomas, J. C. Champaranaud-Mesjard, and B. Frit, “Equilibrium an non-equilibrium phase diagram within the TeO_2-rich part of the TeO_2-PbO system,” *Ann. Chim. Sci. Mat.*, no. 25, pp. S259–S262, 2000.

[89] S.-H. Kim, T. Yoko, and S. Sakka, “Nonlinear optical properties of TeO_2-based glasses: La_2O_3-TeO_2 binary glasses,” *Journal of the American Ceramic Society*, vol. 76, no. 4, pp. 865–869, 1993.

[90] A. Berthereau, Y. Le Luyer, R. Olazcuaga, G. Le Flem, M. Couzi, L. Canioni, P. Segonds, L. Sarger, and A. Ducasse, “Nonlinear optical properties of some tellurium (IV) oxide glasses,” *Materials research bulletin*, vol. 29, no. 9, pp. 933–941, 1994.

[91] F. Folger, “Crystal structure of lithium tellurate (IV),” *Zeitschrift fuer Anorganische und Allgemeine Chemie*, vol. 411, no. 2, pp. 103–110, 1975.

[92] L. Andersen, V. Langer, A. Stromberg, and D. Stromberg, “The structure of K_2TeO_3 – an experimental and theoretical study,” *Acta Crystallographica Section B: Structural Science*, vol. 45, no. 4, pp. 344–348, 1989.

[93] R. Masse, J. Guitel, and I. Tordjman, "Preparation chimique et structure cristalline des tellurites de sodium et d'argent: Na_2TeO_3, Ag_2TeO_3," *Materials Research Bulletin*, vol. 15, no. 4, pp. 431–436, 1980.

[94] M. Weil, "Redetermination of $MgTe_2O_5$," *Acta Crystallographica Section E: Structure Reports Online*, vol. 61, no. 11, pp. i237–i239, 2005.

[95] M. Weil and B. Stoger, "A non-twinned polymorph of $CaTe_2O_5$ from a hydrothermally grown crystal," *Acta Crystallographica Section C: Crystal Structure Communications*, vol. 64, no. 9, pp. i79–i81, 2008.

[96] M. Kocak, C. Platte, and M. Troemel, "Barium hexaoxoditellurate(IV,VI): oxygen coordination number 5 at tetravalent tellurium," *Acta Crystallographica*, vol. B35(6), pp. 1439–1441, 1979.

[97] S. Tagg, J. Huffman, and J. Zwanziger, "Crystal structure and sodium environments in sodium tetratellurite, $Na_2Te_4O_9$, and sodium tellurite, Na_2TeO_3, by X-ray crystallography and sodium-23 NMR," *Chemistry of materials*, vol. 6, no. 10, pp. 1884–1889, 1994.

[98] W. Klein, J. Curda, E.-M. Peters, and M. Jansen, "Neue silber (I)-oxotellurate (IV/VI)," *Zeitschrift für anorganische und allgemeine Chemie*, vol. 631, no. 13-14, pp. 2893–2899, 2005.

[99] N. Barrier, S. Malo, O. Hernandez, M. Hervieu, and B. Raveau, "The mixed valent tellurate $SrTe_3O_8$: Electronic lone pair effect of Te^{4+}," *Journal of Solid State Chemistry*, vol. 179, no. 11, pp. 3484–3488, 2006.

[100] F. Daniel, J. Moret, M. Maurin, and E. Philippot, "Structure cristalline d'un oxotellurate mixte, Te^{IV} et Te^{VI}: $K_2Te^{IV}Te^{VI}{}_3O_{12}$. Pentacoordination du tellure(IV) par les atomes d'oxygène," *Acta Crystallographica Section B*, vol. 34, no. 6, pp. 1782–1786, Jun 1978. [Online]. Available: http://dx.doi.org/10.1107/S0567740878006706

[101] H. Mayer and M. Weil, "Synthesis and crystal structure of $Te_3O_3(PO_4)_2$, a compound with 5-fold coordinate tellurium(IV) [Synthese und kristallstruktur von $Te_3O_3(PO_4)_2$, einer verbindung mit funffach koordiniertem tellur(IV)]," *Zeitschrift fur Anorganische und Allgemeine Chemie*, vol. 629, no. 6, pp. 1068–1072, 2003.

[102] T. Siritanon, J. Li, J. K. Stalick, R. T. Macaluso, A. W. Sleight, and M. Subramanian, "$CsTe_2O_{6-x}$: Novel mixed-valence tellurium oxides with framework-deficient pyrochlore-related structure," *Inorganic chemistry*, vol. 50, no. 17, pp. 8494–8501, 2011.

[103] H. Rossell, M. Leblanc, G. Ferey, D. Bevan, D. Simpson, and M. Taylor, “On the crystal structure of $Bi_2Te_4O_{11}$,” *Australian Journal of Chemistry*, vol. 45, no. 9, pp. 1415–1425, 1992.

[104] V. M. Trömel and T. Scheller, “Die kristallstruktur von $Co_6Te_5O_{16}$,” *Zeitschrift für anorganische und allgemeine Chemie*, vol. 427, no. 3, pp. 229–234, 1976.

[105] C. Platte and M. Tromel, “Nickelditellurat (IV): Sauerstoffkoordinationszahl funf am vierwertigen tellur,” *Acta Crystallographica Section B: Structural Crystallography and Crystal Chemistry*, vol. 37, no. 6, pp. 1276–1278, 1981.

[106] S. M. Woodley, P. D. Battle, J. D. Gale, and C. R. A. Catlow, “The prediction of inorganic crystal structures using a genetic algorithm and energy minimisation,” *Physical Chemistry Chemical Physics*, vol. 1, no. 10, pp. 2535–2542, 1999.

[107] T. S. Bush, J. D. Gale, C. R. A. Catlow, and P. D. Battle, “Self-consistent interatomic potentials for the simulation of binary and ternary oxides,” *J. Mater. Chem.*, vol. 4, pp. 831–837, 1994. [Online]. Available: http://dx.doi.org/10.1039/JM9940400831

[108] M. S. Islam, S. Lazure, R.-N. Vannier, G. Nowogrocki, and G. Mairesse, “Structural and computational studies of Bi_2WO_6 based oxygen ion conductors,” *Journal of Materials Chemistry*, vol. 8, no. 3, pp. 655–660, 1998.

[109] J. Sauer, K.-P. Schröder, and V. Termath, “Comparing the acidities of microporous aluminosilicate and silico-aluminophosphate catalysts: A combined quantum mechanics-interatomic potential function study,” *Collection of Czechoslovak chemical communications*, vol. 63, no. 9, pp. 1394–1408, 1998.

[110] I. Brown and D. Altermatt, “Bond-valence parameters obtained from a systematic analysis of the inorganic crystal structure database,” *Acta Crystallographica Section B: Structural Science*, vol. 41, no. 4, pp. 244–247, 1985.

[111] C. Pirovano, M. Islam, R.-N. Vannier, G. Nowogrocki, and G. Mairesse, “Modelling the crystal structures of Aurivillius phases,” *Solid State Ionics*, vol. 140, no. 1, pp. 115 – 123, 2001. [Online]. Available: http://www.sciencedirect.com/science/article/pii/S0167273801006993

[112] S. Suehara, P. Thomas, A. P. Mirgorodsky, T. Merle-Méjean, J. C. Champarnaud-Mesjard, T. Aizawa, S. Hishita, S. Todoroki, T. Konishi, and S. Inoue, “Localized hyperpolarizability approach to the origin of nonlinear optical properties in TeO_2-based materials,” *Phys. Rev. B*, vol. 70, p. 205121, Nov 2004. [Online]. Available: http://link.aps.org/doi/10.1103/PhysRevB.70.205121

[113] S. J. Mills and A. G. Christy, "Revised values of the bond-valence parameters for Te^{IV}-O, Te^{VI}-O and Te^{IV}-Cl," *Acta Crystallographica Section B: Structural Science, Crystal Engineering and Materials*, vol. 69, no. 2, pp. 145–149, 2013.

[114] M. Howe, R. McGreevy, and P. Zetterström, "CORRECT: A correction program for neutron diffraction data," *NFL Studsvik internal report*, 1996.

[115] L. Pusztai and R. McGreevy, "MCGR: An inverse method for deriving the pair correlation function from the structure factor," *Physica B: Condensed Matter*, vol. 234, pp. 357–358, 1997.

[116] S. L. Roux and P. Jund, "Ring statistics analysis of topological networks: New approach and application to amorphous GeS_2 and SiO_2 systems," *Computational Materials Science*, vol. 49, no. 1, pp. 70 – 83, 2010. [Online]. Available: http://www.sciencedirect.com/science/article/pii/S0927025610002363

[117] D. S. Franzblau, "Computation of ring statistics for network models of solids," *Phys. Rev. B*, vol. 44, pp. 4925–4930, Sep 1991. [Online]. Available: http://link.aps.org/doi/10.1103/PhysRevB.44.4925

[118] L. Cormier, D. Ghaleb, D. R. Neuville, J.-M. Delaye, and G. Calas, "Chemical dependence of network topology of calcium aluminosilicate glasses: a computer simulation study," *Journal of non-crystalline solids*, vol. 332, no. 1, pp. 255–270, 2003.

[119] B. T. M. Willis and A. W. Pryor, *Thermal vibrations in crystallography.* Cambridge University Press Cambridge, 1975, vol. 1.

[120] W. Hamilton, "On the isotropic temperature factor equivalent to a given anisotropic temperature factor," *Acta Crystallographica*, vol. 12, no. 8, pp. 609–610, 1959.

Etude structurale du verre de TeO_2 et de la variété désordonnée TeO_2-δ par dynamique moléculaire

Résumé : Ce travail a pour but d'améliorer la description structurale du verre de TeO_2 pur et d'étudier en profondeur la structure de la phase désordonnée TeO_2-δ au moyen de la dynamique moléculaire (DM).

Nous avons établi des potentiels interatomiques (IAP), simples mais non triviaux, prenant en compte la polarisabilité des atomes de tellure et d'oxygène à l'aide du modèle cœur-coquille. Nous avons démontré le rôle important de la paire libre électronique de l'atome de Te dans la formation d'unités asymétriques TeO_x. Les IAPs précis reproduisent 17 structures cristallines à base de TeO_2 et sont appropriés pour les simulations par DM des systèmes désordonnés.

Les simulations des structures de la phase vitreuse pure et de TeO_2-δ ont été effectuées par DM. Il a été démontré que le verre de TeO_2 est principalement constitué d'unités structurales TeO_3 et TeO_4, et un grand nombre d'atomes d'oxygène non-pontant (NBO) est observé. La coordinence des atomes de tellure est plus faible dans le verre que dans les structures cristallines pures.

Dans la phase TeO_2-δ, les atomes de tellure forment un réseau cristallin (CFC) bien défini et les atomes d'oxygène présentent un grand désordre de position. Cette phase est caractérisée par une population d'unités structurales, une coordinence des atomes de tellure et une proportion d'atomes d'oxygène non pontant typique du verre. Par conséquent, la structure TeO_2-δ est plus proche de celle du verre que des structures d'autres polymorphes cristallines de TeO_2 pures.

Mots clés : tellurites, verres à base de TeO_2, phases désordonnées, paire libre, potentiel interatomique (IAP), simulation par dynamique mol'eculaire (DM), fonction de distribution de paires (PDF), synthèse de poudres.

Structural study of amorphous TeO_2 and disordered $\delta{-}TeO_2$ phase by molecular dynamics simulations

Abstract: This work aims to improve the structural description of the pure TeO_2 glass and to give a deep insight into the structure of the disordered $\delta{-}TeO_2$ phase by means of molecular dynamics (MD) simulations.

We derived simple but nontrivial interatomic potentials (IAPs), which take into account the polarisability of tellurium and oxygen atoms using the core-shell model. We demonstrated the important role of the electronic lone pair of the tellurium atoms in the formation of asymmetrical TeO_x units. The accurate IAPs is able to reproduce 17 crystalline TeO_2-based structures and are appropriate for MD simulations of disordered systems.

The MD simulations of the pure glass and $\delta{-}TeO_2$ phase structures were carried out. It was demonstrated that the TeO_2-glass consists of mainly TeO_3 and TeO_4 structural units and a large number of non-bridging oxygen (NBO) atoms is observed. The coordination number of the tellurium atoms in the glass is less than in the pure crystalline structures.

In the $\delta{-}TeO_2$ phase, the tellurium atoms form a well-defined crystalline (FCC) lattice and the oxygen atoms exhibit a large positional disorder. This phase has a structural units distribution and a tellurium coordination number and a proportion of NBO atoms similar to those of the glass. Hence, the structure of $\delta{-}TeO_2$ is closer to that of glass than to the structures of other pure TeO_2 crystalline polymorphs.

Keywords: tellurites, TeO_2-based glasses, disordered phases, lone pair, interatomic potential (IAP), molecular dynamics (MD) simulations, pair distribution function (PDF), powder synthesis.

SPCTS - UMR CNRS n°7315
12, rue Atlantis - 87068 LIMOGES